

The effect of water addition on crack formation in inorganic polymer cement from Ca-Fe-Al-silicate glass

Glenn BEERSAERTS

Promotor: Prof. Jan Elsen

Co-promotor: Dr. Lieven Machiels

Begeleider: Lukas Arnout

Proefschrift ingediend tot het
behalen van de graad van
Master of Science in de geologie

Academiejaar 2015-2016

© Copyright by KU Leuven

Without written permission of the promotor and the authors it is forbidden to reproduce or adapt in any form or by any means any part of this publication. Requests for obtaining the right to reproduce or utilize parts of this publication should be addressed to KU Leuven, Faculteit Wetenschappen, Geel Huis, Kasteelpark Arenberg 11 bus 2100, 3001 Leuven (Heverlee), Telephone +32 16 32 14 01.

A written permission of the promotor is also required to use the methods, products, schematics and programs described in this work for industrial or commercial use, and for submitting this publication in scientific contests.

Preface

First of all, I would like to thank professor Jan Elsen and co-promotor Lieven Machiels for giving me the support and opportunity to discover the world of inorganic polymers. I would also like to thank my mentor Lukas Arnout, who provided the necessary equipment for the experiments, taught me the craftsmanship of making excellent inorganic polymers and for the support throughout the year.

I would also like to thank the people of SREMat and in particular Lubica, Yiannis, Remus, Silviana and Arne for the companionship, discussions and guidance throughout the year.

Thanks to Herman for preparing my polished sections. Also thanks for the help I received from Kris, Bart, Gert, Johan and Manuel from the department of MTM.

I would also like to thank my parents, my brother and my friends for being there and helping me to take the right decisions in order to reach this far and to complete my goals. And finally, last but not least, my profound thanks to all my fellow geologists for these five most amazing years of my life.

Abstract (Nederlands)

Het concept recyclage was nog niet uitgevonden in de jaren zeventig waardoor er een enorme hoeveelheid stortplaatsen voor huishoudelijk afval zijn gecreëerd. Vandaag de dag wordt er onderzoek verricht om dit afval te recyclen tot een waardevolle grondstof. Het afval wordt in een plasmaoven ontbonden tot een synthetisch gas, metaal en een Fe-Ca-Al-silicaglas. Dit glas wordt ook wel plasmasteen genoemd en kan Ordinary Portland Cement (OPC) vervangen. Bij de productie van dit glas kan mogelijks tot 80% minder CO₂ uitgestoten worden in vergelijking met de productie van huidig OPC. Een nieuwe soort cement, genaamd anorganische polymeer cement, wordt ontwikkeld bij KU Leuven door de plasmasteen te vermalen en te mengen met een alkalisilicaat oplossing. Er treden echter scheurtjes op in de anorganische polymeer, wat slecht is voor de duurzaamheid. Dit onderzoek tracht weer te geven dat een verschillende H₂O/K₂O verhouding in de alkali oplossing aanleiding geeft tot verschillende soorten scheurtjes en een verschil in anorganische polymeer eigenschappen. De eigenschappen van de anorganische polymeer kunnen afgeleid worden via verschillende experimenten zoals: ultrasoon en Vicat penetratie testen, microscopie, BET en calorimetrie. Verder zal SEM, akoestische emissie en lineaire variabele differentiaaltransformator (LVDT) testen uitgevoerd worden om het scheur en krimp gedrag te achterhalen van de anorganische polymeer. Een alkali oplossing met een H₂O/K₂O molaire verhouding tussen 25 en 35 resulteert in een klein aantal macro scheurtjes in de anorganische polymeer en het behalen van een behoorlijke sterkte tot minimaal 50MPa. De oplossing en polymerisatie piek zal kleiner en verbreed worden naarmate een grotere H₂O/K₂O verhouding in de alkali oplossing gebruikt wordt. Bijgevolg zal de E-modulus en de sterkte lagere waarden behalen en zal de hardingstijd verlengd worden. Autogene krimp zal eerst plaatsvinden tijdens polymerisatie en eens de stijfheid voldoende hoog is, kan krimp door interne anorganische polymeer reacties plaatsvinden in samenhang met warmte- en uitdrogingskrimp. Eens het anorganische polymeer netwerk een behoorlijke sterkte en stijfheid heeft opgebouwd kan verdere krimp voorkomen worden. Bijgevolg gaat er zich een stress of poriëndruk opbouwen in de anorganische polymeer. Macro scheurtjes worden preferentieel gevormd bij kleinere H₂O/K₂O verhoudingen door de opbouw van een grote capillaire poriëndruk, terwijl een activator met een grote H₂O/K₂O verhouding micro scheurtjes vormt door de lage sterkte eigenschappen van de anorganische polymeer. Deze thesis kan een bijdrage leveren tot een beter inzicht in de verandering van krimp en scheurtjes gedrag, bij het veranderen van de reactiviteit of de H₂O/K₂O verhouding in de alkali oplossing, dat gekoppeld kan worden aan de verandering van de anorganische polymeer eigenschappen. Op die manier kan de vorming van macro scheurtjes vermeden worden en de hardingstijd verlengd worden.

Abstract (English)

In the seventies, a lot of landfills with residual household waste were created. Today, research is done to recycle this waste into a valuable raw material. The waste is fed to a plasma furnace, in which it is decomposed into a synthetic gas, metal and a Fe-Ca-Al-silicate glass. The production process of this glass or plasmastone emits up to 80% less CO₂ compared to the production of Ordinary Portland cement (OPC). A new type of cement has been developed from this glass at KU Leuven. The glass is milled and blended with an alkali-silicate activator, to form a type of cement that can be used in similar applications as traditional cement. Unfortunately, cracks are generated, which are bad for the durability. This research will show that when the H₂O/K₂O ratio is changed, different types of cracks are created and different inorganic polymer properties will be achieved. Several experiments to determine the properties of the inorganic polymer are conducted, such as ultrasound, calorimetry, compressive and flexural strength, BET and the Vicat penetration depth. The shrinkage and crack behaviour is determined by the SEM, the acoustic emission test and the linear variable differential transformer (LVDT) test. A H₂O/K₂O molar ratio in the alkali solution between 25 and 35 will give the least number of macro-cracks in inorganic polymer pastes with sufficiently high strength properties and with a minimum in compressive strength of 50MPa. The dissolution and polymerisation peak will be smaller and delayed when using an activating solution with a higher H₂O/K₂O ratio. Consequently, the setting time will be prolonged, a low E-modulus and low strength properties will be achieved. Autogenous shrinkage can be determined first and once the rigidity increases, self-desiccation shrinkage will take place, along with thermal and drying shrinkage. The inorganic polymer network can resist further shrinkage after a certain strength or rigidity build up. Consequently, the stress or pore pressure in the inorganic polymer will start to increase. Macro-cracks are produced mainly at low H₂O/K₂O ratios, due to the high capillary pore pressure build-up. An activating solution with high H₂O/K₂O ratios however, will produce micro-cracks due to the low strength properties of the inorganic polymer. This dissertation can provide a starting point for a better understanding of the change in shrinkage and crack behaviour, linked to the inorganic polymer properties, when changing the reactivity or H₂O/K₂O ratio in the activating solution. In this way, the formation of macro-cracks, which decreases durability, can be mitigated.

List of abbreviations and list of symbols

OPC: Ordinary Portland Cement

BFS: Blast Furnace slag

NASH: Na-Al-Si-H gel network

KASH: K-Al-Si-H gel network

L/S ratio: liquid (activating solution) / solid (plasmastone) ratio

Table of content

Preface	IV
Abstract (Nederlands)	VI
Abstract (English)	VIII
List of abbreviations and list of symbols	IX
Introduction	1
Research objectives	4
1. The state of the art, a new world of cement	5
1.1 The realisation of a new kind of cement.....	5
1.1.1 Raw materials.....	5
1.1.2 Activating solution.....	7
1.1.3 Aggregates.....	7
1.2 The formation of an inorganic polymer from a Ca-Fe-Al rich silicate glass	8
1.2.1 Different types of polymerization and gel phases.....	8
1.2.2 Polymerization stages of the Ca-Fe-Al rich silicate glass.....	11
1.3 Shrinkage and crack formation.....	14
1.3.1 Crack formation due to water loss: the rise of capillary pressure	14
1.3.2 The ratios of compositional elements that affect the formation of cracks	17
1.4 The evolution in shrinkage and cracks	19
1.4.1 Early age shrinkage and crack formation.....	20
1.4.2 Late age shrinkage and crack formation	22
2 Part 1: Change in crack characteristics: research on pastes.....	25
2.1 Methods part 1	25
2.1.1 Blaine size.....	25
2.1.2 Sample paste preparation	26
2.1.3 Cracks observation techniques	29
2.2 Results part 1	31
2.2.1 The choice of a preferred curing condition	31
2.2.2 Crack description of the humidity chamber cured inorganic polymer pastes	32
2.2.3 Compressive strength results	33
2.2.4 BET specific surface.....	33
2.3 Discussion part 1	36
2.3.1 Explanation of the observed crack types	36
2.3.2 Interpretation of the general characteristics of inorganic polymer pastes.....	38

2.4	Conclusion part 1	40
3	Part 2: Crack and Shrinkage evolution in time on mortars.....	41
3.1	Methods part 2	41
3.1.1	Mortar preparation	41
3.1.2	Flexural and Compressive strength measurement.....	42
3.1.3	Calorimetry with an admix ampoule.....	42
3.1.4	The Vicat test.....	43
3.1.5	Non-destructive test: acoustic emission combined with thermocouple	44
3.1.6	Linear Variable Differential Transformatior (LVDT)	45
3.1.7	Ultrasonic test: Young's modulus of elasticity	46
3.2	Results of part 2.....	47
3.2.1	Calorimetry: heat flow evolution	47
3.2.2	The setting time via the Vicat penetration.....	48
3.2.3	Elasticity-modulus evolution.....	49
3.2.4	Compressive and flexural strength on mortars	50
3.2.5	NDT Acoustic emission.....	51
3.2.6	LVDT shrinkage results	54
3.3	Discussion: early age properties and behaviour of inorganic polymers.....	55
3.3.1	Analysis of the heat flow generation	55
3.3.2	The setting times according to the penetration depth.....	56
3.3.3	The evolution in elasticity when curing the inorganic polymer.....	57
3.3.4	Compressive and flexural strength: The result of networking.....	58
3.3.5	Cracks received via acoustic emission.....	59
3.3.6	Autogenous and drying shrinkage, determined with the LVDT measurement..	63
3.4	Conclusion of the early age behaviour and properties of the inorganic polymer.....	66
4.	General Conclusion.....	68
5.	Reference table.....	70
6.	Appendix	73
6.1	Crack description of the pastes	73
6.1.1	The crack description of sample 55B	73
6.1.2	The crack description of sample 60B	75
6.1.3	The crack description of sample 65B	77
6.1.4	The crack description of sample 70B	78
6.1.5	The crack description of sample 75B	80

6.1.6	The crack description of sample 80B	81
6.1.7	The crack description of sample 85B	83
6.1.8	The crack description of sample 90B	84
6.1.9	Sample 95B	85
6.2	Compressive strength results	86
6.2.1	Compressive strength, 2 days after casting	86
6.2.2	Compressive strength, 7 days ago after casting.....	87
6.2.3	Compressive strength, 28 days after casting	88
6.3	Flexural strength	89
6.3.1	Flexural strength after 2 days	89
6.3.2	Flexural strength after 7 days	89
6.3.3	Flexural strength after 28 days	90
6.4	E-modulus and temperature plot.....	91

Introduction

An important global problem that 21st century world leaders are eager to find solutions for is global warming. Its consequences will become increasingly noticeable in the following decades. The major contributor of global warming is the CO₂ emission from combustion. The Ordinary Portland Cement (OPC) production is responsible for 8-9% of the total CO₂ emission (Scrivener and Kirkpatrick, 2008). This production process involves the calcination (burning) of impure limestone to cement clinker. Afterwards, gypsum is added to the grinded cement clinker to obtain OPC (Kim et al., 2013). An environmental-friendly alternative needs to be found because calcination proves to emit a high amount of CO₂.

OPC can be replaced when using by-products like blast furnace slag (BFS) and fly ash (Provis, 2013). These supplementary materials are already combined with OPC and can even enhance the cement properties, such as late age strength (Vinai et al., 2015). When blending an alkaline activating solution with alkali reactive materials, such as BFS, an inorganic polymer is formed (Provis, 2013). These inorganic polymers show promising results but further improvement is necessary.

Next to global warming, two other problems for which sustainable resource efficient solutions need to be found for, are resource shortages and waste. In the seventies and eighties almost every town in Belgium and Europe used to have a landfill of residual household waste. To cope with the increasing consumption of society of those years, more than 4000 dump sites are present in Belgium (Jones et al., 2013). During the eighties, our society became more aware of the waste problem and the amount of landfills were reduced (Jones et al., 2013). Since then, all dump sites have been sealed and covered to prevent contamination of ground water. Today, old landfills are dug up to be categorised according to its composition and properties and sealed off again for later potential use (GroupMachiels, 2015).

Nowadays, a solution is being searched for to clean up the landfills of the seventies and eighties and to re-use their materials (Jones et al., 2013). The recuperation of materials from old dump sites, like at the Remo site in Houthalen, is called enhanced landfill mining. The Closing the Circle project of Group Machiels is an example of a enhanced landfill mining project (GroupMachiels, 2015). The waste will be dug up and categorised into different recyclable components. The non-recyclable fraction will be fed to a plasma gasification process to be converted to three products, being a synthetic gas, metal and a calcium-iron-aluminium-rich silicate glass (Machiels et al., 2014). This last fraction can also be called plasmastone. The organic waste products will form a synthetic gas during plasma

gasification. The synthetic gas can be used as an energy source for electricity or heating (Taylor et al., 2013). The whole process is shown on Figure 1. The plasmastone can be used as a new type of cement for similar applications as OPC (Machiels et al., 2014). This process will have a reduced CO₂ emission up to 80% compared with the production of OPC (Davidovits, 2013). The reduction in carbon emission and enhanced landfill mining can subsequently give a contribution for the mitigation of global warming and waste.

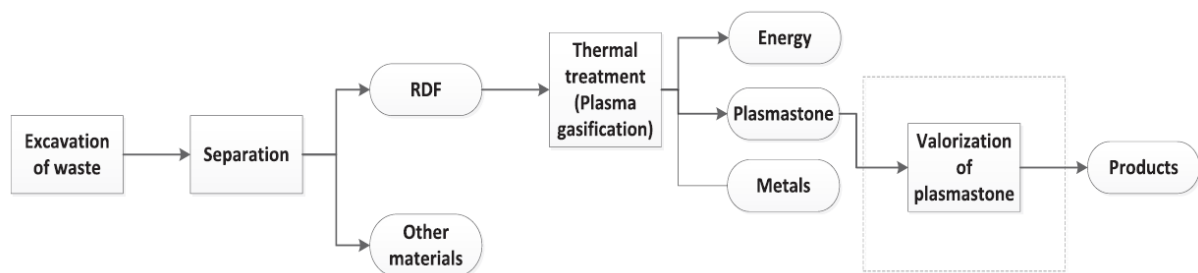


Figure 1: Plasmastone becomes a valuable raw material for the application of inorganic polymer concrete. This figure shows the process from excavation until the production of plasmastone (Danthurebandara et al., 2015).

KU Leuven conducts a research on a new type of inorganic polymer. This research is part of the Plasmatec project and KU Leuven is assigned to create an inorganic polymer cement product from plasmastone. This plasmastone will replace OPC, as illustrated on Figure 2. The Plasmatec project comprises several industrial companies who are involved in the R&D of landfill mining up to the valorisation and investigation of plasmastone properties. In this way, landfills get recycled to valuable secondary raw materials, used to create an inorganic polymer (Jones et al., 2013).

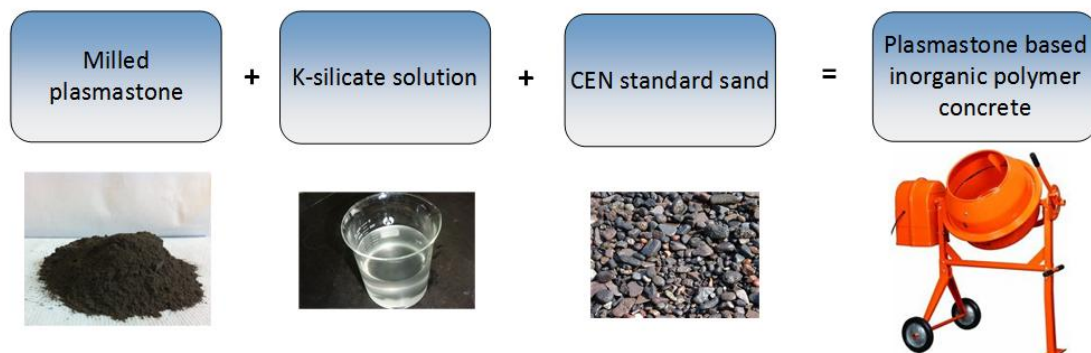


Figure 2: An inorganic polymer concrete is produced without OPC, only by mixing plasmastone with an activating solution and aggregates (modified after (Machiels, 26/03/2015)).

To create an inorganic polymer, the plasmastone will be milled to a fine grained powder and blended with an alkaline solution, consisting of a $\text{SiO}_2/\text{K}_2\text{O}$ molar ratio of 1.6 and a $\text{H}_2\text{O}/\text{K}$ -silicates ratio of 55 wt%. Once mixed and casted, the activating solution will dissolve the plasmastone and an oversaturation of Al-silicates will be reached in the solution to form an inorganic polymer network (Provis, 2013).

Cracks are formed in this type of inorganic polymer after setting and influence the strength and durability of the inorganic polymer (Kriskova et al., 2015). To achieve an inorganic polymer from residual household waste that is economically valuable, the number of cracks will need to reduce. The main focus of this thesis is to reduce the number of cracks, especially macro cracks, by adding water to the activating solution. The addition of water to the activating solution has several advantages: it can reduce the number of cracks and prolong the setting time of the inorganic polymer (Kriskova et al., 2015). Furthermore, it will reduce the cost of the expensive potassium-silicate activating solution.

Research objectives

The inorganic polymer, produced from a Ca-Fe-Al silica glass, has some problems, such as the occurrence of cracks, which decreases the durability. To mitigate the number of cracks, research needs to be done to understand the mechanism of crack formation. This thesis will focus on the formation of cracks in the inorganic polymer, with different water ratios in the activating solution.

In the first research part, the crack characteristics, on microscopic scale, of the inorganic polymer pastes will be described for each water ratio after 28 days of curing. The pastes, each prepared with a different H₂O/K-silicate ratio, are compared with each other in order to find an optimum in water ratio of the activating solution. This optimum results in the least amount of cracks, a proper inorganic polymer development and a minimum in required strength properties.

The second research part of the thesis will focus on the type of reactions and processes that can generate cracks in inorganic polymer mortars. In order to know these processes, the early age properties of the inorganic polymer for different water ratios need to be studied. The second part comprises the following objectives:

1. The properties of the inorganic polymer include the amount of reaction that took place, the setting time, the elasticity and the strength. The change in these properties must be correlated by the use of a different water ratio.
2. The change in early age properties of the inorganic polymer for different water ratios can explain the different behaviour in shrinkage and crack formation of the samples.
3. An evolution model of the formation of cracks and the shrinkage behaviour can be made. This evolution model must be explained by the inorganic polymer properties in order to know why at a certain moment the sample starts to crack and what processes are occurring at that time. This way, by understanding the processes of the inorganic polymer, the crack and shrinkage behaviour can be controlled.

1. The state of the art, a new world of cement

The literature comprises an overview of the raw materials for synthesising inorganic polymers. In the second part, the different types of processes that occur during polymerisation and the evolution from a liquid to a hardened stage are explained. Furthermore, the driving force to generate shrinkage and cracks will be explained. Subsequently, the influence of the amount in compositional elements to the formation of cracks and shrinkage are mentioned. And last, the different types of shrinkage and cracks, that can be formed during the early and late stage of the inorganic polymerisation process, will be described.

1.1 The realisation of a new kind of cement

In this paragraph, the components used to synthesise an inorganic polymer paste and mortar are described. To produce the particular inorganic polymer paste of this thesis, only two raw materials are needed. These two substances are, a solid Ca-Fe-Al-rich silicate glass called plasmastone and the activating solution, which consists of alkali-silicates and water. To prepare a mortar sand, aggregates are added to the mixture.

1.1.1 Raw materials

1.1.1.1 Activators

According to Provis (2013) the major elements of alkali activated materials or activators can vary from calcium rich silicates precursors, like metallurgic slag, to more aluminium rich silicate precursors, like fly ash. Blast Furnace slag (BFS), fly ash, volcanic ashes, steel slag, phosphorous slag, copper slag and ferronickel slag can all be used for the production of inorganic polymers (Provis, 2013). Slag's are by-products of the metallurgic industry and are commonly quenched. Quenching is a process whereby the residue melt is cooled that fast that crystallisation of the melt cannot take place (Provis, 2013). This process gives an amorphous, glassy structure to the slag.

Inorganic polymers or geopolymers are a subdivision of the alkali activated materials with exclusively Al-silicates and a low amount of calcium, as illustrated on Figure 3. In certain

building applications, inorganic polymers are used, but not yet customized on large scale as OPC (Provis, 2013). The term inorganic polymer is however not well defined (Provis, 2013).

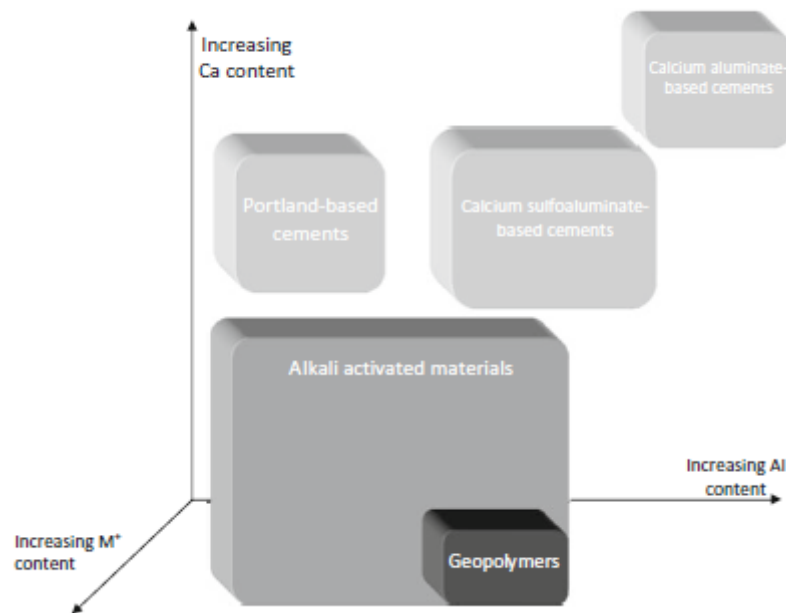


Figure 3: Based on the chemical composition of Ca and Al of the precursor and the M⁺ content, which is the Na and/or K content in the activating solution the different raw materials can be classified (Provis, 2013). Darker grey colours indicate a higher amount of M⁺ content.

1.1.1.2 Plasmastone

Plasmastone will be used as raw material to prepare the inorganic polymer pastes and mortars. Quenching molten plasmastone results in an oxidic amorphous glassy structure (Machiels et al., 2014). This amorphous nature is very important for the reactivity of the plasmastone when mixing with the activating solution (Kriskova et al., 2015).

The composition of the plasmastone used in this thesis is given on Table 1 (Kriskova et al., 2015). The glass contains mainly Si, Fe, Ca and Al and has a glassy dark brown colour. The minor elements are Ti, Na, Cu, Zn and Mg (Kriskova et al., 2015). The chemical composition of the plasmastone can differ however, depending on the heterogeneity of the waste feed. The glass is quite rich in Ca, with a CaO amount of 20%, which is more than Al (Machiels et al., 2014). In this case, the composition of the plasmastone is not confined to a few major elements, but to a broader range of major elements like Fe, Ca and Al.

SiO ₂	CaO	Fe ₂ O ₃	Al ₂ O ₃	Na ₂ O	MgO	ZnO	TiO ₂	CuO	Others
33.6 %	21.7 %	19.9 %	11.9 %	4.0 %	3.4 %	1.9 %	1.7 %	1.1 %	0.9 %

Table 1: An average composition in wt% of the plasmastone or Ca, Fe, Al rich silicate glass (Kriskova et al., 2015).

1.1.2 Activating solution

The activating solution consists of K- or Na-silicates and water (Provis, 2013). Water in the activating solution is of major importance because it is a catalyst for the dissolution of the plasmastone grains and the creation of the inorganic polymer (Vijayakumar, 2013). Water also improves the transportation of the alkali-silicates throughout the inorganic polymer gel (Scherer, 1987). That way, the alkali-silicates can diffuse in the network to dissolve grains as much as possible.

The alkaline solution will be created by adding NaOH or KOH pellets in a silicate water solution. The addition of the NaOH or KOH will result in a high pH and will give the alkaline character to the solution. The NaOH or KOH will react with the silicate chains and will cut the chains in small pieces to become a K-silicate solution (Provis, 2013).

1.1.3 Aggregates

Aggregates are important because they give extra support for the concrete (Lee, 2007). The strength will increase when the concrete is more aggregates supported. Aggregates will not dissolve, or only in a very limited way (Provis, 2013). They will not participate in the inorganic polymer gel formation. Aggregates can give a better dispersion of the gel, they can break up gel clumps and make the structure more uniform (Holt, 2001).

1.2 The formation of an inorganic polymer from a Ca-Fe-Al rich silicate glass

This section will discuss the different reactions that will take place and the different gel phases that will form when mixing the activating solution with the Ca-Fe-Al rich silicate glass or plasmastone. Afterwards, the different polymerization stages will be described. This section is important because it represents the processes that occurs at micro to macrostructure scale which can be linked with the evolution in properties of the inorganic polymer.

1.2.1 Different types of polymerization and gel phases

The formation of different inorganic polymer gel types can be a result of the abundance of Ca, Fe and Al compounds in the plasmastone. The possible gel types that can form due to the Ca and K cation exchange are K-Al-Si-H (KASH) and Ca-Al-Si-H (CASH) gels (Machiels et al., 2014). Some gel types can also be enriched with Fe. Figure 4 indicates the formation of a NASH or CASH gel according to the amount of Ca and Mg (Provis and Bernal, 2014).

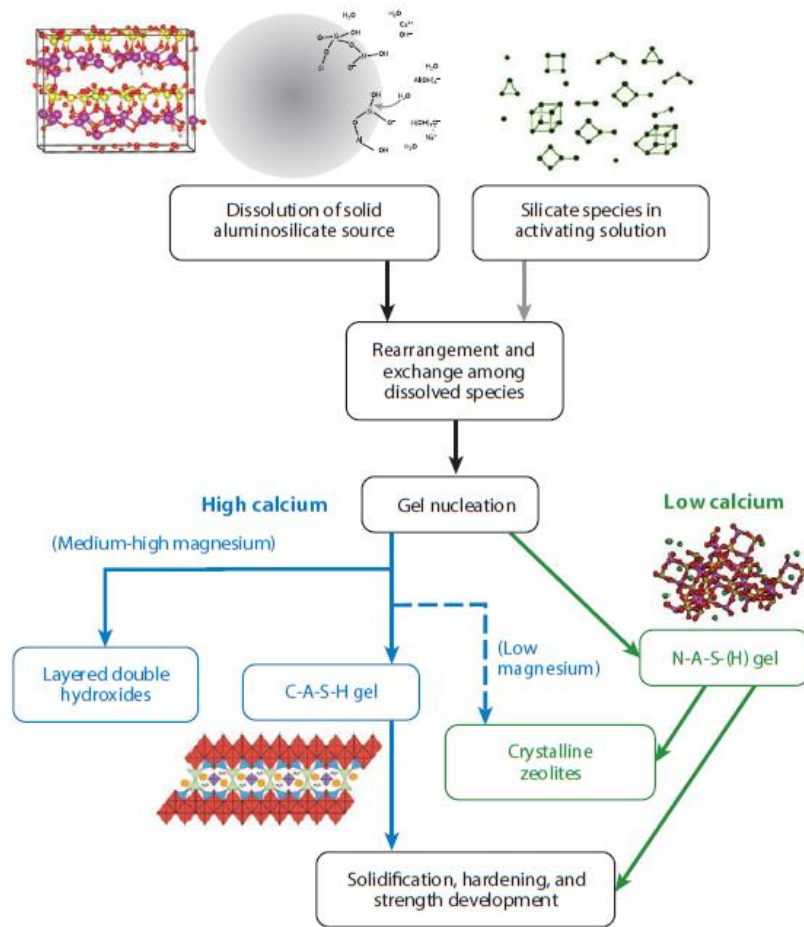


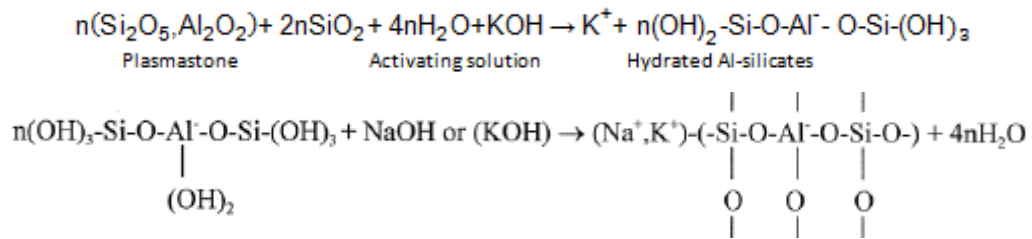
Figure 4: The process of gel formation is given, from dissolution of the glass until hardening of the inorganic polymer. The proportion of calcium is an important factor in the formation of gels, as explained in the following subchapters (Provis and Bernal, 2014).

1.2.1.1 The formation of KASH/NASH gels

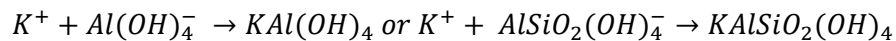
The Na^+ and K^+ ions in the alkali solution will react with the Ca-Fe-Al-silicate glass. When the alkali solution reacts with the plasmastone, the non-crystalline grains will dissolve (Provis, 2013). The dissolution of the Ca-Fe-Al-silicate glass will give Fe^{3+} , Al^{3+} and Si^{4+} ions in solution. The aluminates and silicates in the solution get hydrated and form a chain of Al-silicates, silicates and aluminates species (Vijayakumar, 2013). In that way, the hydrated Al-silicates, in the form of monomers or oligomers, will saturate the solution (Provis, 2013).

Once a threshold value of oversaturation is exceeded, a gel is being formed. The Al-silicates start to nucleate and form a chain network, which results in an increase in viscosity and the appearance of a gel. The formation of an Al-silicate chain is illustrated in the first reaction

formula below (Duxson et al., 2007). The second reaction represents the polymerization and condensation of the oligomers to form a large KASH amorphous network system (Xu and Van Deventer, 2000). During condensation, water is released when the chain network becomes more and more extended by crosslinking (Duxson et al., 2007).



According to Kuenzel et al. (2012) the Al-hydrate and Al-silicate chain network in the solution are negatively charged and are being balanced by the Na^+ and K^+ cations from the activating solution. K^+ cations in the solution preferentially bond in the gel with the hydrated Al, Al-silicates, mono- and oligomers (Xu and Van Deventer, 2000). As can be seen in the reaction formula given below, KASH gels will be formed, depending on the availability of potassium (Kuenzel et al., 2012).



1.2.1.2 The formation of CASH and CSH gels

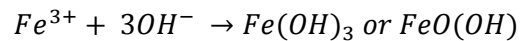
The dissolution of the plasmastone will give Ca^{2+} in solution. According to Provis (2013) the influence of a calcium rich source in the solution depends on the balance between the Ca availability from the source and the alkalinity of the activating solution.

An activating solution with low to moderate alkalinity will produce Ca-Si-H (CSH) gels, which is a similar gel phase that is produced when water reacts with OPC (Provis, 2013). The activating solution is however very alkaline, so a CSH phase will probably not be formed. Only solutions with a high Ca/Si ratio and with the absence of Al can lead to the formation of CSH gel (Provis, 2013).

Provis (2013) suggests that the KASH gels, in a system with a high amount of Ca, will become unstable and will form CASH gels. A system with a high pH, due to the alkalis, can cause an exchange of potassium for calcium in the gel which favours the formation of a CASH gel (Provis, 2013).

1.2.1.3 The influence of Fe and other elements in the gel phases

Fe can have a similar behaviour as Al in the polymerization process and will form an Fe rich gel phase. Kriskova et al. (2015) stated that Fe can occur throughout the binder phase, as well as locally in high concentrations. The Fe rich local zones can precipitate as a hydroxide or oxohydroxide (goethite) as formulated below (Duxson et al., 2007). Further research needs to be conducted to find out the behaviour of Fe in the gel.



Some non-crystalline silicates or unreacted glass will remain in the gel structure. Only at the surface of those grains, some reaction can take place for binding the undissolved particles with the final inorganic polymer structure. Consequently, the inorganic polymer gel encapsulates the less reactive phases (Provis, 2013). Provis (2013) states that unreacted particles can disrupt the formed gel network, which can result in lower overall strength.

1.2.2 Polymerization stages of the Ca-Fe-Al rich silicate glass

The more polymerization, the more viscous the solution becomes. First the solution becomes a gel and in the final stage, a hard inorganic polymer (Scherer, 1988). The gelation and polymerisation process is illustrated on Figure 5. The timescale between the first and second phase depends on several factors, such as the reaction rate and the composition of the activating solution (Provis, 2013).

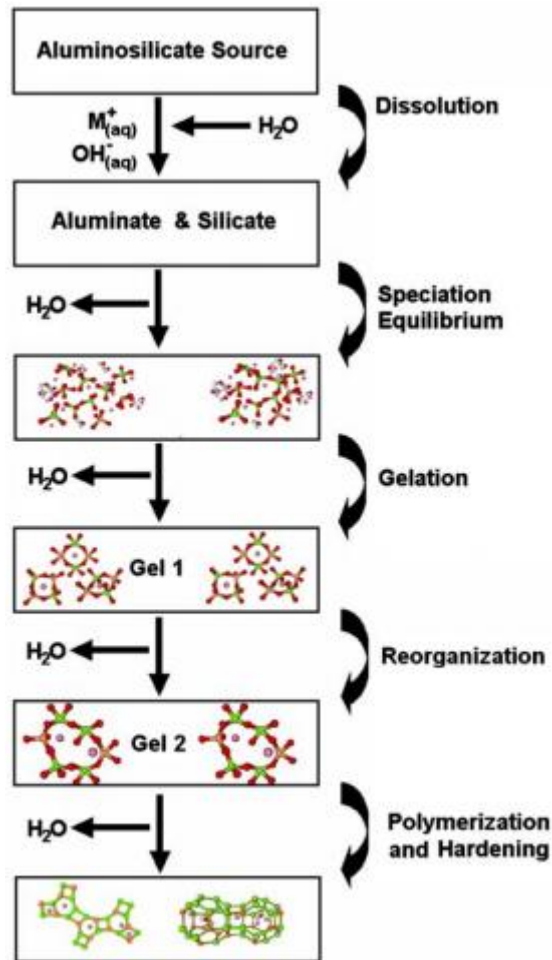


Figure 5: A schematic view of the polymerization process by Duxson et al. (2007).

The first stage is the liquid stage. In this stage, the plasmastone grains dissolve and the Al^{3+} ions form monomers (Xu and Van Deventer, 2000). The viscosity is very low at this stage (Scherer, 1988).

The gel or skeleton stage occurs when the liquid loses its fluidity and when viscosity increases rapidly (Scherer, 1988). During the gelation process, a continuous rearrangement of the network will take place, which gives an increase in connectivity of the gel network as visualised on Figure 5. This way, the formed KASH chains will go through a process of densely cross linked clusters to create a gel network (Scherer, 1988).

During polymerization, Scherer (1988) states that the gel contracts and the liquid will be trapped in the network pores or will be expelled from the gel. The gel consists in this stage of a solid network with a liquid phase incorporated in the network. The remaining liquid, which is

trapped in the pores of the gel network, can participate in further polymerization reactions. This reaction type is called self-desiccation reaction (Lee, 2007). The continuous dissolution and precipitation results in a volume decrease, which will give a reduction in surface area and an increase in pore size in the gel according to the paper of Machiels et al. (2014).

The hard stage is the final stage of polymerization. The inorganic polymer is set and hard enough to resist stresses and further contraction of the gel (Scherer, 1988). Most of the liquid is used for reaction, is dried or is expelled from the inorganic polymer. Self-desiccation reactions are the only reactions that take place at this stage (Holt, 2001). The rate in polymerization decreases and the inorganic polymer reaches its maximum density according to Scherer (1988).

1.3 Shrinkage and crack formation

Capillary pressure is an important topic because it is the driving force for shrinkage and the formation of cracks in an inorganic polymer. The differences in ratios of major elements can influence the polymerization process, the pore size and the formation of cracks. These different ratios include the liquid/solid ratio, the K-silicate/water ratio and the Si/(Na or K) ratio.

1.3.1 Crack formation due to water loss: the rise of capillary pressure

Apart from thermal expansion and contraction, capillary pressure is the main contributor to the formation of cracks. In the beginning of gel formation, water covers the surface of the solid gel phase in order to reach its lowest energy state (Scherer, 1988). When there is an abundance of water, the water can move along the pores and can wet all the surfaces/pores. In this stage, no tension will be created (Scherer, 1988).

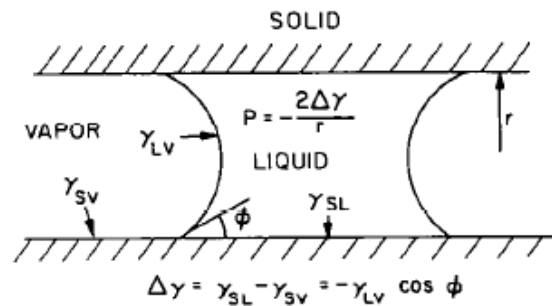


Figure 6: The different tensile stresses that is exercised on the water. $\gamma_{\text{vapour/solid}} > \gamma_{\text{liquid/solid}} \rightarrow \Delta\gamma = \gamma_{\text{liquid/vapour}}$ results in a meniscus curvature with a stress exercised on the pore walls (Scherer, 1987).

When the rate of the water loss is higher than the rate of the remaining water to cover the solid surface, a part of the solid surface will come in contact with the vapour phase (Scherer, 1988). The solid-vapour contact creates a tension, because the water is not in its lowest energy state anymore. The solid/vapour contact ($\gamma_{\text{vapour/solid}}$) has more energy than the solid/liquid contact ($\gamma_{\text{liquid/solid}}$) (Scherer, 1988). This tension difference results in a liquid/vapour tension ($\gamma_{\text{Liquid/Vapour}}$), as can be seen on Figure 6 (Scherer, 1987). On Figure 7, the tension in the liquid is given by σ but is similar to γ .

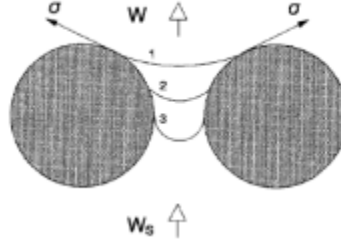


Figure 7: The creation of capillary forces between two grains in the occurrence of water loss (Radocea, 1992).

To reduce the tension and consequently, its pressure difference, the dry surface needs to be covered again with water to prevent further solid/vapour contact. If this is not possible, the water will form a meniscus, as can be seen on Figure 8. The concave meniscus in a pore will be forced to be pulled into the pore by the pressure difference, as illustrated on Figure 7. When the meniscus moves between the pores, the pressure of the meniscus will be exerted on the solid network walls according to Holt (2001). In this stage, the network is not water supported anymore (Scherer, 1988). To counteract these pressures on the walls, the network will contract or shrink, which leads to a reduction of the surface area (Kuenzel et al., 2012). The decrease in surface area results in a wet supported network because the water meniscus can wet the whole surface again according to Kuenzel et al. (2012).

Scherer (1988) states that the amount of shrinkage of the network depends on the amount of water that is removed from the gel. When water is being removed, the liquid will retreat further between the pore walls until the meniscus reaches its minimum radius. At that point, the meniscus cannot retreat any further between the pore walls and the gel reaches its maximum contraction. The pressure in the liquid at the exterior surface, according to the meniscus curvature r and α , the contact angle between the water surface and the pore wall, is formulated as: $P = \frac{2(\gamma_{solid/vapor} - \gamma_{solid/liquid}) \cos \alpha}{r}$. An example is given on Figure 6 (Scherer, 1987).

The formula below indicates that a tension difference results in a pressure rise and that a smaller pore size will result in a bigger capillary pore pressure (Scherer, 1988).

$$\text{Capillary pressure } P_r = \frac{(\gamma_{solid/vapor} - \gamma_{solid/liquid}) S_p}{V_p} \text{ with pore volume } V_p \text{ and surface area } S_p.$$

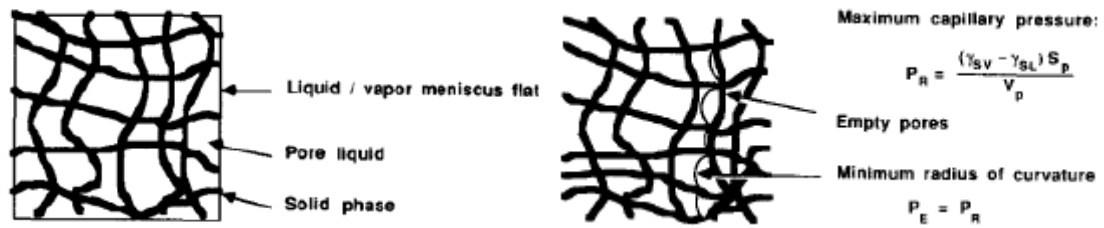


Figure 8: This illustration represents the gel network. Inside the network, a meniscus or curvatures are present on the network surface when water is lost. The formation of a meniscus results in a pressure according to the tension difference and the pore volume (Scherer, 1987).

In the hardened stage, the inorganic polymer network already has some strength build-up. The network will not shrink anymore because the pore walls can withstand the exerted pressure (Scherer, 1988). Consequently, the network gel system is not wet supported anymore. At a certain threshold the capillary stress on the walls will exceed the strength of the network according to Scherer (1988) and a crack will be formed to release the pressure build-up exercised on the network.

A similar process happens when water starts evaporating earlier on the inorganic polymer surface than in the core of the sample (Scherer, 1987). Once the surface water forms a meniscus, the water will be drawn back into the gel. Consequently, the surface will be exposed to desiccation and shrinkage. The retreat of the liquid will create a pressure difference between the interior, which is more wet, and exterior of the inorganic polymer. This tension can result in cracks at the surface (Scherer, 1988). The wet interior gel will respond with a tension pressure to equilibrate with the surface pressure (Scherer, 1987). Consequently, a bigger pressure will be exercised on the wet interior, which favours the formation of cracks. When the water distribution from the wet interior to the dry exterior is fast enough, the loss of water in the interior will result in shrinkage of the interior (Scherer, 1987).

1.3.2 The ratios of compositional elements that affect the formation of cracks

1.3.2.1 *The influence of the liquid over solid ratio on the properties of the inorganic polymer*

An inorganic polymer with good properties depends on the liquid (activating solution) over solid (plasmastone) ratio (L/S ratio) (Bentz and Jensen, 2004). When decreasing the L/S ratio, an increase in compressive strength and a reduction in shrinkage, cracks and porosity is observed by Machiels et al (2014). Such low L/S ratios result, according to the paper of Kriskova et al. (2015) in a fast setting and a dry paste, without the creation of an extensive gel. A L/S ratio which is too high would also result in poor strength properties (Bentz and Jensen, 2004). Cracks and shrinkage is more expressed with a high L/S ratio according to Machiels et al (2014). The optimum L/S ratio, proposed by Bentz and Jensen (2004) is situated around a ratio of 0.39.

1.3.2.2 *The H₂O/K-silicates ratio in the activating solution*

An increase of the H₂O/K-silicates ratio in the activating solution will result in a decrease in viscosity of the liquid. The reaction rate will be slower, due to the lack of potassium, according to Kriskova et al. (2015) which can prolong the strength build-up. If the H₂O/K-silicates ratio is too high, some plasmastone grains will not dissolve and the grains will remain in suspension, as stated in the paper of Kriskova et al. (2015). The increase in water results in a deficiency of Al-silicates to reach oversaturation for the formation of the gel (Provis, 2013). Provis (2013) interpreted this result due to a low amount of polymerisation.

The increase of the H₂O/K-silicates ratio in the activating solution will not prevent shrinkage, only more water will have to be removed before shrinkage can occur (Kuenzel et al., 2012). The gel will be resistant to drying shrinkage until the water content reaches the amount of structural water according to the interpretation of Kuenzel et al. (2012). A higher water content can give a higher porosity, a larger amount of free water will stay trapped in the network (Kriskova et al., 2015). When increasing the H₂O/K-silicates ratio, more micro-cracks (20-50 µm) can be formed according to Eppers (2010).

A decrease of the H₂O/K-silicates ratio on the other hand, can give a faster setting time. According to the paper of Bentz and Jensen (2004), the heat production due to the exothermal reactions and the shrinkage will occur in a shorter time period.

1.3.2.3 *The variation of the $\text{SiO}_2/(\text{Na}_2\text{O or K}_2\text{O})$ ratio*

When using an activating solution with a high $\text{SiO}_2/\text{K}_2\text{O}$ ratio, the dissolution of the plasmastone will not happen in the appropriate way according to Vinai et al. (2015). Their paper state that the gel will become very dense because long silica chains are formed. Consequently, the paper of Vinai et al. (2015) says that water will get trapped in the dense inorganic polymer gel. The trapped pockets of water can result in macropores (Kriskova et al., 2015). In this case, shrinkage will occur at a later stage once the water is removed from the gel (Vinai et al., 2015). According to Kriskova et al. (2015) an increase in $\text{SiO}_2/\text{K}_2\text{O}$ ratio will result in a low strength development and a prolonged setting time.

A low $\text{SiO}_2/(\text{Na}_2\text{O or K}_2\text{O})$ ratio on the other hand will give a high polymerization rate. This results in a greater shrinkage according to Vijayakakumar (2013) and high strength properties according to Kriskova et al. (2015). Increasing the K_2O content will favour the Al dissolution of the glass (Rees et al., 2007).

When a certain low $\text{SiO}_2/(\text{Na}_2\text{O or K}_2\text{O})$ threshold ratio is exceeded, there are not enough silicates left to form a proper network and to achieve higher strength values according Vinai et al. (2015). The reactivity of the solution will be too high in that case and the plasmastone grains can't dissolve properly before the inorganic polymer is produced and hardened (Vinai et al., 2015). Cracks are generated because the inorganic polymer hardens too fast and cannot withstand the pressure built-up (Kriskova et al., 2015).

1.4 The evolution in shrinkage and cracks

Shrinkage and cracks are phenomena that are triggered by different processes at different stages in time. A general overview is given on Figure 9. The shrinkage at early age occurs in the liquid and gel stage of the polymerisation process. The shrinkage and crack formation at a late stage is situated in the stiff and hardened stage of the inorganic polymer formation. In the late stage, deformation and shrinkage will be less pronounced (Holt, 2001).

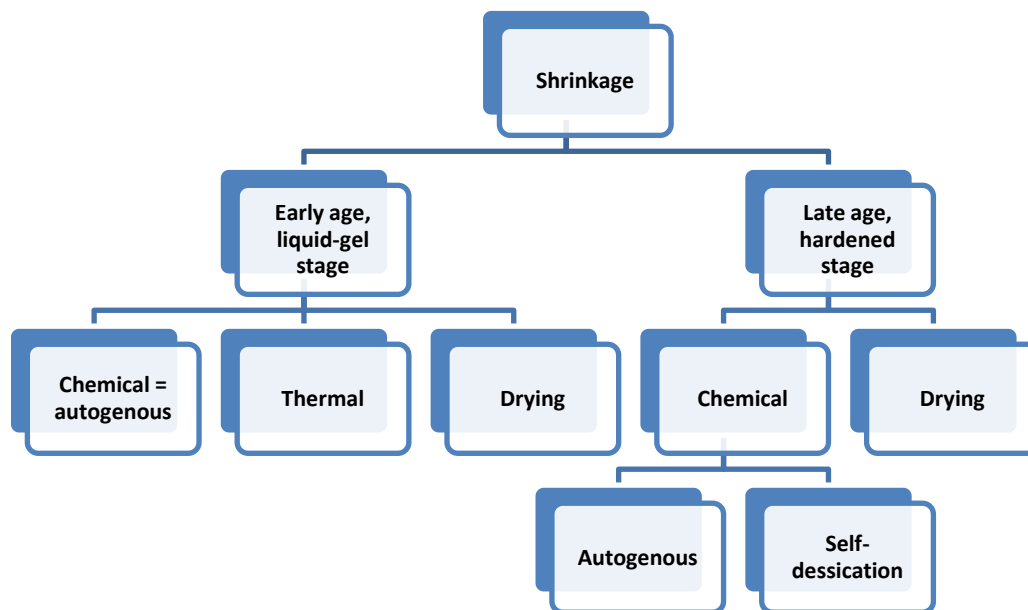


Figure 9: The organization chart of the different types of shrinkages. Modified after Holt (2001).

According to Machiels et al. (2014) a larger chemical heterogeneity in the inorganic polymer paste can result in a larger number of cracks. The zones between the different chemical heterogeneities can be a weak spot with different stresses. This weak zone can be prone to crack formation (Machiels et al., 2014). A wide variation in pore size can give more cracks because of the differences in stress distribution than a uniform pore size (Scherer, 1988).

1.4.1 Early age shrinkage and crack formation

1.4.1.1 Chemical shrinkage is similar to autogenous shrinkage

When the activating solution is mixed with the plasmastone and produces an inorganic polymer gel, a volume reduction can take place (Machiels et al., 2014). The volume reduction can result in shrinkage without moisture loss by evaporation (Holt, 2001; Sagoe-Crentsil et al., 2013). This type of shrinkage is called chemical shrinkage (Lee, 2007). In the early stage of chemical shrinkage, the gel is still deformable and any sort of capillary pressure or volume reduction can result in contraction of the gel. When this contraction or volume reduction is macroscopically visible, it can be called autogenous shrinkage (Lee, 2007). In the early stage of the shrinkage process, the chemical shrinkage is similar to autogenous shrinkage and the shrinkage is uniform with no tension differences in the gel (Holt, 2001).

1.4.1.2 Thermal shrinkage

Polymerisation releases heat, which will cause thermal dilation of the inorganic polymer, as can be seen on Figure 10 (Lee, 2007). Heating in the gel occurs uniformly because the polymerisation reactions will take place throughout the gel. The cooling down evolution afterwards will be different however. The gel surface in contact with the colder environment will be affected first. The centre of the gel remains warm for a longer period however. This will result in an earlier contraction of the surface in comparison with the interior. If the gel has formed already some rigidity, the different contraction rates will cause a difference in tension between the colder and hotter regions of the gel (Scherer, 1987). This tension, according to Holt (2001), can exceed the strength of the gel and can cause cracks.

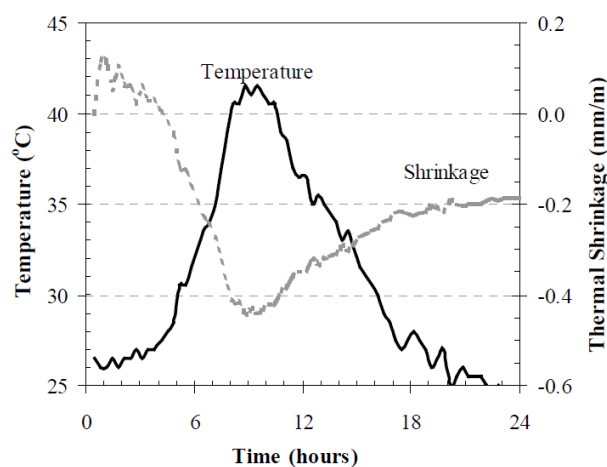


Figure 10 represents the influence of the temperature on shrinkage for OPC (Holt, 2001).

Figure 10 illustrates expansion when temperature increases. When the gel cools down, shrinkage will increase again. The shrinkage results from Holt (2001) in Figure 10 account for OPC. The shrinkage evolution is similar for inorganic polymers, only the time scale and shrinkage magnitude is different.

1.4.1.3 Drying shrinkage

Once the inorganic polymer is exposed to the environment, which is unsaturated in water, evaporation will start (Lee, 2007). Due to evaporation at early age, an extend of water will be evaporated while this water could still be a part for the polymerisation reaction (Scherer, 1988). Evaporation will first affect the surface of the sample. The internal moisture will move to the surface to wet the gel (Scherer, 1988). Scherer (1988) indicates that, once the water content is lower than the structural water content, the network will not be water supported anymore. Consequently, capillary pressure will be performed on the network according to Lee (2007) to generate shrinkage. Some dense phases of the network at an early stage can also be exposed to crack formation (Sagoe-Crentsil et al., 2013; Scherer, 1988). The early stage drying shrinkage and cracks can result in a decrease in strength properties (Sagoe-Crentsil et al., 2013).

A covered curing condition, sealed from the environment, has no early stage drying shrinkage (Lee, 2007). The difference in curing condition can be seen on Figure 11. The number of cracks will be reduced in the covered curing conditions according to Scherer (1988).

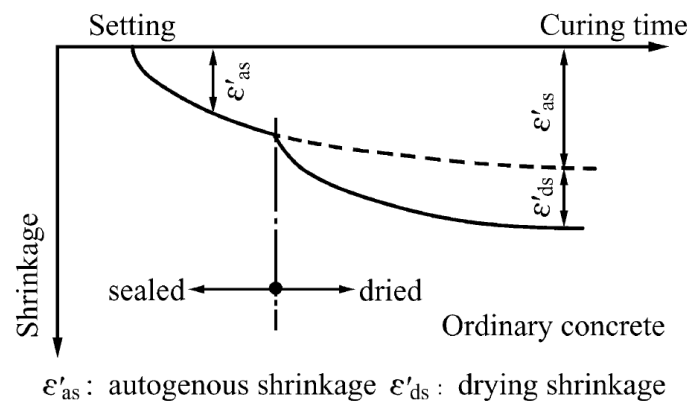


Figure 11: The difference in shrinkage at sealed or open drying conditions during curing (Zhang et al., 2003).

1.4.2 Late age shrinkage and crack formation

1.4.2.1 Chemical Shrinkage: self-desiccation and autogenous shrinkage

The autogenous shrinkage at the late stage will not be similar to chemical shrinkage, as can be seen on Figure 12. The gel will be hard enough to resist some shrinkage (Scherer, 1988). According to Holt (2001), chemical shrinkage can be subdivided in this stage into autogenous shrinkage and self-desiccation shrinkage. Autogenous shrinkage remains the macroscopic shrinkage of the inorganic polymer, as a result of the large scale chemical shrinkage. The part of the chemical shrinkage that doesn't result in autogenous shrinkage, but gives internal volume change is called self-desiccation shrinkage, as illustrated on Figure 13. Self-desiccation shrinkage is a process that takes place in the gel and enlarges the pores of the gel (Vijayakumar, 2013).

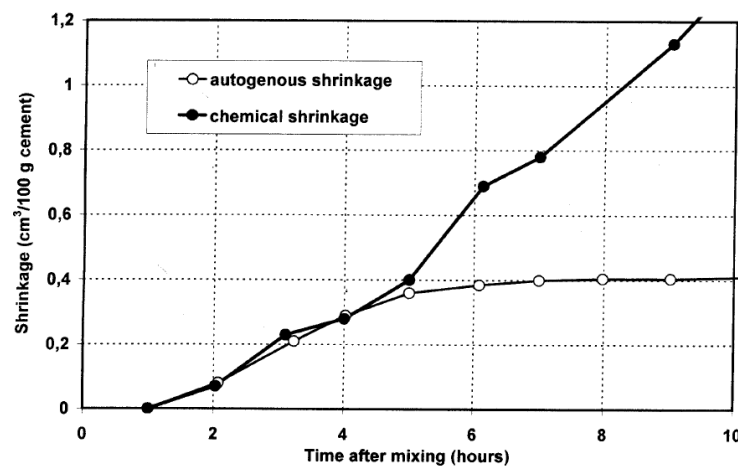


Figure 12: Once the gel is hardened, the autogenous shrinkage will become a part of the chemical shrinkage. Self-desiccation shrinkage becomes the major contributor to chemical shrinkage (Holt, 2001). The time scale is only indicative and is representative for OPC, but not for inorganic polymers.

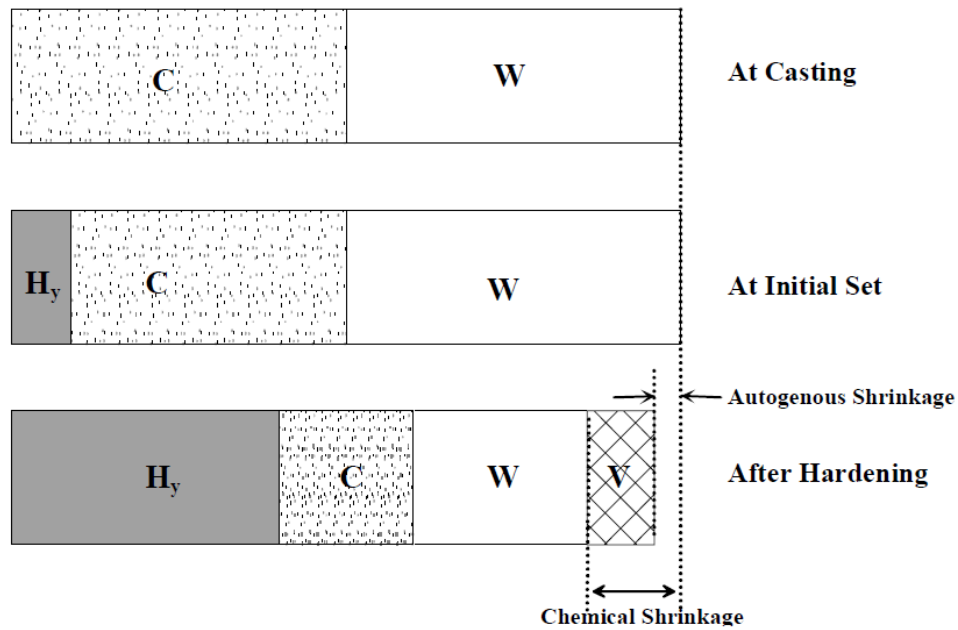


Figure 13: The different stages of the OPC concrete. The difference between autogenous and chemical shrinkage is displayed. C = cement cfr to plasmastone, W = liquid phase, Hy = formed gel phase, V = volume reduction inside the gel due to pore formation by self-desiccation shrinkage (JCI, 1999).

The loss of liquid and the increase in volume and surface of the pores will give a rise in capillary pore pressure, according to the paper of Vijayakumar (2013). The capillary pressure and the chemical shrinkage has a uniform distribution in the gel according to Holt (2001). If the pressure exceeds the strength of the gel network, Bent and Jensen (2004) states that cracks can be induced at that moment.

1.4.2.2 Late drying shrinkage

Drying shrinkage in the late stage is similar to drying shrinkage in the early stage. When the inorganic polymer is exposed to the environment at the late stage, evaporation will take place. At first, the surface will be affected by evaporation. In the next step, the liquid in the pores will start to evaporate. The water in the large pores will start to evaporate first according to Scherer (1988). Scherer (1988) continues that the remaining water will retreat to the smaller pores, which will be later on subjected to evaporation. The capillary pore stress build-up will be proportional to the drying once the maximum shrinkage or density of the inorganic polymer is reached (Scherer, 1988). When this capillary stress exceeds the strength of the inorganic polymer, cracks can be generate according to the paper of Kirschner and Harmuth (2004).

When the inorganic polymer is covered in the early stage, drying shrinkage can't take place. Once the hardened inorganic polymer in the late stage is uncovered, the drying will start. The sudden humidity change of the covered 100% humidity inorganic polymer to a much lower humidity of the environment can give a humidity shock (Scherer, 1987). The sample can't adapt fast enough to the change in humidity and Kirschner and Harmuth (2004) states that the capillary pore pressure build-up will be too fast. This fast pressure build-up can result in a large number of cracks (Kirschner and Harmuth, 2004).

2 Part 1: Change in crack characteristics: research on pastes

The first research part will cover the crack characteristics for each activating solution with another $\text{H}_2\text{O}/\text{K}_2\text{O}$ ratio. With respect to the compressive strength, an optimal $\text{H}_2\text{O}/\text{K}_2\text{O}$ ratio with the smallest number of cracks should be found. The cracks of each inorganic polymer paste, made from a different $\text{H}_2\text{O}/\text{K}_2\text{O}$ ratio, will be described and compared with the other ratios. First of all, the best curing condition that gives the least number of cracks needs to be found.

2.1 Methods part 1

To acquire the preferred grain size of the plasmastone, a correct blaine size needs to be found first. Afterwards, the activating solutions are prepared with the different $\text{H}_2\text{O}/\text{K}_2\text{O}$ ratios. The activating solution and the plasmastone are mixed and each batch of pastes is cured at a different curing condition. Once the inorganic polymer pastes are cured, SEM, fluorescence and optical microscopy are performed to get a global image of the extension of cracks for each paste. At the end BET is performed, to have an idea about the nanoporosity.

2.1.1 Blaine size

The obtained plasmastone is still wet due to the quenching and milling procedure. Therefore, the plasmastone needs to be dried before it can be milled to obtain the preferred grain surface. The plasmastone is dried at 100°C in an oven and afterwards put in the Atritor mill with zirconium balls for 12 to 14 hours. Once the plasmastone is milled, it is ready to be used for paste preparation. The smaller the grain size, the more surface is available to react with the activating solution. The plasmastone grains have an average surface area of $4400 \text{ cm}^2/\text{g}$.

The grain surface area is measured by the Blaine method. A specific amount of plasmastone is weighed, pushed in a canister and put on top of a U tube. The liquid in the U tube is brought in imbalance, as can be seen on Figure 14. When the pressure is released in the tube, the liquid in the U tube will go back in equilibrium as a result of the air that goes through the canister. The finer the grain size, the more time is needed to reach equilibrium, as there is more friction of the air with the grain surface. The time interval to bring the liquid back in equilibrium is measured. The Blaine size in cm^2/g can be calculated with the measured time and in combination with the weight of the plasmastone in the canister.

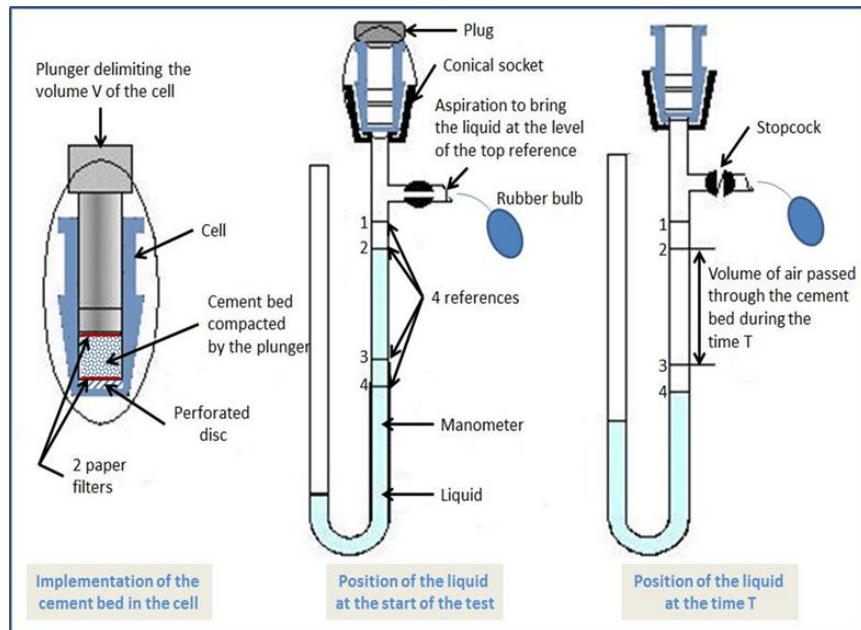


Figure 14: The left drawing shows the canister or cell where the plasmastone is put inside. This canister is put on top of the U tube. The middle picture shows that the liquid is brought in imbalance by sucking the air out of the tube. Afterwards, the time period of the air going through the canister is measured until the liquid reaches a reference level. (Piccinin, 2016)

2.1.2 Sample paste preparation

2.1.2.1 Creation of a paste for each water ratio

The activating solution is a Woellner made solution. The solution consists of a mixture of 22.5 wt% K_2O , 22.5 wt% SiO_2 and 55 wt% H_2O . This solution was put under high temperature conditions. In these conditions, $KSiO_3^-$ and silica chains are produced. The Woellner solution has a SiO_2/K_2O ratio of 1.6. The 55 wt% of water will increase when adding more water to the solution for each sample. The range in dilution of the solution will start from 55 wt% water up to 95 wt% water, with an interval of 5 wt% water, as can be seen on Table 2.

In the next step, the plasmastone will be weighted. 320 grams of plasmastone will be taken for each water ratio solution. 112 grams of the 55 wt% water in the activator will be weighted which coincides with a volume of 76 ml. This volume will stay the same for all water ratios. A constant volume will result in a decrease in mass when the solutions are more diluted. The decrease in mass is explained by the lower water density, in comparison with the K-silicates density of the activating solution. Therefore, the liquid over solid mass ratio will be lower when more water-diluted solutions are used. The volume of 76 ml for the activating solution

will be mixed with the 320 grams of plasmastone to produce an inorganic polymer paste. On Table 2, the ratios for volume and mass are given for each water ratio. The density of the plasmastone is 3.138 kg/m³.

H₂O/K-silicates ratio (wt%) in activator	Sample code humidity chamber	Density solution (g/cm³)	L/S (V/V)	L/S (m/m)	H₂O/K₂O molar
55%	55B	1.47	0.75	0.35	12.91
60%	60B	1.39	0.75	0.33	15.85
65%	65B	1.33	0.75	0.32	19.62
70%	70B	1.26	0.75	0.30	24.65
75%	75B	1.22	0.75	0.29	31.70
80%	80B	1.17	0.75	0.28	42.26
85%	85B	1.12	0.75	0.27	59.87
90%	90B	1.06	0.75	0.25	95.09
95%	95B	1.02	0.75	0.24	200.75

Table 2: While the volume is kept constant to ensure the wettability of the grains, the mass decreases with increasing water ratio.

Plasmastone and the activating solution will be mixed for 3 minutes and afterwards poured in sample holders. These sample holders are silicone cube holders and have a size of 1 cm^3 and of $2.5 \times 2.5 \times 2.5\text{ cm}^3$ or 15.625 cm^3 . An example of a 15.625 cm^3 sample is given on Picture 1. The small 1 cm^3 holders, illustrated on Picture 3, will be used for SEM and compressive strength measurements. The 15.625 cm^3 cubes, illustrated on Picture 2, will be used for microscopy on the sample side surface and to make polished sections. Five 15.625 cm^3 cubes and seven 1 cm^3 small cubes are prepared for each water ratio twice because two curing conditions are performed.



Picture 1: An example of a $2.5 \times 2.5 \times 2.5\text{ cm}^3$ cube. A piece is broken off to show the interior of the paste.



Picture 2: The left picture 2 shows silicon cube holders of $2.5 \times 2.5 \times 2.5\text{ cm}^3$. Picture 3: The right picture 3 shows silicon cube holders of 1 cm^3 . Both are covered by a plastic foil to prevent evaporation.

2.1.2.2 Curing conditions and evolution

One batch of samples is put in the climate curing chamber at a constant temperature of 23°C . The relative humidity in the first 10 days is 85%. After these 10 days, the relative humidity is lowered to 65%. The other batch of samples is placed in boxes and sealed off. These boxes are put in a room with a constant temperature of 23°C . A humid cloth is put in the box to guarantee a 100% relative humidity for the whole curing period. In this case, evaporation will be avoided when curing. After 28 days, the humid tissues are removed from

the boxes. In the following step, the samples are aerated for 14 days. The samples are all dry 15 days after the opening of the boxes. Afterwards, the samples will be demoulded.

2.1.3 Cracks observation techniques

2.1.3.1 *Microscopy on pastes and polished sections*

The crack and shrinkage features on the side surface of the $2.5 \times 2.5 \times 2.5 \text{ cm}^3$ samples are described macroscopically and microscopically after 45 days of curing. The cracks on the samples for each water ratio and for each curing condition are compared by optical microscopy at incident light.

Polished sections are prepared from the samples of each water ratio from each curing condition. The polished sections of each curing condition are compared with each other via fluorescence and optical microscopy. Polished sections of the samples are prepared by the following steps. First, the inorganic polymer paste is sawed vertically in two pieces. Afterwards, a green colored resin is placed on the inner face, on the sawn surface of the samples. This resin impregnates the sample surface. A low temperature resin is chosen because a hot impregnation that is placed at vacuum pressure could induce cracks. Once the resin is hard, the impregnated surface is polished.

2.1.3.2 *Scanning Electron Microscope (SEM) -XL30 FEG*

The Philips XL30 FEG SEM will be used to observe the scale of the cracks, the concentration of cracks and the amount of polymerisation for each sample. The 1 cm^3 samples will be put in a vacuum canister. The vacuum canister will perform low vacuum conditions of 10^{-2} bar. With this procedure, the samples will already get accustomed to vacuum conditions before bringing the samples in the EM vacuum chamber at 10^{-6} bar. Hereby, a vacuum shock will be avoided to prevent the formation of cracks. An electrolyte solution and Pt coating will be applied on the samples to divert the fired electrons on the sample in the EM chamber. The EM will provide high resolution pictures from $500 \text{ }\mu\text{m}$ up to $2 \text{ }\mu\text{m}$. The SEM analysis is carried out on the side surface of the 1 cm^3 paste samples.

2.1.3.3 *Compressive strength measurement*

The compressive strength measurement is carried out by the Instrum 5985 device with a load rate of 0.5 mm/min. A vertical load, which exercises a pressure, is applied on the samples. The pressure is increased until it exceeds the strength of the samples. At that point, the ultimate compressive strength is reached and beyond that point, the material fails by forming cracks.

2.1.3.4 *BET: Nitrogen adsorption technique*

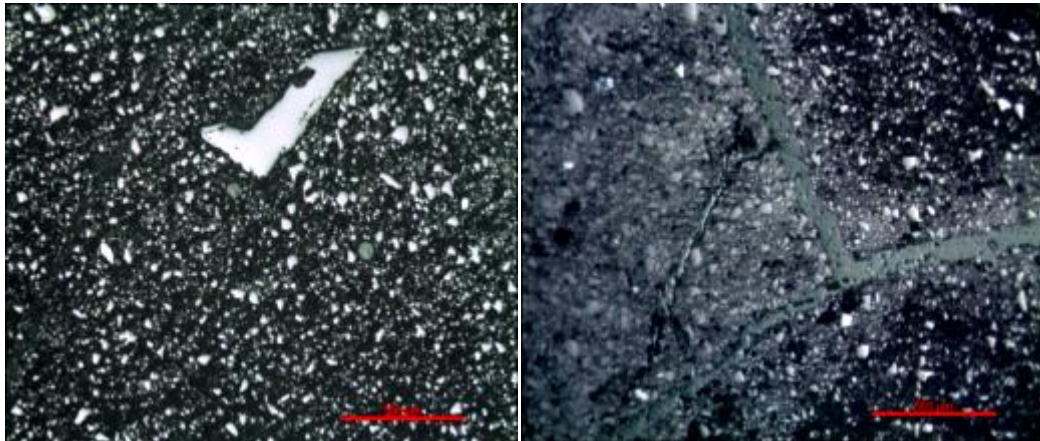
A Brunauer, Emmett and Teller (BET) test is performed to get a quantification of the nanoporosity evolution of the inorganic polymer paste samples (Jennings et al., 2007). The BET test will be issued only on the inorganic polymer paste samples that were cured in the humidity chamber. The porosity, which includes the cracks, is measured by injecting the non corrosive nitrogen gas in the sample. The nitrogen gas molecules will get physically adsorbed by van der Waals forces on the solid surface of the pores and cracks of the sample. The adsorption and desorption procedure is carried out for at least 3 times with successive higher pressure values, starting at the liquid temperature of nitrogen, up to a specific defined point. The amount of gas adsorbed and desorbed on the surface is measured by a volumetric or continuous flow procedure (Analytical, 2016). The desorption pore size distributions are calculated by the Barrett-Joyner-Halenda (BJH) method (Steins et al., 2014).

In this way, the BET specific surface area, which corresponds with a monomolecular layer of gas that is adsorbed on that surface, can be deduced with a multi-point analysis technique. A data sheet of the incremental and cumulative pore volume for each pore width will be received (Analytical, 2016; Thomassen, 2011). The BET experiment is limited for a minimum pore width of 1.5 nm up to a maximum pore width of 64 nm. The analysis of the BET technique is carried out by the TriStar apparatus at -195°C.

2.2 Results part 1

2.2.1 The choice of a preferred curing condition

With optical microscopy can be observed that the 100% humidity cured $2.5 \times 2.5 \times 2.5 \text{ cm}^3$ samples have a high number of macro-cracks on the surface. These cracks can be followed throughout the samples in the polished sections. Picture 5 shows the macro-cracks of a 100% humidity cured sample, while Picture 4 doesn't show macro-cracks in the humidity cured sample. The large amount of macro-cracks can be explained by the theory of Kirschner and Harmuth (2004). They state that the macro-cracks can be generated by the induced humidity shock when aerating the samples. Consequently, the research on cracks will be focused on the humidity chamber cured inorganic polymer pastes because they have the least number of macro-cracks.



Picture 4 and 5: The left picture shows the matrix of a 80 wt% water inorganic polymer paste matrix, cured in the humidity chamber. The right picture visualizes the matrix of a paste with an extensive crack network made with the same water ratio, but cured in 100% relative humidity boxes.

2.2.2 Crack description of the humidity chamber cured inorganic polymer pastes

SEM is conducted on the side surface of the 1 cm³ pastes after 40 days of curing. Optical microscopy is executed on the polished sections. A detailed description of each sample is given in the appendix, along with the SEM pictures. The summary on Table 3 comprises the different crack lengths. 1st order cracks are the largest cracks found throughout the matrix of the sample. 2nd order cracks are the second largest cracks in the sample. The 3th and 4th order cracks are the smallest cracks in the sample. In specific zones, like in voids, cracks of several 100 µm can still be observed, as can be seen in sample 75B and 80B. These cracks don't occur throughout the sample and are not mentioned on Table 3.

Next, the type of crack pattern can be observed in the samples. Solitaire cracks don't have a specific repetitive crack pattern, but are more random widespread cracks. A circular crack network pattern, with 3, 4 or 5 angles and each angle is 120°, is called a desiccation crack pattern. The relief and the void size can be determined from the polished sections via optical microscopy. In some samples, cracks originate from the voids and connect other voids. Sample 95B couldn't be examined because the sample was too soft to make a polished sample and the sample wouldn't stick on the SEM sample holder.

Sample	SEM						Optical microscopy polished section		
	Macro-cracks		Meso-cracks	Micro-cracks		Specific crack type in matrix	Grains in matrix, relief	Void size in matrix	Cracks connect voids
	>100 µm	50-100 µm	10-50 µm	5-10 µm	1-5 µm				
55B	1 st order	2 nd order	3 th order	4 th order	/	Desiccation pattern	/	< 500 µm	Yes
60B	1 st order	2 nd order	3 th order	4 th order	/	Desiccation pattern	/	< 250 µm	Yes
65B	1 st order	2 nd order	3 th order	4 th order	/	Desiccation pattern	/	< 250 µm	Yes
70B	Two cracks	1 st order	2 nd order	3 th order	4 th order	Desiccation pattern	Some grains	< 100 µm	Yes
75B	/	/	1 st order	2 nd order	3 th order	Solitaire	Some grains	< 100 µm	No
80B	/	/	/	1 st order	2 nd order	Solitaire	High relief	< 50 µm	No
85B	/	/	/	1 st order	2 nd order	Solitaire	High relief	< 50 µm	No
90B	/	/	/	/	1 st order	Solitaire	High relief	<50 µm	No

Table 3: A summarizing table, which consist the most important features of cracks, void type and void size in the matrix.

2.2.3 Compressive strength results

Compressive strength measurements are performed on the samples after 40 days of curing. Their results are plotted on Figure 15. A high compressive strength is measured for the samples 55B up to 75B. From sample 75B up to 95B, a strong decrease in compressive strength can be noticed. The compressive strength of sample 80B is only half the strength of sample 75B.

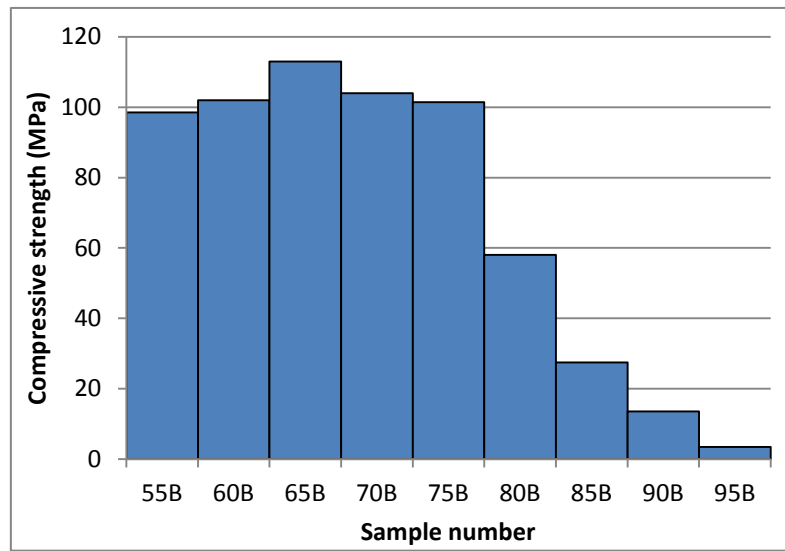


Figure 15: This figure represents the compressive strength measurements of the inorganic polymer pastes for different water ratios after 40 days of curing

2.2.4 BET specific surface

The pastes 55B, 60B, 90B and 95B have a very low specific nanopore surface area. Figure 16 shows a high amount of specific surface for samples 70B, 75B and a in some extend for 80B. Once passing this high amount or optimum at sample 75B, a constant decline is visible until 85B. The desorption cumulative volume shows a similar course for each paste. Sample 75B could not be plotted on Figure 17, because good data couldn't be obtained. Figure 17 represents the cumulative pore volume for each sample, determined by the desorption technique. The cumulative volume indicates the total measured volume for all nanopores. On Figure 17, an optimum in cumulative pore volume is visible as well.

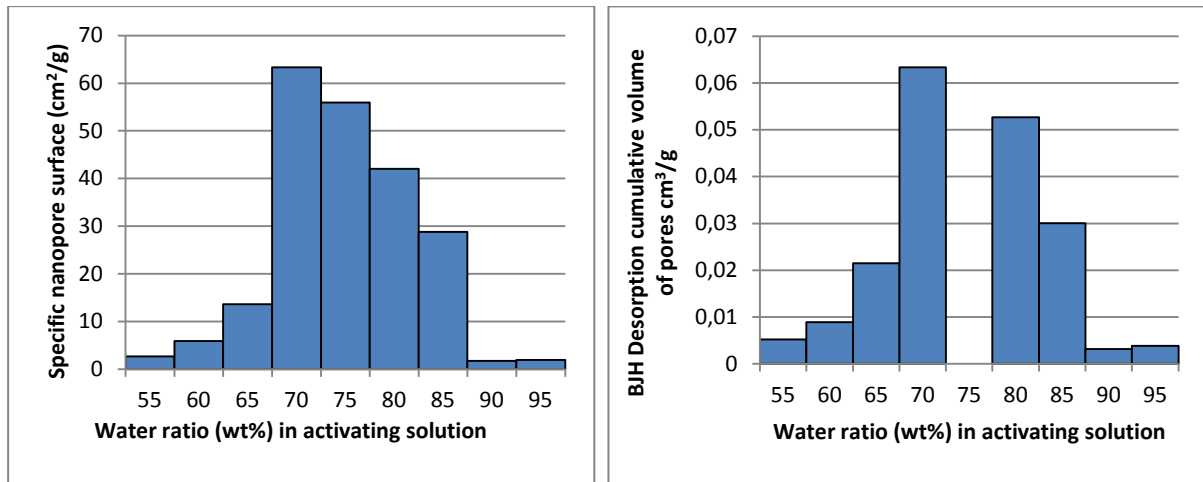


Figure 16 and 17: Figure 16 represents the surface area of the nanopores for each paste. Figure 17 gives the volume of pores by desorption.

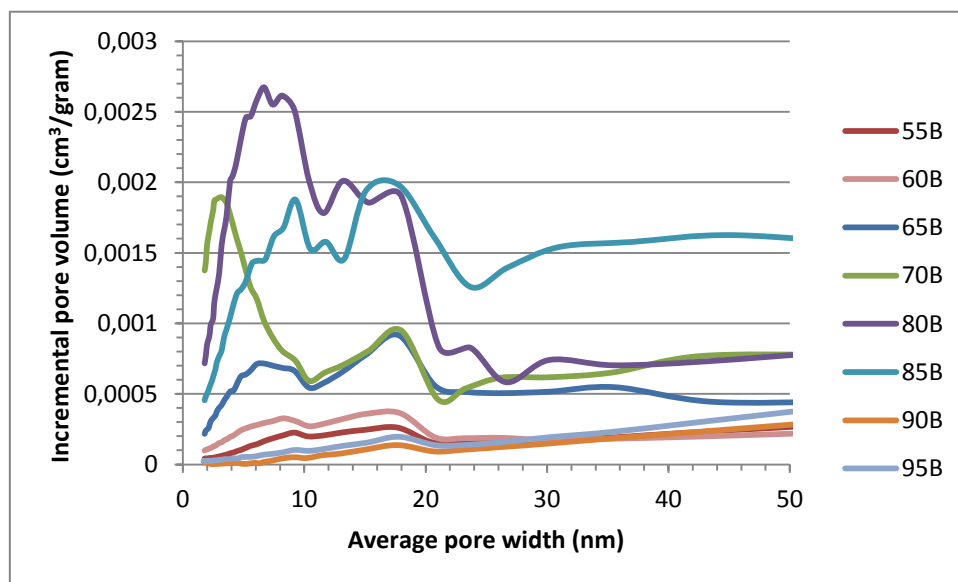


Figure 18: This figure represents the incremental pore volume, for each pore width and for pastes with different water ratios.

The results of sample 75B show unrealistic pore volume data, these values are not plotted on Figure 18. The incremental pore volume indicates how many pores of a specific pore width or size occur. Sample 70B has a peak in incremental pore volume at a pore width of 3.9 nm. Samples 80B and 85B have a high pore volume with a pore range width from 7.4 nm up to 17.8 nm. Consequently, most pores have a pore width that occur in this range of pore width. In general, most pores occur with a width of 4-18 nm. Samples 55B, 60B, 95B and 95B have the lowest pore volume for each pore size.

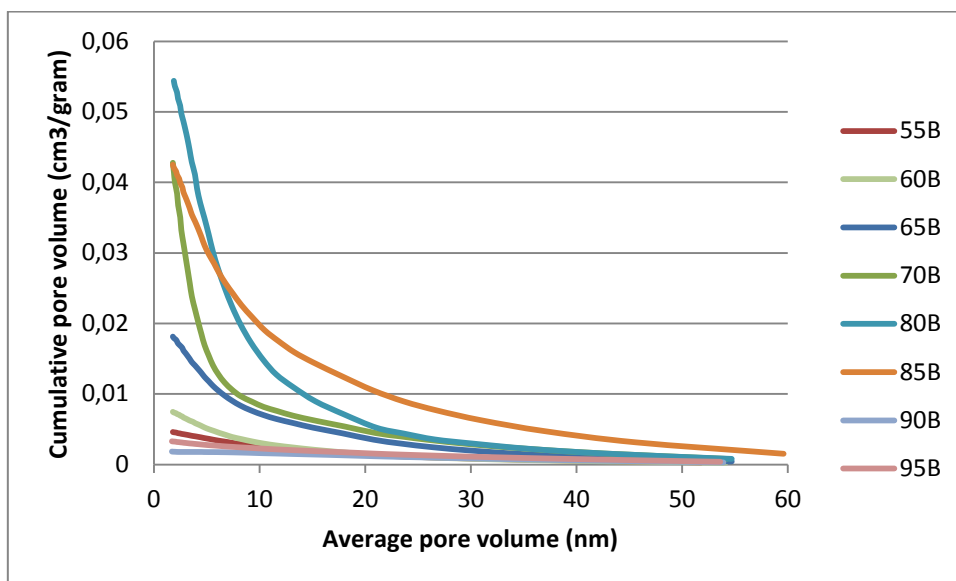


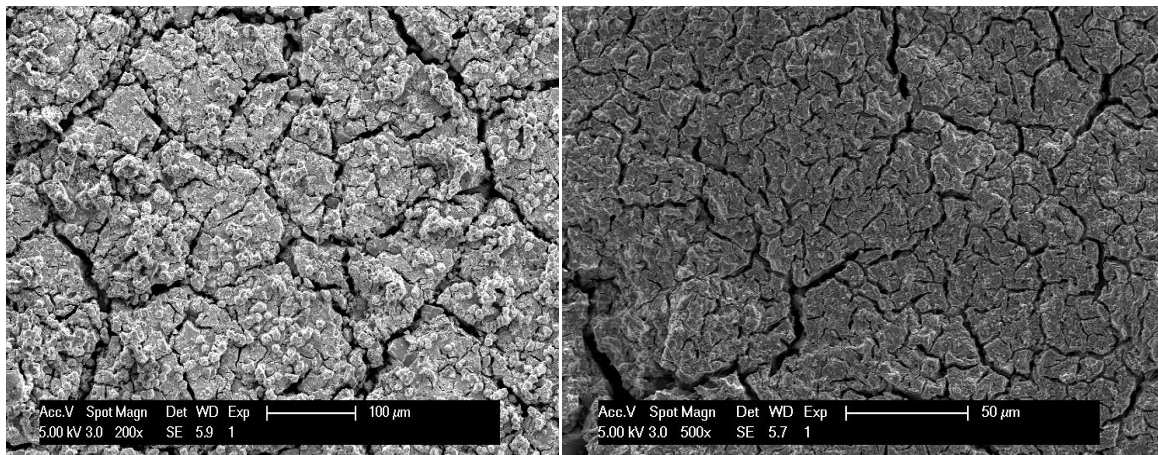
Figure 19: This figure represents the cumulative pore volume with the average pore width for each sample.

As can be seen on Figure 19, samples 55B, 60B, 90B and 95B have an overall small amount of pore volume. Samples 80B and 85B have the highest cumulative pore volume. Most pores occur in the range of pore width from 1 nm up to 20 nm. Sample 75B couldn't be plotted because the measurement gave incorrect data.

2.3 Discussion part 1

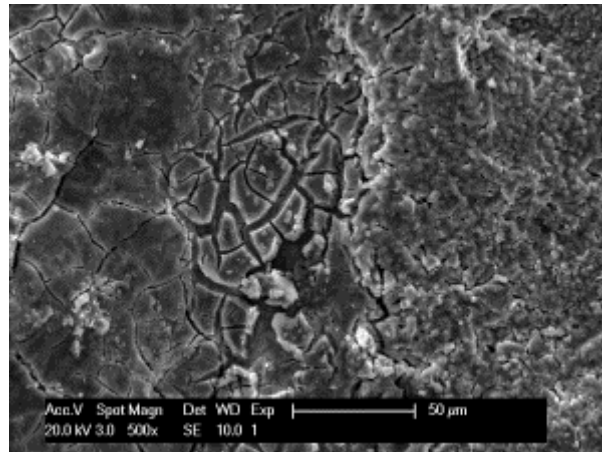
2.3.1 Explanation of the observed crack types

Desiccation cracks are similar to mudcracks. This type of crack is very good visible at the top surface of sample 55B, seen on Picture 6 and at the side surface of sample 65B, seen on Picture 7. These cracks can be formed when the samples are drying. In this case, the water will retreat in the interior and capillary pressure will increase at the surface (Scherer, 1988). This capillary stress has a uniform distribution in the weak zones, with an angle of 120° . Once the stress exceeds the strength of the weak zone, a specific uniform repetitive crack pattern is formed.



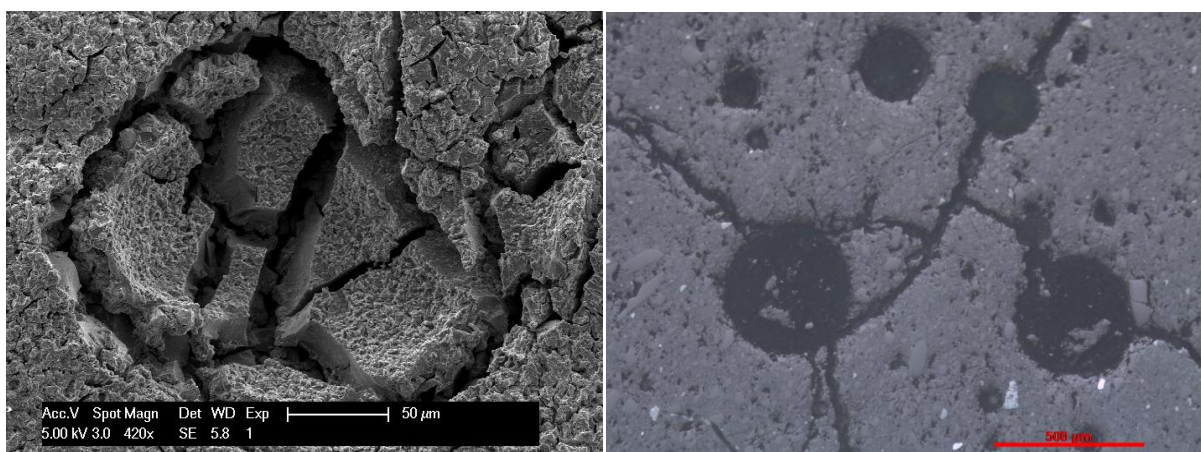
Picture 6: Desiccation cracks in a weak zone due to drying in sample 55B. Picture 7: The right picture shows a uniform circular desiccation crack pattern in sample 65B.

Samples 55B and 80B are good examples of concentrated crack zones. These concentrated cracks are situated in zones with a different texture than the matrix, as illustrated on Picture 8. Machiels et al. (2014) states in his paper that some zones can be enriched in certain chemical elements like Fe, Ca and K. The difference in chemistry results in a different stress regime in comparison with the stress of the surrounding matrix. These differential stresses create cracks in zones with a low strength and inorganic polymer development (Machiels et al., 2014; Scherer, 1987).



Picture 8: Three different types of crack zones on the surface of sample 80B.

Samples 55B, 60B and 65B contain a large number and a large size of voids because a significant amount of water stays trapped in the fast forming interior network of the matrix (Scherer, 1988). The number and the size of the voids are smaller for samples 80B, 85B and 90B because the liquid is less viscous and the water will have more time to escape out of the network. The voids in samples 55B, 60B and 65B are often heavily cracked inside, or form a launch path for cracks to originate from. Scherer (1987) interprets that high stresses are exercised on the voids, as a result of the concave shape of the void. These high stresses rip open the voids and result in short but wide cracks inside the voids. An example is given on Picture 9. Consequently, cracks are formed from these voids, which will connect other voids in order to release the stress of the voids. An example of this phenomena is given on Picture 10.



Pictures 9 and 10. The left picture 9 represents a void in the matrix of 60B that is internally heavily cracked. The right picture 10 of sample 60B shows that the voids are connected by cracks.

2.3.2 Interpretation of the general characteristics of inorganic polymer pastes

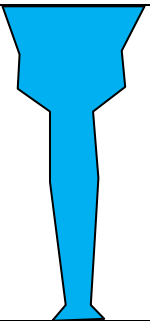

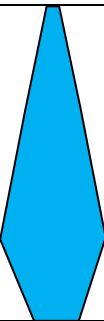
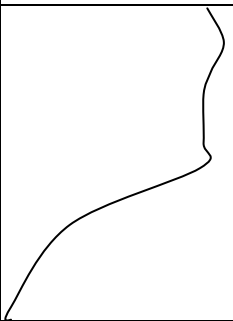
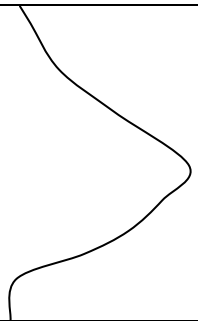
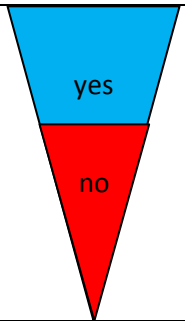
Sample code	Macro cracks >100-50μm	Meso cracks 50-10 μm	Micro cracks 10-1μm	Strength (MPa)	BET specific surface (m ² /g)	Cracks connect voids
55B						
60B						
65B						
70B						
75B						
80B						
85B						
90B						
95B						
	Relative proportion			Low ----- High	Low ----- High	Size/amount

Table 4: A general evolution of the cracks, strength, BET specific surface and voids of the inorganic polymer pastes are given from a low to a high water ratio in the solution.

Table 4 shows a general overview of the cracks, the compressive strength, the specific nanopore surface, the amount and size of voids of all the pastes with a different water ratio in the activating solution. These characteristics can be linked to each other.

Macro-, meso- and micro-cracks are observed in the samples. The formation of a specific type of crack can depend on the strength properties of that sample. Samples 55B, 60B and 65B have a large proportion of macro-cracks and high strength properties, of more than 100MPa. According to Eppers (2010), the capillary pore can build-up a high amount of pressure in order to exceed these high strength properties. Kirschner and Harmuth (2004) interprets that once the pressure exceeds the high strength, a crack can be produced. Macro-crack are probably generated by the high energy release of a high capillary pressure.

Samples 80B, 85B, 90B and 95B have a large proportion in micro-cracks and almost no macro-cracks. These samples have low strength properties. In this case, the capillary pore pressure can exceed the strength of the sample easily. The release of a low capillary pore pressure can generate micro-cracks according to Eppers (2010). The inorganic polymer pastes of 85B, 90B and 95B don't have enough strength to bind the paste and the undissolved grains together, as shown on the SEM pictures and on Figure 15 for compressive strength. This results, according to Provis (2013), in the production of micro-cracks alongside the undissolved grains, as illustrated on the SEM pictures.

A clear change in crack characteristics is visible from sample 65B up to sample 80B. The proportion of macro- and meso-cracks decreases, as can be seen on the SEM pictures. The decrease in macro-cracks can be the result of the decrease in capillary pore pressure build-up. Evidence for this decrease in stress build-up can be seen on the existing voids in the paste. Cracks do not connect the voids anymore to release the high stress build-up of the voids.

Samples 85B, 90B and 95B are too water-diluted and exceed the optimum of the paste properties. The alkalinity is too low to dissolve the grains, so the matrix becomes grain supported, with a paste between the grains (Bentz and Jensen, 2004). The grainy surface or relief in the interior and exterior surface is a perfect example of a bad dissolution of the plasmastone. The samples have a very low strength development because a proper inorganic polymer can't develop according to Bentz and Jensen (2004).

The lack of water in samples 55B, 60B and 65B and the strong presence of potassium, can result in short K-Al-Si chains (Rees et al., 2007). The short silica chains will lead to a fast oversaturation in the solution. Consequently, the formation of an inorganic polymer network will start early because of the intense reaction, but the extend in polymerisation will stay low, according to Kriskova et al (2015). The formation of a low quality inorganic polymer in samples 55B, 60B and 65B is also supported by the amount specific surface and adsorption volume of the nanopores, as can be seen on Figures 16 and 17.

The number of nanopores would be driven by the amount of polymerisation. This theory can be support by the paper of Jennings et al. (2007) for CSH gels. A large number of nanopores in samples 70B, 75B and 80B can be the result of a large amount of formed inorganic polymer. The activating solution of samples 70B, 75B and 80B provide enough water and alkalis to dissolve the plasmastone grains and to transport these ions in the matrix. In this way, oversaturation can be reached in the matrix, along with cross linking to produce an extend inorganic polymer network. The specific surface of nanopores reduces significantly in samples 85B, 90B and 95B because of a low amount in polymerisation.

2.4 Conclusion part 1

The inorganic polymer pastes, from sample 70B up to 75B, with a $\text{H}_2\text{O}/\text{K}_2\text{O}$ molar ratio from 25 up to 35 has the smallest number of macro-cracks, with a minimum of required strength and a high amount of formed inorganic polymer. An activating solution with a water ratio of this optimum can give proper results to form an industrial applicable inorganic polymer. Any lower $\text{H}_2\text{O}/\text{K}_2\text{O}$ ratio will result in a lower amount of formed inorganic polymer and the formation of a high number of macro-cracks. Desiccation cracks are formed and the cracks connect the voids throughout the sample. Any higher water ratios will result in a very low amount of polymerisation with undissolved grains in the matrix and a lack of strength. Macro-cracks are not formed in these samples with a high water ratio.

3 Part 2: Crack and Shrinkage evolution in time on mortars

In the second part, research will be conducted on the effect of the H_2O/K_2O ratio on the early age properties of inorganic polymer mortars. These properties consist of strength evolution, setting time, calorimetry and the Young modulus of elasticity. These properties will be linked to the results of cracks and shrinkage experiments to clarify the driving forces of shrinkage and cracks in time. The acoustic emission experiment will count the number of cracks, while the Linear Variable Differential Transformatior (LVDT) device will measure the shrinkage in time.

3.1 Methods part 2

3.1.1 Mortar preparation

Mortars are created with a water ratio of 60wt%, 70wt%, 80wt% and 90wt% in the activating solution. In the first stage, the paste is produced. The plasmastone with a Blaine size of 4000 g/cm^3 and the activating solution are mixed in a Hobart mixer at low velocity for one minute. In the second stage, a CEN_SAND type of sand aggregates is poured in the paste, while mixing for one minute at low velocity. Afterwards, the mixture is mixed for another minute at high velocity. After mixing, the mortar is cast in the mould. The volume of the activating solution stays constant but the weight changes according to the H_2O/K_2O ratio, as can be seen at the L/S column on Table 5. The L/S ratio of the mortars for each water ratio will be used for all experiments in part 2.

Mortar number	Water ratio (wt%) in activator	L/S (m/m)	L/S (V/V)	Plasmastone/sand	Density solution (g/cm^3)	H_2O/K_2O molar	pH
60M	60	0.44	0.91	0.41	1.39	15.85	14.28
70M	70	0.40	0.91	0.41	1.26	24.65	13.74
80M	80	0.37	0.91	0.41	1.17	42.26	13.46
90M	90	0.34	0.91	0.41	1.06	95.09	13.10

Table 5: The ratios of each substance, in order to prepare the inorganic polymer mortars for each water ratio. Each mortar of a different water ratio receives a mortar number.

3.1.2 Flexural and Compressive strength measurement

Six mortars are created for each water ratio to conduct compressive and flexural strength measurements. The mortars are cast in six moulds, each with a size of 4 x 4 x 16 cm³. After casting, the mortars are wrapped in a plastic foil for one day. At the second curing day, the mortars are unwrapped and put in plastic boxes until the day of testing. An amount of 1100 grams of plasmastone and 2700 grams of sand are used for each water ratio. The flexural and compressive test is measured after 2, 7 and 28 days of curing.

The compressive and flexural strength measurement is carried out by the Instrum 5985 device, at a rate of 0.5 mm/min flexural extension. The mortar is put in a three-point bending device, as shown on Picture 11, to measure the flexural strength. A load is gradually increased until the mortar cracks into two pieces. Afterwards, these two pieces are put in the compressive device. A pressure load is gradually increased on the sample until the pressure exceeds the strength of the mortar. At that braking point, the mortar is shattered in pieces and the strength of the mortar is lost. This way, the compressive strength of the mortar can be measured. A scattered mortar can be seen on Picture 12.



Pictures 11 and 12: The flexural strength is exercised on the mortar on picture 11. A mortar is scattered into pieces on picture 12 after it reached its maximum compressive load.

3.1.3 Calorimetry with an admix ampoule

A calorimeter (TAM Air device, TA Instruments) measures the reaction kinetics in terms of heat flow or released heat (J) in the inorganic polymer paste at 293 K (Kriskova et al., 2015). First, an amount of liquid is weighed and put in the admix ampoule. In the next step, the corresponding amount of plasmastone powder is brought into the canister. Further, the admix ampoule is placed on the canister and brought into the calorimeter, next to an empty canister used for standard calibration. After four hours of calibration, the liquid can be mixed

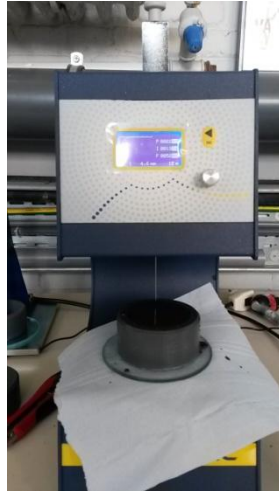
in situ with the powder in the canister. The calorimeter starts recording the heat flow generated from that moment. After 24 hours of monitoring, the sample is removed and the next sample with a different water ratio can be put in the calorimeter. This test is done for each water ratio, with the same L/S as the mortars on Table 5. The results are given in heat flow W and will be converted to Joule/(gram x hour) by dividing every sample by its weight. The total weight can be found on Table 6.

Sample code	Plasmastone (gram)	Activator (gram)	Total (gram)
60M	3.72	1.65	5.37
70M	3.77	1.50	5.27
80M	3.55	1.30	4.85
90M	3.54	1.20	4.74

Table 6: The weight of each sample is used for the calculation to Joule/gram.

3.1.4 The Vicat test

The Vicat penetration test will be performed next. The EN-UNI 196-3 standard penetration scheme is used with the Vicatronic automatic vicat recording apparatus. The paste is cast in a circular sample holder and placed under the pin of the Vicat device, as can be seen on Picture 13. The same L/S ratios are used as for the mortars on Table 5. An amount of 400 grams of plasmastone is used for the production of every paste. The time is being recorded from the moment of casting, until the paste is completely set or hard. At certain pre-set time periods the pin will fall into the paste with the gravitational falling speed. Each time, the penetration depth will be measured. 26 penetrations are taken to measure the evolution of penetration depth of the paste. 86 penetrations are taken for sample 90M because of the long hardening time. The penetration depth can be correlated with the setting time of the paste.



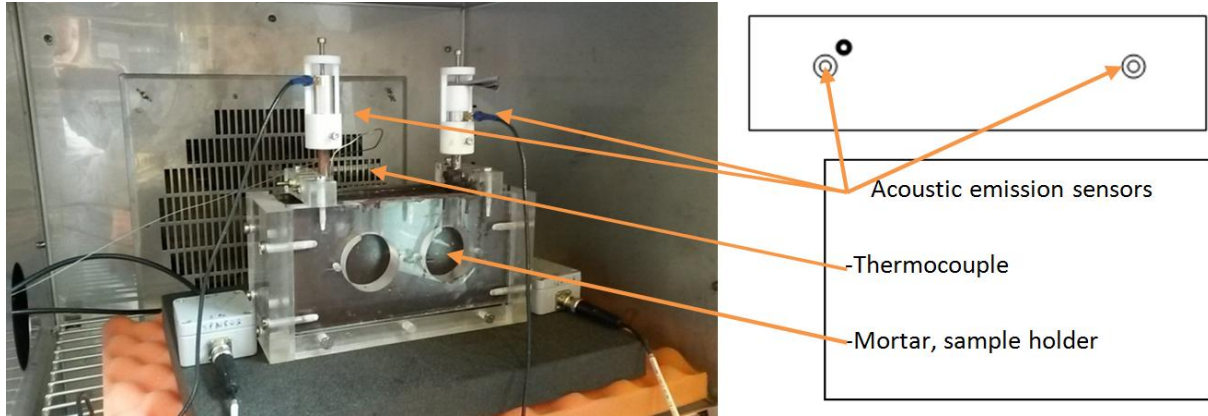
Picture 13: The Vicat device with the sample placed underneath the pin. On top of the pin, a weight is fixed to give the proper falling speed. The tests are carried out with pastes, no sand is involved.

3.1.5 Non-destructive test: acoustic emission combined with thermocouple

Acoustic emission is the result of a strain energy release by harmonics when changes in the microstructure of materials, like inorganic polymers, occur (Van Den Abeele et al., 2009). The energy release transfers elastic waves throughout the inorganic polymer. These waves are recorded by a piezocrystal, where the acoustic wave is amplified and recorded as a hit with a specific decibel (Farhidzadeh et al., 2012). With this technique, cracks in the inorganic polymer can be monitored. The Vallen AMSY-51 device listens via a frequency of 40 kHz and 350 kHz, in which cracks or hits are collected. The software Digital Wave system will register these hits or acoustic emission events with a detection limit of 30 dB. A thermocouple is combined with the acoustic monitoring. This thermocouple measures continuously the temperature.

First, the mortars will be made. An amount of 1100 grams of plasmastone and 2700 grams of sand are used for each water ratio. The same L/S ratios will be used as on Table 5. The sample holder has a size of 20 x 10 x 5 cm³ and has two metal bars and one thermocouple that are placed in the sample. Through these bars, the acoustic waves originated from the inorganic polymer will travel to the sensors. On top of each bar, a sensitive sensor is placed, which registers the acoustics. A silicone glue is put between the bar and the sensor to have an as good as possible connection and to avoid external interference. The mortar is cast in the sample holder and put on a vibration plate for four minutes. The experimental set-up, as can be seen on Picture 14, is placed in a climate chamber (Heraeus-Vötsch Climate Cabinet

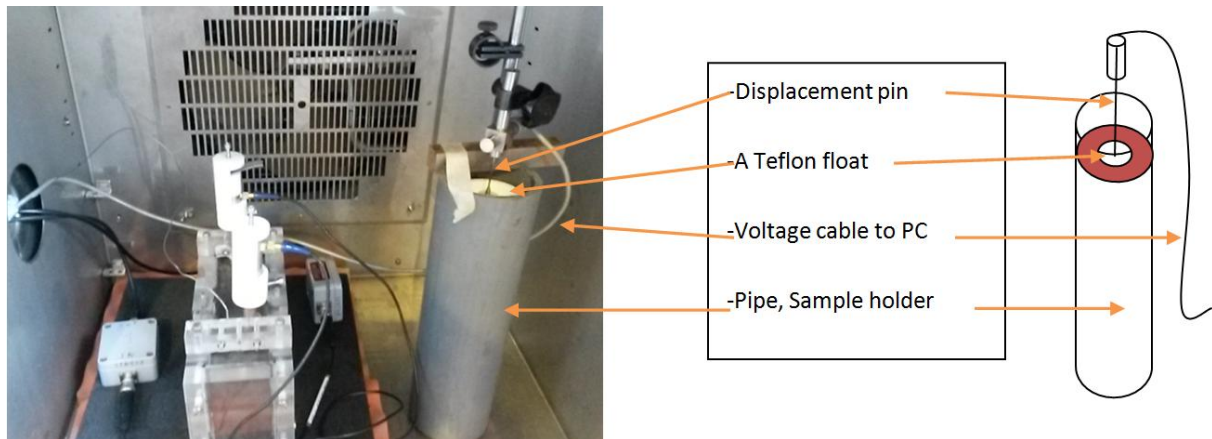
VLK 04/150). The climate chamber does not operate, but acts as an insulator for noise, vibrations, temperature variation and humidity fluctuations. The mortar will be monitored for five days before replacing it with another mortar of a different water ratio.



Picture 14: The NDT Acoustic emission experimental set-up.

3.1.6 Linear Variable Differential Transformator (LVDT)

An LVDT shrinkage test will be carried out in the same climate chamber as the acoustic emission test, as visualized on Picture 15. The mortar is cast in a pipe up to a reference height of 26.5 cm. Between the pipe and the mortar, a Teflon sheet is placed to reduce friction during shrinking or expansion. The LVDT measures a displacement that can occur when the inorganic polymer mortar undergoes autogenous and drying shrinkage or thermal expansion. The shrinkage and expansion will result in a displacement towards the reference level. The displacement is measured by a pin, connected to a Teflon plate that floats on the concrete surface, as visualized in the left part of Picture 15. The change in height or displacement of the pin leads to a change in voltage. An increase in voltage indicates shrinkage of the concrete, while a decrease in voltage results in expansion of the concrete. The measured voltage can be converted into displacement in mm/m. The displacement will be measured continuously for five days. An amount of 1650 grams of plasmastone, 4050 grams of sand and the same L/S ratios as mentioned on Table 5 are used for the combined test of the Young modulus and the LVDT. Sample 80M could not be measured due to time constraints and because the computer for recording the shrinkage was no longer available.



Picture 15: The experimental set-up of the LVDT test.

3.1.7 Ultrasonic test: Young's modulus of elasticity

Ultrasonic waves are used to evaluate the materials attenuation properties, which provides the inorganic polymer Young's Modulus of elasticity or E-modulus (Farhidzadeh et al., 2012). The attenuation is measured by emitting pulses of sound waves through the sample of $20 \times 10 \times 5 \text{ cm}^3$. The sample has on each side a circular opening to fit a transducer for emitting and receiving the ultrasonic waves. A thin film closes the opening to prevent spilling of the inorganic polymer. The transducers measure the attenuation of the shear waves in μs for a sample with a width of 0.05 m. With this data, the wave velocity can be calculated. The inorganic polymer has a total density of 2400 kg/m^3 . With the sound velocity and the density, an E-modulus can be determined in time with the following formula: $E \text{ (GPa)} = v^2 \rho$ (Azenha et al., 2012). The first moments after casting has such a high attenuation that it is impossible to receive any sound wave through the sample because the mortar is still too liquid (Farhidzadeh et al., 2012).

3.2 Results of part 2

3.2.1 Calorimetry: heat flow evolution

The calorimetry data are plotted on Figures 20 and 21. From the moment the activator is mixed with the plasmastone, a strong increase in heat flow can be noticed, which results in a peak. Samples 70M and 80M show two peaks or bumps on Figure 21. Sample 60M has the highest peak and its two peaks seems to be merged into one. Only a small bump can be noticed at sample 60M, prior to its maximum heat flow. The more water in the solution the smaller the peaks are and the more the peaks are shifted in time. Sample 90M shows no increase in heat flow. Once the reactions are finished, the heat flow will decrease exponentially for all samples.

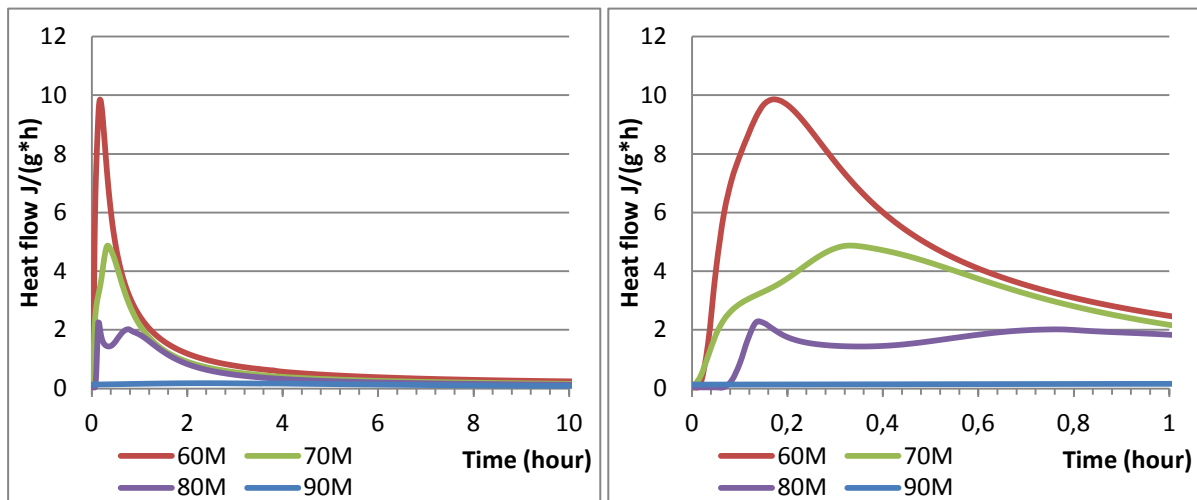


Figure 20 and 21: The evolution in heat flow with time for each mortar with a different water ratio. The right figure 21 is zoomed in on the first hour after mixing. Different peaks are visible.

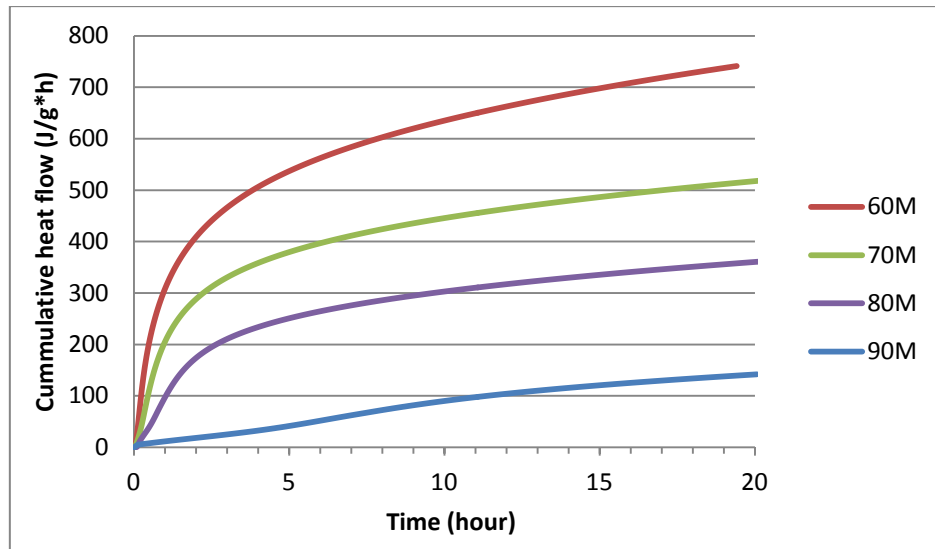


Figure 22: The cumulative heat flow in time for each mortar with a different water ratio.

The cumulative heat flow on Figure 22 shows a strong increase when mixing starts. After some hours, the increase is less strong and continues as a constant in time. A lower amount of water in the activator results in a higher amount of cumulative heat flow and vice versa.

3.2.2 The setting time via the Vicat penetration

The Vicat penetration depth results in time are visualised on Figures 23 and 24. Samples 60M and 70M seem to start setting after 33 minutes. Samples 60M and 70M have a short setting time period, from initial to final setting, of only 10 minutes, which result in a steep curve. Paste 80M starts setting after 44 minutes. Sample 80M has a setting time period of 14 minutes. Sample 80M has a delay in the start of the initial setting of 10 minutes and the setting time period is prolonged for 4 minutes compared to sample 70M. At the final setting time, the paste is completely hard. Sample 90M start to set 4.63 hours (278 min) after mixing. On Figure 24, it can be seen that the setting period from initial to final setting of paste 90M is up to 1.5 hours long. Sample 90M seem to have softer and harder parts because the setting curve is discontinuous.

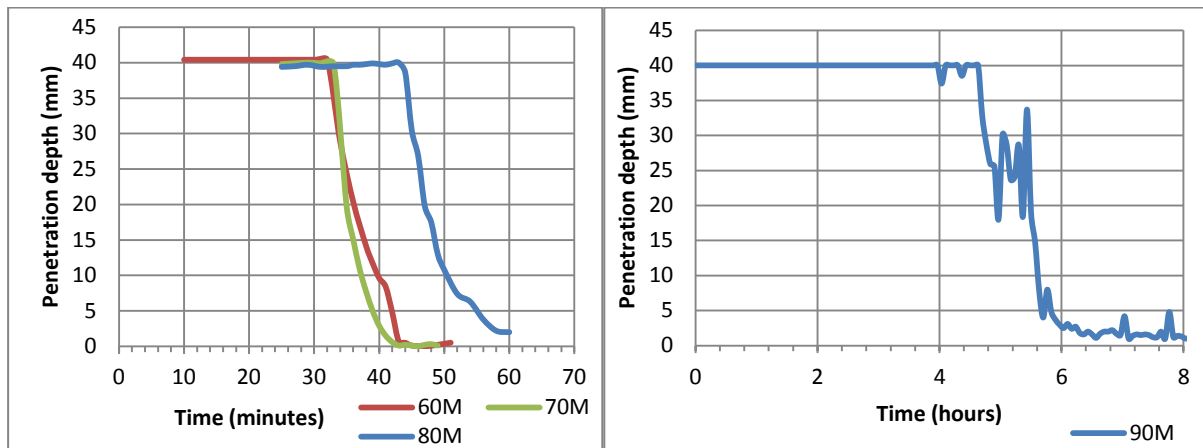


Figure 23 and 24: The penetration depth with time of samples 60M, 70M and 80M are presented on the left figure. The penetration depth with time of sample 90M is given on the right figure.

3.2.3 Elasticity-modulus evolution

The calculated data of the ultrasonic test to obtain the evolution of the E-modulus for the four different samples is plotted on Figure 25. The E-modulus start to increase at different values, sample 60M start at 0 GPa, while sample 80M start at 8 GPa. The first hours of E-modulus increase don't show a proper evolution because the background noise is still high. The increase in E-modulus start at the same time for samples 60M and 70M. Samples 80M and 90M start to have an increase in E-modulus later in time. When the activating solution is more water-diluted however, a lower elasticity value will be reached and a slower increase in elasticity will be developed. Samples 60M and 70M show, after one day, an increase in elasticity at a constant rate. Figures 47 and 48 in the appendix show the temperature peak, which agree with the start of the E-modulus.

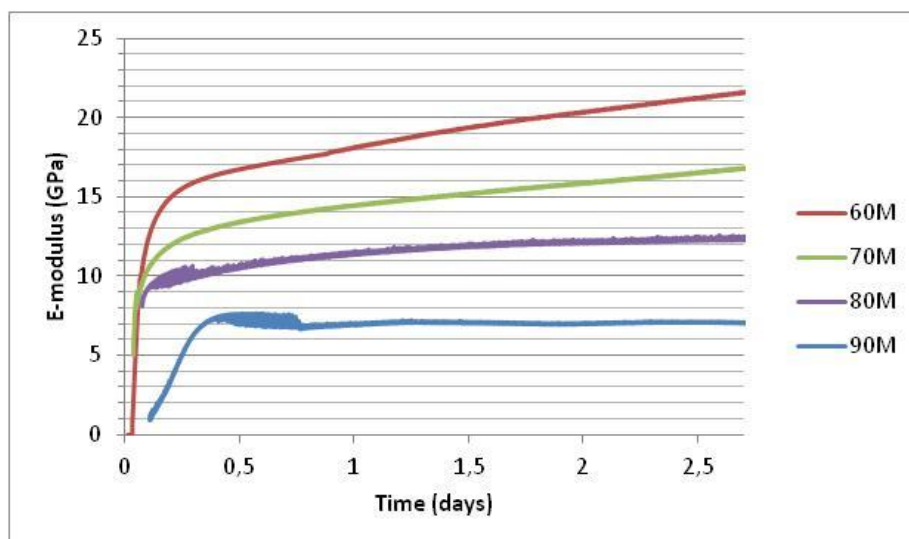


Figure 25: The evolution in E-modulus for each sample.

3.2.4 Compressive and flexural strength on mortars

The results of the compressive and flexural strength and the compressive strain (mm/mm) are given in the appendix. In general, all mortars show on Figure 26 a strength increase in time. The mortars of 60M and 70M show a significant strength increase; the strength is almost doubled after 7 days of curing. Mortar 70M also seems to catch up in strength of sample 60M. Sample 90M shows a very slow strength development.

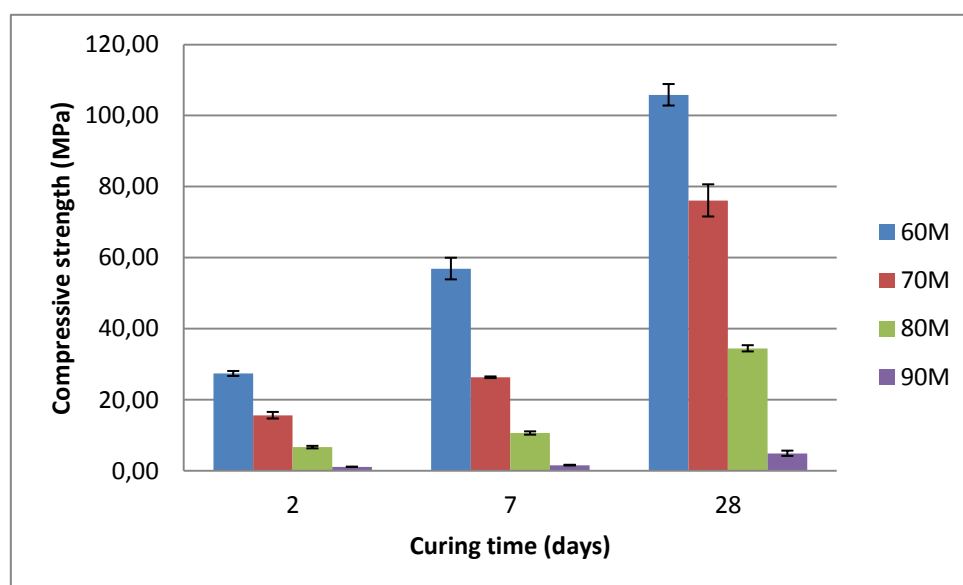


Figure 26: The evolution of compressive strength for the mortars of different water ratios after 2, 7 and 28 days of curing.

The results of the flexural strength evolution for each water ratio are given on Figure 27. An increase in flexural strength of all mortars can be observed. One mortar of sample 90M already broke into two pieces when demoulding after 2 days of curing, because this mortar has an extremely slow strength development. The difference in flexural strength between 60M and 70M is smaller after 28 days of curing. The difference between 80M and 90M on the other hand is significant.

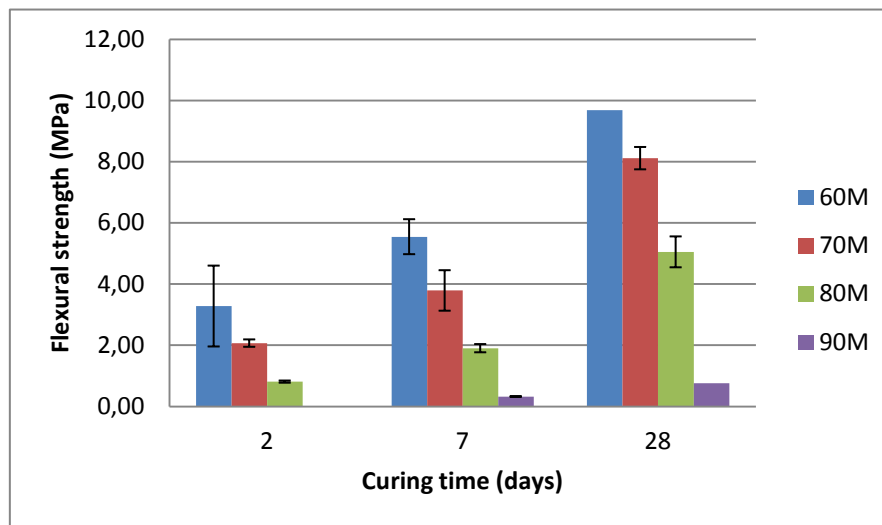


Figure 27: The flexural strength evolution of mortars with different water ratios.

3.2.5 NDT Acoustic emission

The acoustic emission displays its data in cumulative hits on Figure 28. One hit represents one crack that is formed at a specific frequency. Channel 1 has a frequency of 40 kHz and shows a constant increase in hits for all the samples. On Figure 28 it is clearly visible for every sample that the evolution in cumulative hits, especially at a frequency of 40 kHz, happens gradually in steps. Sample 60M has a low increase in hits with a total number of 200 hits after 6 days, while all other samples show 800 hits after 6 days. Channel 2 has a frequency of 350 kHz and captures less hits and evolves to a plateau. The maximum number of hits, at a frequency of 350 KHz, are around 200 after 6 days, apart from sample 80M, which has only around 100 hits. Sample 60M has a strong increase in hits at a frequency of 350 kHz during the first 12 hours of measurement.

A high temperature peak is visible for sample 60M and 70M in the beginning of the measurement. For sample 80M and 90M, this temperature peak is not visible anymore. The day and night influence is clearly visible on the temperature, with a maximum temperature difference of two degrees.

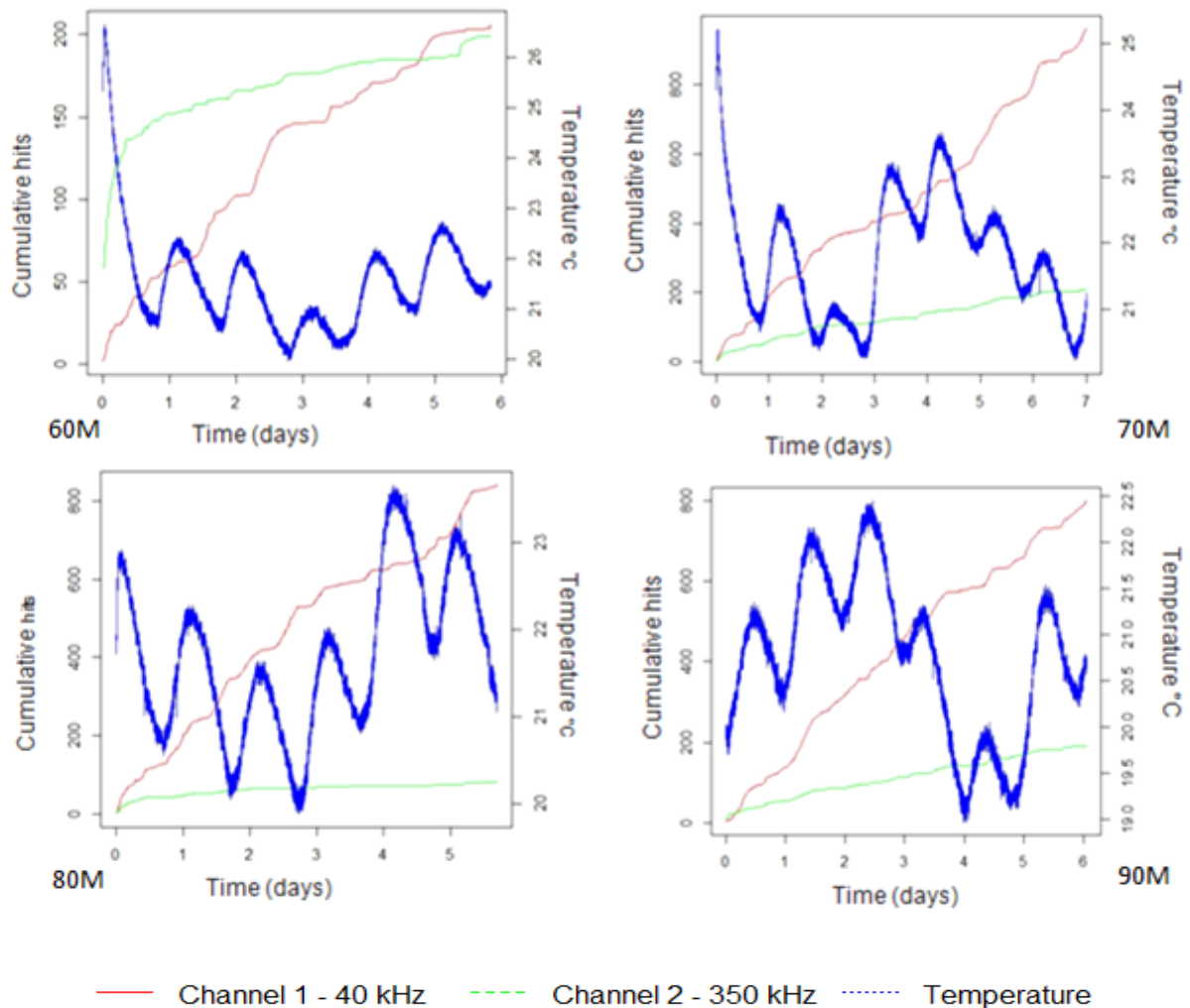


Figure 28: The acoustic emission data in cumulative hits for each frequency of each mortar is potted, in combination with the temperature evolution.

Figure 29 represents the number of hits of a certain peak amplitude, for each mortar and at a frequency of 40 kHz. At this frequency, a large number of low peak amplitude hits are received. Only a few high peak amplitude hits are received on this low frequency. Samples 70M, 80M and 90M has the most hits while 60M definitely has the smallest number of hits.

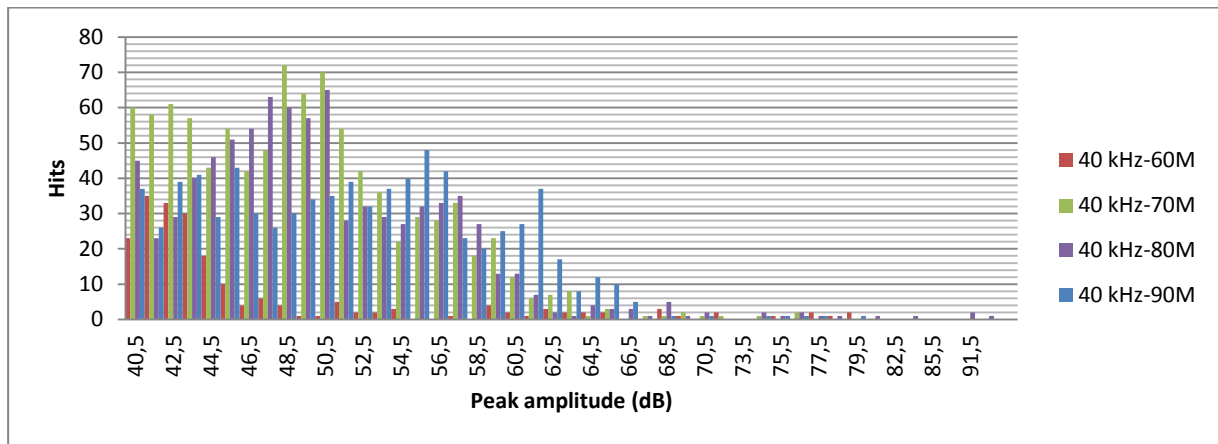


Figure 29: Each hit has a specific peak amplitude in decibel, measured at a frequency of 40 kHz. The amplitudes of the hits are displayed for each sample.

Figure 30 shows the number of hits of a certain peak amplitude, for each mortar and at a frequency of 350 kHz. At this high frequency, a broader range of peak amplitudes and less low peak amplitudes are received. Most of the hits of samples 70M, 80M and 90M have low peak amplitudes. Sample 60M on the other hand has, compared to the other samples, a smaller number of hits in the low peak amplitudes range and a larger number of hits in the high peak amplitudes.

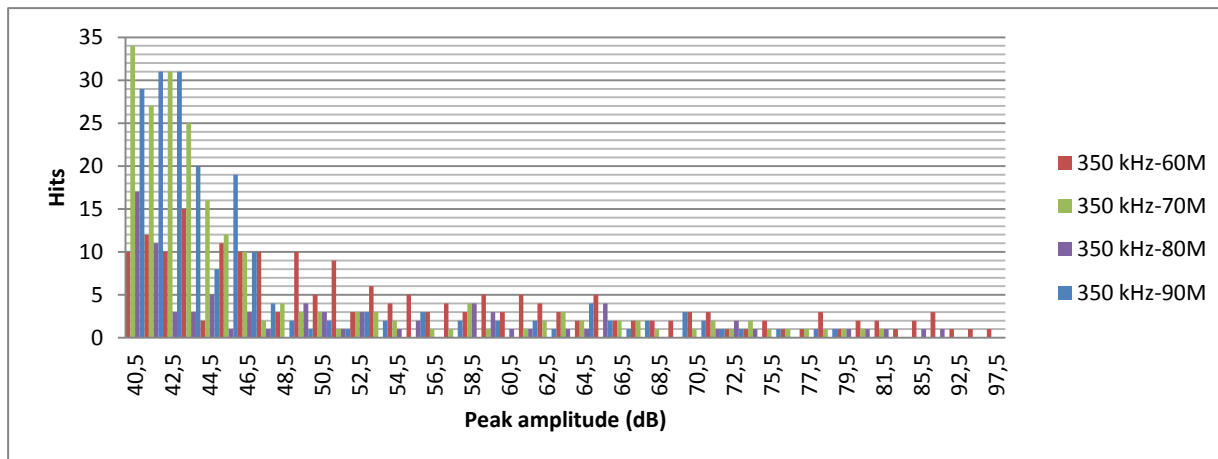


Figure 30: Each hit has a specific peak amplitude in decibel measured at a frequency of 350 kHz. The hits with their amplitudes are displayed for each sample.

3.2.6 LVDT shrinkage results

The shrinkage (mm/m) is displayed on Figure 31. Three shrinkage events can be determined when looking at the curves. Firstly, a strong shrinkage increase in a short time took place. Secondly, a cyclic variation can be noticed. Thirdly, a gradual increase in shrinkage has been observed after 3 days .

Samples 70M and 90M show the same amount of displacement on Figure 31. This could be a coincidence, because there is a time difference for each sample when the measurement starts to record. In this way, a certain amount of shrinkage is not measured for sample 70M, while it is recorded for sample 90M. More shrinkage or displacement would be expected in sample 70M, because more reactions take place. The shrinkage evolution can be compared in a relative way, but not for quantification.

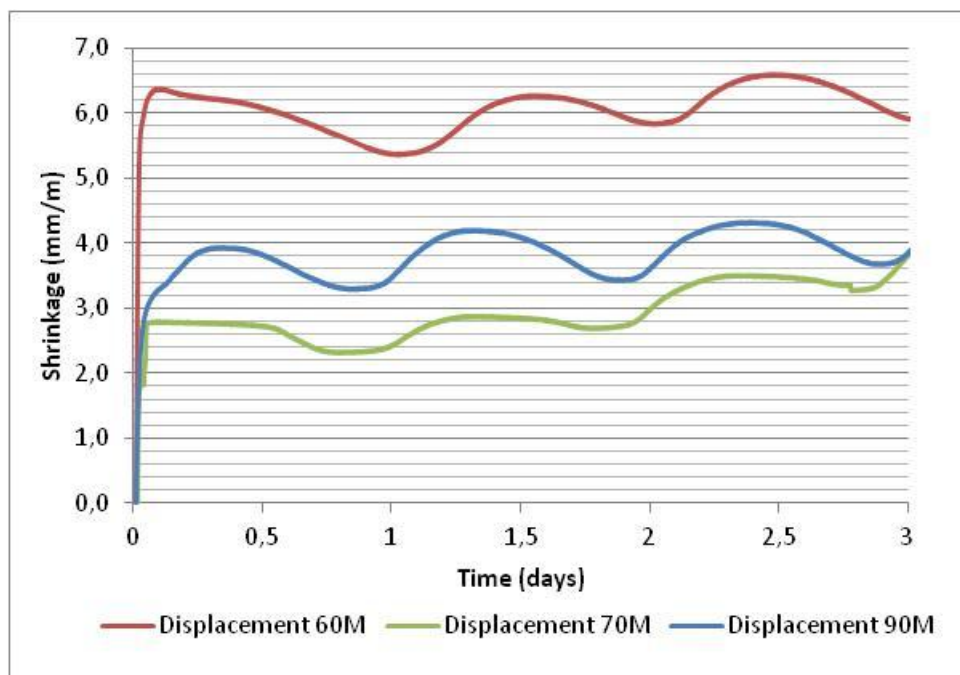


Figure 31: The shrinkage evolution of samples 60M, 70M and 90M for 3 days.

3.3 Discussion: early age properties and behaviour of inorganic polymers

In the discussion chapter, a constructive interpretation will be made of the inorganic polymer early age properties. The shrinkage and crack behaviour of the mortars will be interpreted with the acoustic emission and LVDT data.

3.3.1 Analysis of the heat flow generation

The amount of heat flow generated can be correlated with the amount of reaction taking place in the sample. Two peaks can be identified on the heat flow curves on Figures 20 and 21 for samples 70M and 80M. According to the paper of Xu and Van Deventer (2000) the first peak represents the wetting and dissolution peak of the glass, while the second peak represents the polymerization peak. Two individual peaks can't be distinguished for sample 60M however. Sample 60M has such a low H_2O/K_2O ratio which results, according to Kriskova et al. (2015) in a reaction rate that is so high that both peaks merge together. While dissolution is still taking place at such a low H_2O/K_2O ratio, Provis (2013) states that oversaturation is already reached in the solution to start polymerization. A higher H_2O/K_2O ratio will delay the reaction peaks because the reaction rate is lower (Kriskova et al., 2014).

Almost no dissolution and polymerization peaks are visible in sample 90M. The H_2O/K_2O ratio is so high and the reaction rate is so low, that almost no reaction will occur. In this case, according to Provis (2013) oversaturation of the Al-silicates cannot be reached and almost no polymerization can take place.

A constant increase in cumulative heat flow on Figure 22 is still visible after several hours for samples 60M and 70M. This indicates that reactions are still taking place in the network. According to Lee (2007) these reactions can be designated to self-desiccation reactions.

On Figure 32, one can see that the temperature peaks, of the exothermal polymerization reactions, are delayed for samples 60M and 70M. The temperature peaks occur 20 minutes later than the polymerization peak.

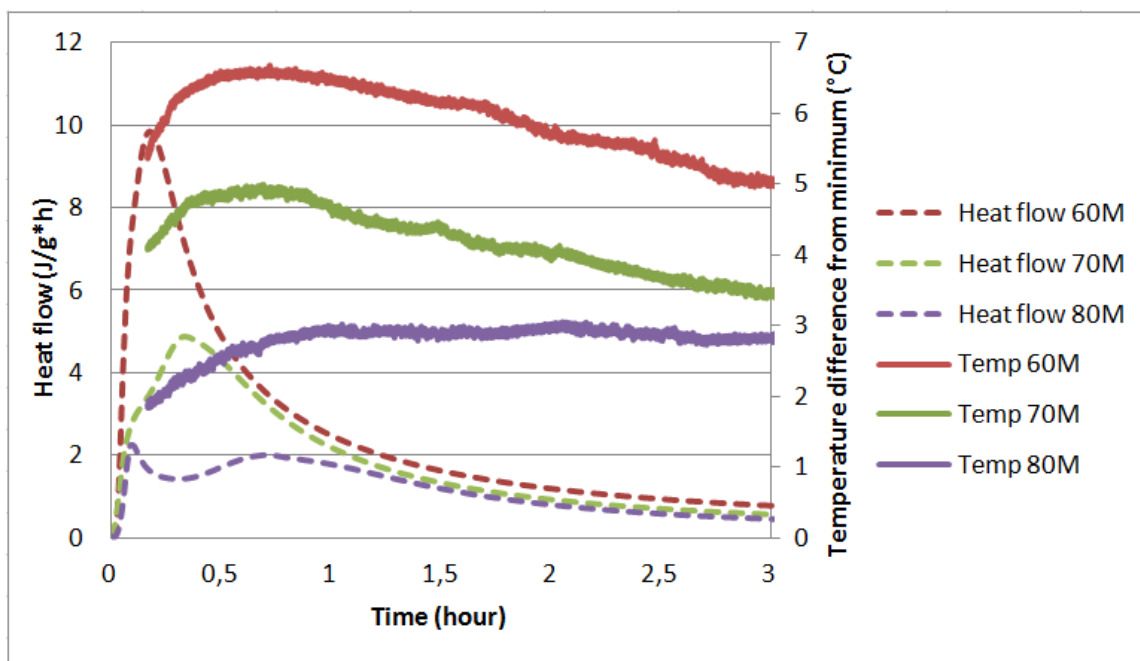


Figure 32: The temperature from the acoustic emission test is plotted along with the heat flow evolution of sample 60M, 70M and 80M.

3.3.2 The setting times according to the penetration depth

The Vicat penetration depths represent the setting time evolution of the samples. Samples 60M and 70M show on Figure 23 a similar setting time. The fast setting time of samples 60M and 70M can be explained by the high reaction peak on Figure 33. A low H_2O/K_2O ratio, results in a high reaction rate and a fast network build-up of the inorganic polymer, according to Bentz and Jenssen (2004). This network will become dense and stiff in a relatively short time. Once a certain densification or stiffness of the network is reached and the dissolution and most of the polymerization reactions are finished, the inorganic polymer will start to set (Scherer, 1988). Figure 33 illustrates that the gel network will be dense and hard after most of the reactions are finished.

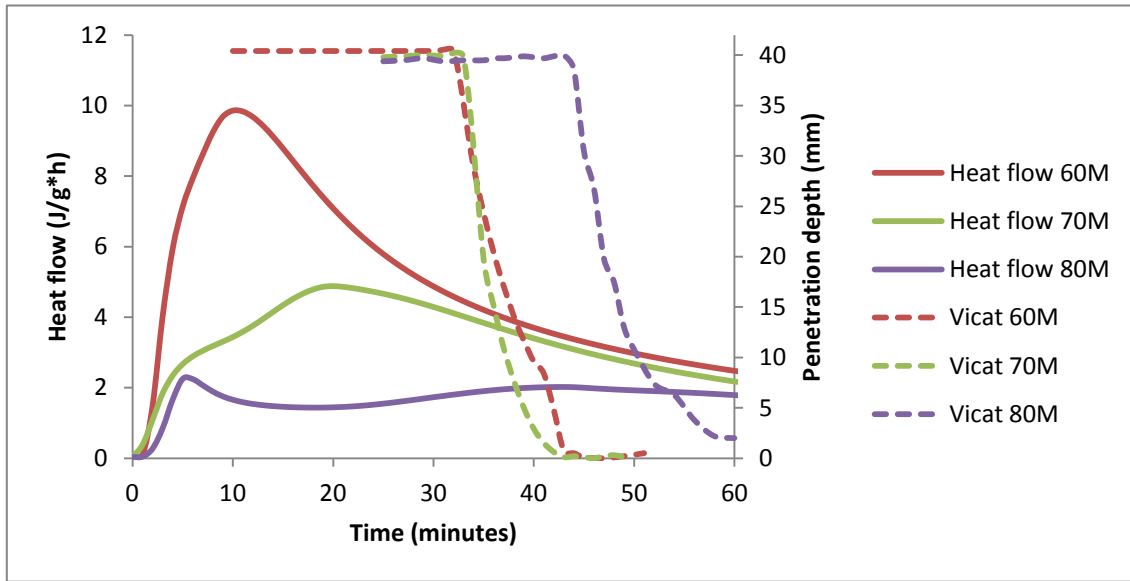


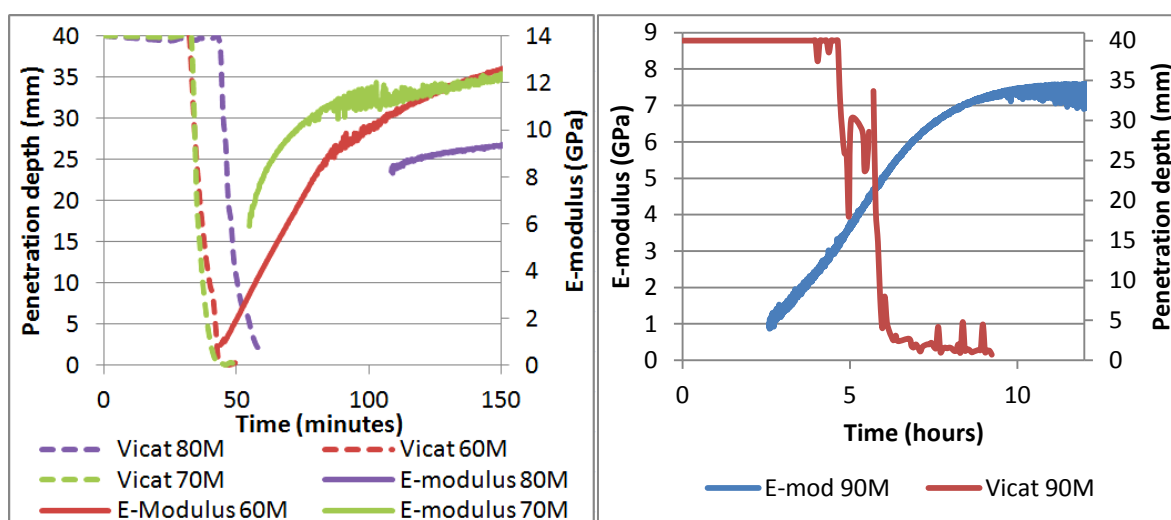
Figure 33: A combined figure of the heat flow and penetration depth in time for samples 60M, 70M and 80M.

Sample 80M has a lower reaction rate, which results in a prolonged time of initial setting, as illustrated on Figure 33. The high H_2O/K_2O ratio in the activating solution of sample 90M will have, stated by Provis (2013) a lack of potassium to reach oversaturation in order to produce a substantial gel network. The setting of sample 90M can also be designated by evaporation of the water. The weakly formed network can reach its hard stage after a certain amount of water is removed .

3.3.3 The evolution in elasticity when curing the inorganic polymer

The setting time and heat flow generation can explain the change in E-modulus. A high E-modulus indicates a short delay in sound wave. In this case, a higher E-modulus has a harder, more solid gel phase or a higher rigidity. Figure 34 indicates that the rigidity build-up is lower for samples with a higher H_2O/K_2O ratio, due to the decrease in amount of polymerization, which is supported by the theory of Bentz and Jensen (2004). Figure 34 shows for samples 60M and 70M that the E-modulus will start to increase, from the moment the samples set. The increase in E-modulus can be delayed because the mortar first needs to be water-unsaturated. When the sample is set, a dense network start to form which results, according to Scherer (1988), in the increase of the rigidity and strength build-up.

Sample 90M on Figure 35 shows a good correlation between the time of setting and the increase in E-modulus. This correlation supports the interpretation of the setting time of sample 90M that is linked to evaporation, which results in the increase of the E-modulus. The E-modulus, on Figure 25 of samples 60M and 70M, still increases after 1.5 days. This behaviour can be linked to the continuous cumulative heat flow generation on Figure 22, due to self-desiccation reactions. Sample 90M doesn't show an increase in E-modulus after a few days. The slow E-modulus accumulation for sample 90M, compared to the other samples, can be explained by the low heat flow generation. A rigid network cannot be produced because of the low amount of reactions that took place in sample 90M.



Figures 34 and 35 represent a plot with the penetration depth and E-modulus generation in time for samples 60M, 70M and 80M.

3.3.4 Compressive and flexural strength: The result of networking

The increase in compressive and flexural strength of the inorganic polymer can be explained by the heat flow development, the setting time and the E-modulus. The strength values on Figure 26 and Figure 27 are a result of the polymerization reactions that took place in the mortar. Sample 60M reaches in a short time high rigidity or elasticity values which are related to the strength properties. The higher the H_2O/K_2O ratio, the slower the strength build-up and this could be, according to Bentz and Jensen (2004) a result of the decrease in reaction rate. The strength properties will decrease significantly with a longer setting time, which agrees with the observations of Kriskova et al. (2015) and Provis (2013) and accounts for sample 90M.

All the samples increase in strength with time, especially samples 60M, 70M and 80M. The strength increase can be correlated with the self-desiccation reactions and densification of the network (Scherer, 1988). The strength increase is however not as fast anymore after 28 days as after 7 days of curing. The strength increase will reach a sort of plateau, according to Scherer (1988). The bad strength properties in sample 90M are a result of the high $\text{H}_2\text{O}/\text{K}_2\text{O}$ ratio, which engenders a lack of reactive agents, such as potassium, to create a dense inorganic polymer network. In that case, almost no self-desiccation reactions and gel densification will occur in sample 90M to achieve, according to Kriskova et al. (2015) high strength properties. The unreacted grains in sample 90M and to a lesser extent sample 80M, will disrupt the gel network, according to Provis (2013). This disruption will result in low strength properties as well.

3.3.5 Cracks received via acoustic emission

The graphs on Figure 28 show an increase in cumulative hits at low frequency when the temperature decreases. The inorganic polymer will cool down and shrink and differential stress will occur that can exceed, according to Holt (2001), the strength of the inorganic polymer. This type of thermal shrinkage will give an increase in hits or cracks at low frequency. The low frequency record mainly cracks with low amplitude peaks, as visualized on Figure 38, which can be interpreted, according to Farhidzadeh et al. (2012), as micro-cracks. An increase in hits at a frequency of 40kHz, as a result of thermal shrinkage, can be interpreted as the formation of micro-cracks.

The temperature variation of each sample on Figure 28 is combined on Figure 36. The temperature variation is visualized as the temperature difference from its minimum temperature. Sample 60M shows a high temperature peak at the beginning, which is, according to Bentz and Jensen (2004) the result of the exothermal polymerization reaction. A higher $\text{H}_2\text{O}/\text{K}_2\text{O}$ ratio will result in a smaller temperature peak, as a result of a lower reaction rate (Vijayakumar, 2013).

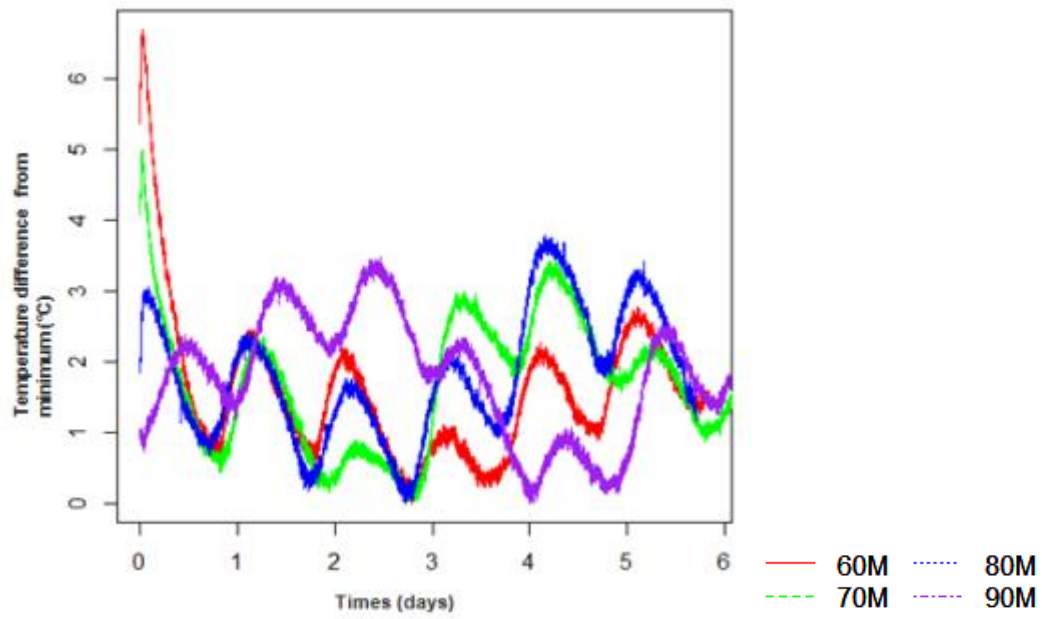


Figure 36: The temperature variation (absolute temperature values are subtracted from the minimum temperature) of the different samples.

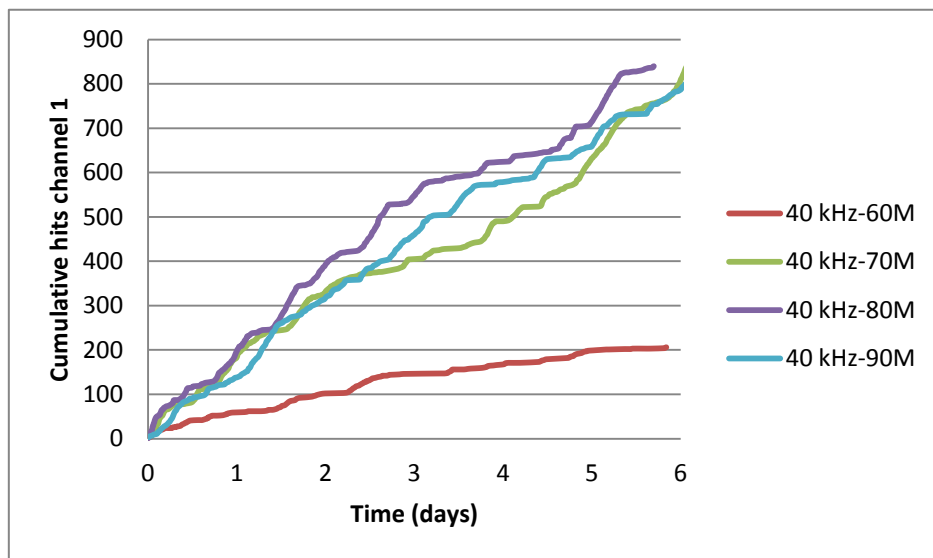


Figure 37: The cumulative hits of each sample received with a 40kHz frequency transducer.

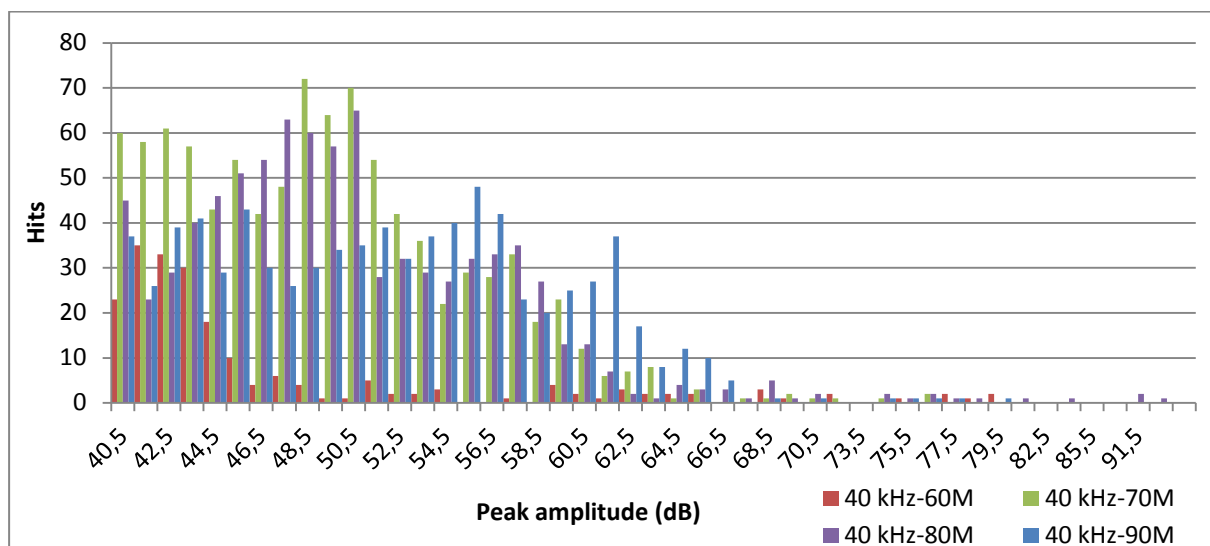


Figure 38: Each hit has a specific peak amplitude in decibel, measured at a frequency of 40 kHz for each sample.

Almost all hits or cracks with a frequency of 40kHz are situated in the low peak amplitude range on Figure 38. Cracks in the range of low amplitude peaks can be interpreted as micro-cracks (Farhidzadeh et al., 2012). Sample 60M shows the smallest number of hits on Figure 37. Samples 70M, 80M and 90M on the other hand, show a strong constant increase in hits per day. Sample 60M produces a small number of micro-cracks, while samples 70M, 80M and in particular sample 90M produce a large number of micro-cracks at a frequency of 40 kHz.

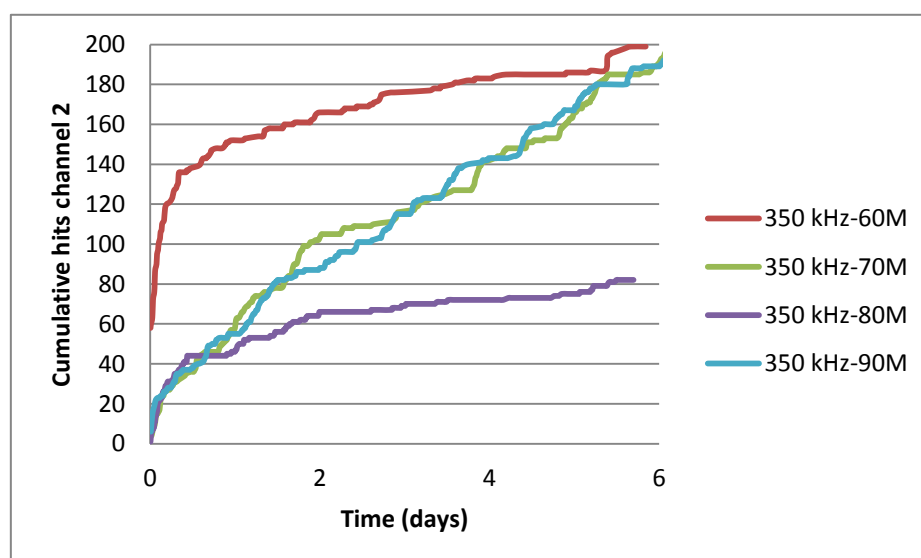


Figure 39: The cumulative hits of each sample received with a frequency of 350kHz.

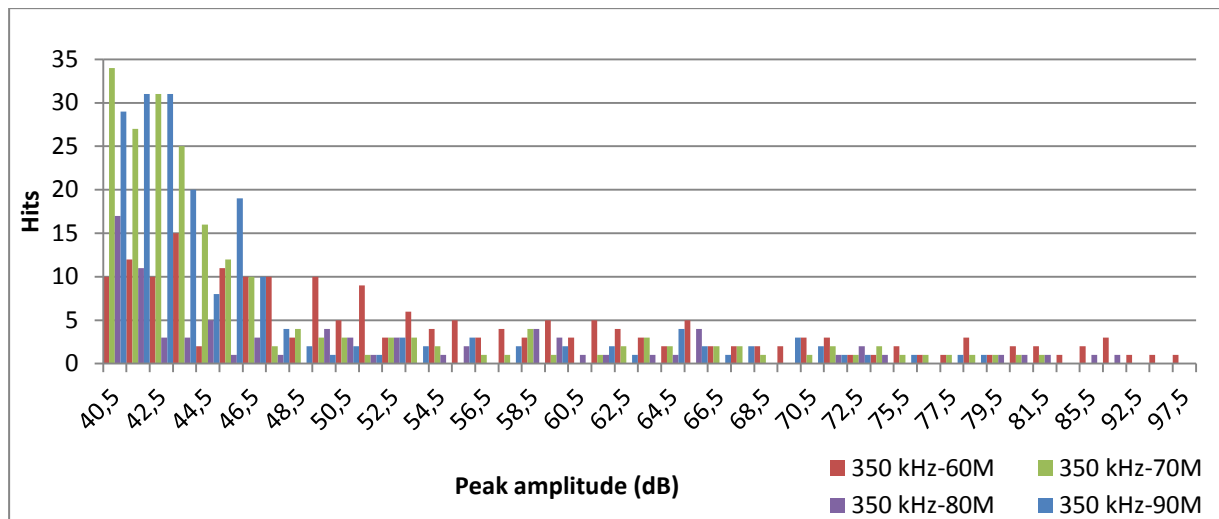


Figure 40: Each hit has a specific peak amplitude in decibel, measured at a frequency of 350 kHz. The amplitudes of the hits are displayed for each sample.

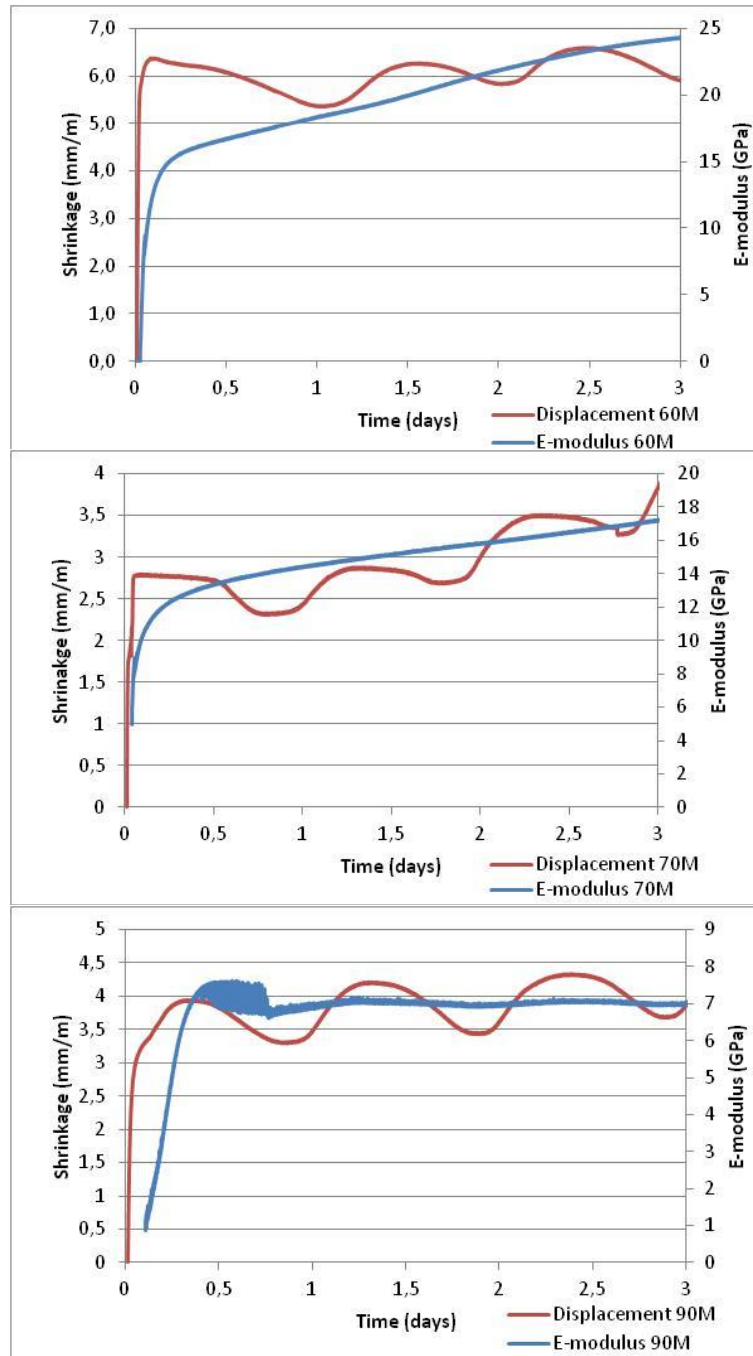
Sample 60M has the largest number of hits at a frequency of 350 kHz on Figure 39. The few high peak amplitudes on Figure 40, can be interpreted as cracks with a high energy release. These high energy cracks can be identified as macro-cracks, according to Farhidzadeh et al. (2012). In sample 60M cracks at high peak amplitudes still occur regularly, while the cracks of samples 70M, 80M and 90M are concentrated in the low peak amplitude range. Sample 60M produces the largest number of macro-cracks, especially during the first day of monitoring. After three days, samples 60M and 80M produce less cracks and reach a sort of plateau, while samples 70M and 90M still produce a constant number of micro-cracks per day. Most macro-cracks are probably formed in the first day, after setting of the inorganic polymer, as illustrated for sample 60M and 80M on Figure 39.

3.3.6 Autogenous and drying shrinkage, determined with the LVDT measurement

In the first hours of measurement, a major shrinkage event can be noticed for samples 60M, 70M and 90M on Figures 41, 42 and 43. This shrinkage event can be identified as early age autogenous shrinkage, which is similar to chemical shrinkage according to the paper of Lee (2007), because no rigidity is measured yet by the E-modulus. Sample 60M shows a much larger amount of early age autogenous shrinkage in comparison with sample 70M, due to the higher amount of polymerization reactions. A decrease is noticed in the rate of autogenous shrinkage once the inorganic polymer is set and when the E-modulus starts to increase. Early age autogenous shrinkage ends once the inorganic polymer achieves a certain rigidity, determined by the E-modulus. Samples 60M and 70M reach this rigidity sooner, after a few hours. Sample 90M needs almost half a day to reach this certain rigidity because the amount in polymerization is much lower. Once the inorganic polymer is hard, self-desiccation shrinkage and a small amount of the late age autogenous shrinkage can occur (Scherer, 1988).

Apart from the cyclic event, another shrinkage event can be noticed with increasing shrinkage in time. This shrinkage event occurs at a lower rate in sample 90M than in samples 60M and 70M. This type of shrinkage is generated due to capillary pore pressure and can be designated to drying and late age autogenous shrinkage (Scherer, 1988). The drying shrinkage occurs at a low rate for sample 90M, because it has a higher H_2O/K_2O ratio. The high H_2O/K_2O ratio implies, according to Keunzel et al. (2012), that more water needs to be removed from the sample to reach the structural water value. Consequently, the shrinkage rate will be lower for 90M, as illustrated on Figure 43. The structural water in samples 60M and 70M on the other hand can be reached faster because they have a lower H_2O/K_2O ratio.

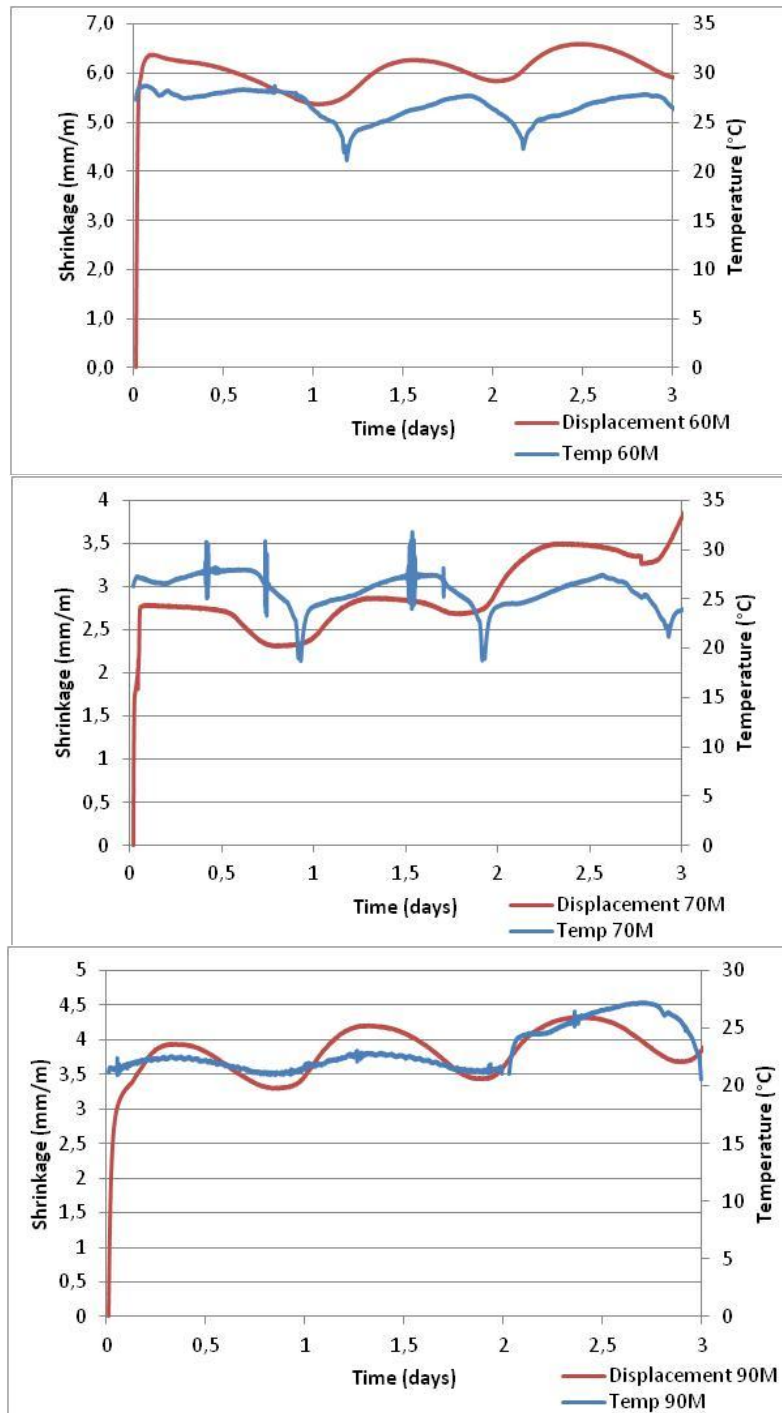
The rate of drying shrinkage agrees with the constant increase in E-modulus for samples 60M and 70M. A low rate in drying shrinkage coincides with a low development in E-modulus for sample 90M. Sample 90M consists of more water and needs more time to dry.



Figures 41, 42 and 43: The shrinkage in time for samples 60M, 70M and 90M is combined with the E-modulus to determine what type of shrinkage occur for which rigidity, regardless the temperature variation. Shrinkage gives an increase in displacement, while expansion results in a decrease in displacement.

Figures 44, 45 and 46 indicate that the temperature variation agree with the cyclic shrinkage variation. A small delay of the shrinkage can be noticed however because the sample cannot be cooled down at once. A temperature decrease results in shrinkage, while a temperature increase results in expansion. This type of shrinkage can be called thermal shrinkage

according to Holt (2001). The thermal shrinkage and expansion cycle is less expressed in samples 60M and 70M because the sample has a higher strength or rigidity than sample 90M to withstand shrinkage.



Figures 44, 45 and 46: The shrinkage in time for samples 60M, 70M and 90M is combined with the temperature variation to determine the temperature influence. Shrinkage gives an increase in displacement, while expansion results in a decrease in displacement.

3.4 Conclusion of the early age behaviour and properties of the inorganic polymer

Depending on the H_2O/K_2O ratio, different early age properties of the inorganic polymer are achieved. A low H_2O/K_2O ratio in the activating solution will result in a large amount of heat flow generation with a high dissolution, polymerization and temperature peak. Consequently, a high reaction rate and an extend amount of polymerization reactions take place in the solution to reach easily Al-Silicates oversaturation and the formation of a network. The fast forming network will consequently give a short setting time. Once the inorganic polymer is set, the network will continue to harden due to self-desiccation reactions. The fast network hardening will result in a decent strength build-up in time and a high E-modulus of the inorganic polymer. A high H_2O/K_2O ratio in the activating solution will give a low heat flow generation with small and wide dissolution, polymerization and temperature peaks. Consequently, it will take a longer time until oversaturation in the liquid is reached and a network can be created. Therefore the setting time as well as the E-modulus and strength development will be delayed.

Early age autogenous shrinkage occurs when the gel is still viscous and an adequate E-modulus value is not developed yet. Once the rigidity or E-modulus is high enough, the sample is set and cools down, the early age autogenous shrinkage will end. The inorganic polymer network resist further early age autogenous shrinkage and stress will build up in the sample. For inorganic polymers with a low H_2O/K_2O ratio high stresses are generated to exceed the early strength of the inorganic polymer. Once the stress exceeds the strength of the inorganic polymer macro-cracks are formed during the first 12 hours of curing. After this stress release, the strength is already so well developed that stress generated in a later stage cannot exceed the strength of the network anymore.

In a later stage, the moisture in the inorganic polymer will evaporate and once it exceeds the structural amount of water, capillary pore pressure will increase. This capillary pore pressure will result in autogenous and drying shrinkage. Drying and self-desiccation reactions of the sample will also continue to increase the rigidity or the E-modulus. The temperature variation will result in thermal shrinkage. The thermal shrinkage and the late age autogenous shrinkage agree with an increase of micro-cracks.

When using an activating solution with a high H_2O/K_2O ratio, the rate in autogenous shrinkage will be lower due to the low amount in polymerization. More water needs to be removed to reach the structural amount of water, which gives a low rate of drying shrinkage.

Thermal shrinkage is more strongly presented because of the low E-modulus. Any capillary pressure increase can easily exceed low strength properties, which results in a large number of micro-cracks.

4. General Conclusion

Inorganic polymer pastes, made from an Ca-Fe-Al silicate rich glass, with an optimum of a $\text{H}_2\text{O}/\text{K}$ -silicates ratio between 70 and 75 wt% or a $\text{H}_2\text{O}/\text{K}_2\text{O}$ molar ratio between 25 and 35 in the activating solution, have sufficient strength properties of a minimum value of 50MPa up to 100MPa and a small number of macro-cracks. A small number of macro-cracks is beneficial for the durability of the inorganic polymer and one of the requirements for the industrial application of the inorganic polymer. Once this optimum is exceeded with higher water ratios, poor strength properties will be achieved with almost no macro-cracks. The inorganic polymer achieves for low water ratios however, excellent strength properties up to 120 MPa, but a large number of macro-cracks are produced.

The macro-cracks in the pastes of part 1 can be linked to the high peak amplitudes of the acoustic emission for mortars, with a $\text{H}_2\text{O}/\text{K}_2\text{O}$ molar ratio lower than 25. Such a low ratio, will result in high dissolution, polymerization and temperature peaks. The large amount of polymerization will give a fast setting time and once the gel is hard, a strong increase in E-modulus or rigidity will be recorded. A large amount of autogenous shrinkage will take place for low $\text{H}_2\text{O}/\text{K}_2\text{O}$ ratios, until the mortar reaches a certain rigidity. Once the inorganic polymer is set, the inorganic polymer network will resist further autogenous shrinkage. Consequently, a large capillary stress is developed and once this stress exceeds the early strength, macro-cracks are produced in the first 12 hours of curing. Once the strength of the inorganic polymer is high enough, the macro-crack formation will develop to a plateau and no more macro-cracks will be produced. When the mortar starts to evaporate the structural amount of water, drying shrinkage will occur. The macro-cracks are unfortunately bad for the durability of the inorganic polymer. To avoid these early age macro-cracks, a $\text{H}_2\text{O}/\text{K}_2\text{O}$ ratio larger than 25 can be used.

Like in the pastes, mortars with a $\text{H}_2\text{O}/\text{K}_2\text{O}$ ratio larger than 35 will give a low amount of polymerization and low strength properties. Drying shrinkage will take place at a lower rate because more water need to be removed. Capillary pore pressure can easily exceed the low strength, which result in a constant formation of micro-cracks in time.

This dissertation can be used to anticipate the evolution in properties of the inorganic polymer, due to the different processes, when the $\text{H}_2\text{O}/\text{K}_2\text{O}$ ratio or reactivity in the activating solution is modified. A change in properties will consequently result in a change in shrinkage behaviour and the type of cracks that are produced in the inorganic polymer, which has an effect on the durability of the inorganic polymer.

Further research can be done, regarding the difference in weight loss, when using a different water ratio in the activating solution. This weight loss can be linked to drying shrinkage. Freeze-thaw experiments can also be conducted to determine the durability of the different mortars, which can be linked again with the inorganic polymer properties. Also the change in $\text{SiO}_2/\text{K}_2\text{O}$ ratio can be investigated to lower the reactivity and prolong the setting time.

5. Reference table

- Analytical, P., 2016, Brunauer, Emmett and Teller (BET) Theory, Practicle Analytical, Denmark.
- Azenha, M., L. F. Ramos, R. Aguilar, and J. L. Granja, 2012, Continuous monitoring of concrete E- modulus since casting based on modal identification: A case study for in situ application: *Cement and Concrete Composites*, v. 34, p. 881-890.
- Bentz, D. P., and O. M. Jensen, 2004, Mitigation strategies for autogenous shrinkage cracking: *Cement and Concrete Composites*, v. 26, p. 677-685.
- Danthurebandara, M., S. Van Passel, L. Machiels, and K. Van Acker, 2015, Valorization of thermal treatment residues in Enhanced Landfill Mining: Environmental and economic evaluation: *Journal of Cleaner Production*, v. 99, p. 275-285.
- Davidovits, J., 2013, Geopolymer Cement, Institut Géopolymère, p. 11.
- Duxson, P., A. Fernández-Jiménez, J. Provis, G. Lukey, A. Palomo, and J. Deventer, 2007, Geopolymer technology: the current state of the art: *J Mater Sci*, v. 42, p. 2917-2933.
- Farhidzadeh, A., S. Salamone, B. Luna, and A. Whittaker, 2012, Acoustic emission monitoring of a reinforced concrete shear wall by b -value-based outlier analysis: *Structural Health Monitoring*, v. 12, p. 3-13.
- GroupMachiels, 2015, Enhanced Landfill Mining, Hasselt, Group Machiels, p. <http://www.machiels.com/company-detail.aspx?ID=885c55e0-f3b6-4fe6-aa25-1fa7bfc312dd>.
- Holt, E. E., 2001, Early age autogeneous shrinkage of concrete: Technical research centre of Finland, Espoo, 197 p.
- JCI, 1999, Autogenous shrinkage of concrete: London, E & FN Spon, 62 p.
- Jennings, H. M., J. J. Thomas, J. S. Gevrenov, G. Constantinides, and F.-J. Ulm, 2007, A multi-technique investigation of the nanoporosity of cement paste: *Cement and Concrete Research*, v. 37, p. 329-336.
- Jones, P. T., D. Geysen, Y. Tielemans, S. Van Passel, Y. Pontikes, B. Blanpain, M. Quaghebeur, and N. Hoekstra, 2013, Enhanced Landfill Mining in view of multiple resource recovery: a critical review: *Journal of Cleaner Production*, v. 55, p. 45-55.
- Kim, M. S., Y. Jun, C. Lee, and J. E. Oh, 2013, Use of CaO as an activator for producing a price-competitive non- cement structural binder using ground granulated blast furnace slag: *Cement and Concrete Research*, v. 54, p. 208-214.
- Kirschner, A. V., and H. Harmuth, 2004, Investigation of geopolymer binders with respect to their application for building materials: *Ceramics - Silikaty*, v. 48, p. 117-120.
- Kriskova, L., L. Machiels, and Y. Pontikes, 2015, Inorganic Polymers from a Plasma Converter Slag: Effect of Activating Solution on Microstructure and Properties: *J. Sustain. Metall.*, v. 1, p. 240-251.

- Kuenzel, C., L. J. Vandeperre, S. Donatello, A. R. Boccaccini, C. Cheeseman, and P. Brown, 2012, Ambient Temperature Drying Shrinkage and Cracking in Metakaolin- Based Geopolymers: *Journal of the American Ceramic Society*, v. 95, p. 3270.
- Lee, N., 2007, Creep and shrinkage of inorganic polymer concrete, Judgeford, New Zealand, BRANZ study report SR 175, p. 32.
- Machiels, L., 26/03/2015, Closing the Circle meeting.
- Machiels, L., L. Arnout, P. Jones, B. Blanpain, and Y. Pontikes, 2014, Inorganic Polymer Cement from Fe- Silicate Glasses: Varying the Activating Solution to Glass Ratio: *Waste Biomass Valor*, v. 5, p. 411-428.
- Piccinin, M., 2016, Blaine Specific Surface Area (Cement density), Torri del Benaco, Italy, The Cement Grinding Office.
- Provis, J., 2013, Alkali Activated Materials: State-of-the-Art Report, RILEM TC 224-AAM: Alkali Activated Materials: Dordrecht, Dordrecht : Springer; Dordrecht : Springer,, 2013.
- Provis, J. L., and S. Bernal, A., 2014, Geopolymers and Related Alkali-Activated Materials: Annual review of materials research, v. 44, p. 299-327.
- Rees, C. A., J. L. Provis, G. C. Lukey, and J. S. J. Van Deventer, 2007, Attenuated total reflectance fourier transform infrared analysis of fly ash geopolymer gel aging: *Langmuir : the ACS journal of surfaces and colloids*, v. 23, p. 8170.
- Sagoe-Crentsil, K., T. Brown, and A. Taylor, 2013, Drying shrinkage and creep performance of geopolymer concrete: *Journal of Sustainable Cement-Based Materials*, v. 2, p. 35-42.
- Scherer, G. W., 1987, Drying gels: *Journal of Non-Crystalline Solids*, v. 89, p. 217-238.
- Scherer, G. W., 1988, Aging and drying of gels: *Journal of Non-Crystalline Solids*, v. 100, p. 77-92.
- Scrivener, K. L., and R. J. Kirkpatrick, 2008, Innovation in use and research on cementitious material: *Cement and Concrete Research*, v. 38, p. 128-136.
- Steins, P., A. Poulesquen, F. Frizon, O. Diat, J. Jestin, J. Causse, D. Lambertin, and S. Rossignol, 2014, Effect of aging and alkali activator on the porous structure of a geopolymer: *Journal of Applied Crystallography*, v. 47, p. 316-324.
- Taylor, R., R. Ray, and C. Chapman, 2013, Advanced thermal treatment of auto shredder residue and refuse derived fuel: *Fuel*, v. 106, p. 401-409.
- Thomassen, L., 2011, Model systel to study the influence of aggregation on the Hemolytic potential of silica nanoparticles: *American Chemical Society*, v. 24, p. 6.
- Van Den Abeele, K., W. Desadeleer, G. De Schutter, and M. Wevers, 2009, Active and passive monitoring of the early hydration process in concrete using linear and nonlinear acoustics: *Cement and concrete research*, v. 39, p. 426-432.

- Vijayakumar, R. M., 2013, Evaluating shrinkage of fly ash –slag polymers, Master of science in civil engineering in the graduate college of university of Illinois at Urbana-Champaign., 55 p.
- Vinai, R., A. Rafeet, M. Soutsos, and W. Sha, 2015, The role of water content and paste proportion on physic-mechanical properties of alkali activated fly ash –Ggbs concrete., Minerals, Metals and Materials Society, p. 11.
- Xu, H., and J. S. J. Van Deventer, 2000, The geopolymerisation of alumino- silicate minerals: International Journal of Mineral Processing, v. 59, p. 247-266.
- Zhang, M. H., C. T. Tam, and M. P. Leow, 2003, Effect of water-to- cementitious materials ratio and silica fume on the autogenous shrinkage of concrete: Cement and Concrete Research, v. 33, p. 1687-1694.

6. Appendix

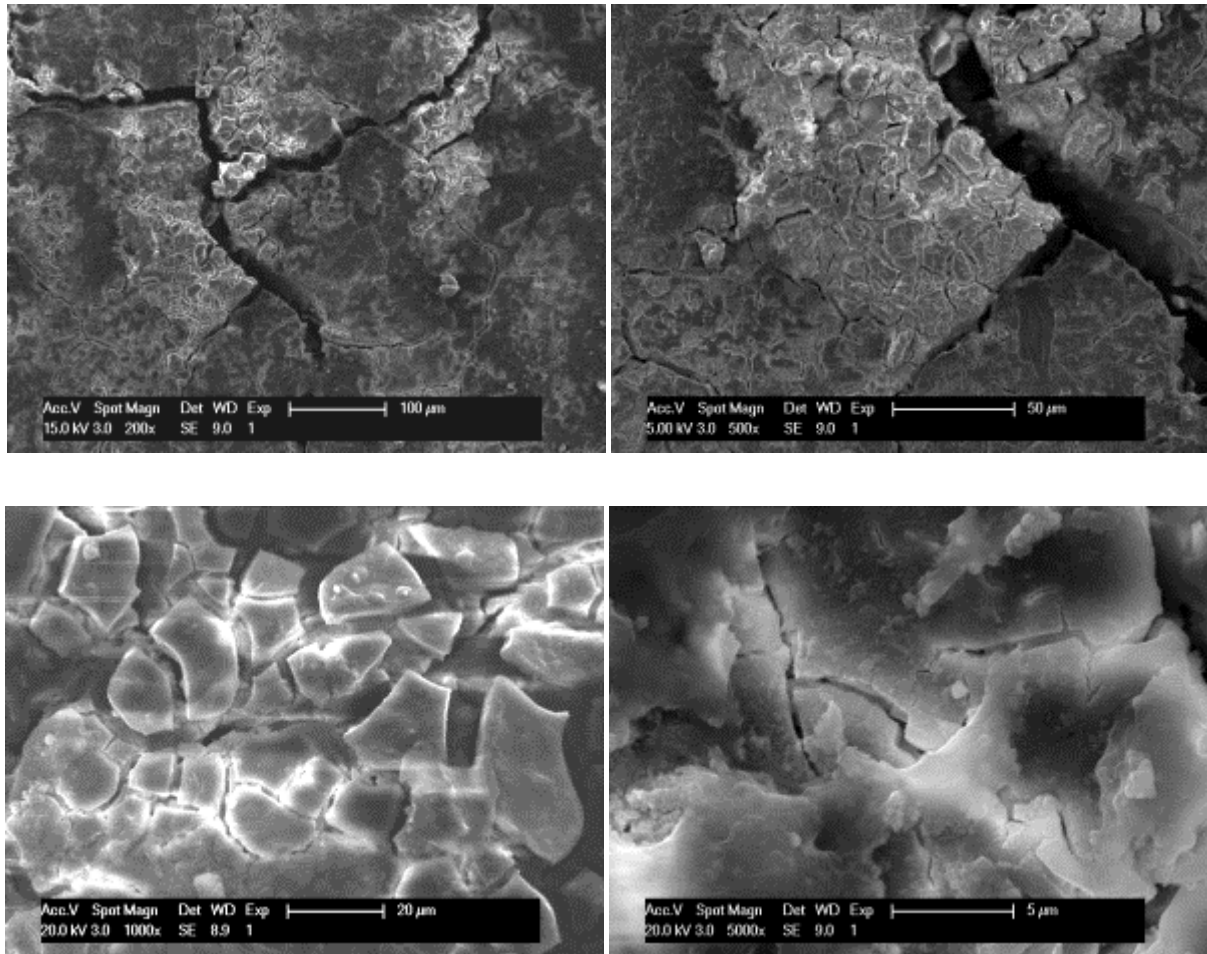
6.1 Crack description of the pastes

6.1.1 The crack description of sample 55B

- SEM

The top surface of the sample shows a typical desiccation crack network. Zones with a different amount in paste development are visible on Picture 6. Major cracks are described in specific zones with a different texture than the matrix of the surface. In general, the cracks have a width from 1-2 μm up to 10 μm and a length of 50 μm up to several hundreds of micrometres throughout the sample.

The side surface has a desiccation crack network that consists of 1st, 2nd, 3th and 4th order cracks. The different orders in cracks can be seen from Pictures 16 to 19. The 1st order cracks have a length of more than 500 μm and a width of 10 μm , as can be seen on Picture 16. The 2nd order cracks are often branched from the 1st order cracks. Second order cracks have a width of 3-5 μm and a length up to 100 μm . The 3th order cracks are better visible at higher magnification and are often concentrated in zones alongside first and second order cracks, as visualised on Picture 17. Third order cracks have a length of 10-20 μm and a width of 1-3 μm . 4th order cracks are also determined. 4th order cracks are often solitaire and have a length of 5-10 μm and a width of 1 μm . These cracks are visible on Picture 19.



Pictures 16, 17, 18 and 19: Pictures representing the crack network on the side surface of sample 55B.

Cracks preferably occur at the white coloured zones. The white zones have a well developed desiccation crack network, as can be seen on Pictures 17 and 18. The cracks branches at an angle of around 120° and the cracks are not straight but curved, so a round pattern is constructed. Most of the cracks of sample 55B are 2nd and 3th order cracks.

- Optical and fluorescence microscopy

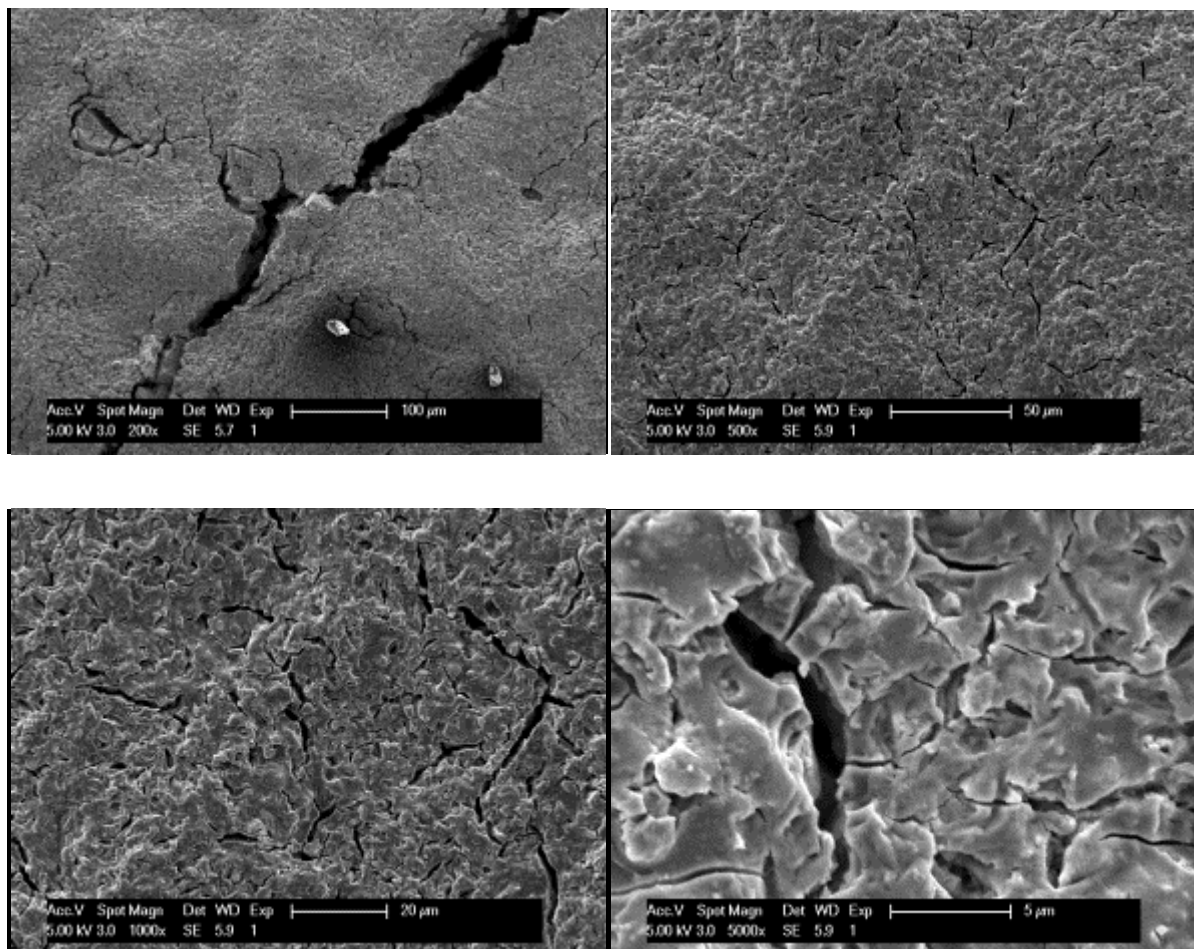
The crack network inside the paste can be examined on a polished section under the fluorescence microscope. The macro-cracks have a length of several hundred micrometres throughout the sample. The cracks originate from voids and connect the voids with each other. There is a considerable number of voids inside the polished section. Some cracks are perpendicular to each other. In general, the interior of the sample is represented by a major crack network that connects the voids. Extended cracks are formed alongside undissolved

grains. Even voids with a diameter up to 500 μm are possible. A small number of micro-cracks is present in the sample.

6.1.2 The crack description of sample 60B

- SEM

Only two major cracks were identified. One of them can be seen on Picture 20. These cracks have a width up to 15 μm and a length of more than hundred micrometres. Some white colored grains are also noticed on top of the side surface. A crack network is also presented in the matrix, as visualised on Pictures 22 and 23. The cracks are not extend for a large distance however. When a crack dies out, a V shaped branch occurs often. This feature can be seen on Picture 23. In other cases, the branched cracks are perpendicular to the main crack. No grains are visible in the matrix. The cracks in the matrix have a length of a few μm up to 50 μm . Most cracks are visible at the 1000x magnification on Picture 22. Small scaled micro-cracks have a length of 4 up to 10 μm . These cracks occur widespread in the matrix on Picture 23. A clear network of cracks throughout the matrix or a clear desiccation crack pattern is not identified.



Pictures 20, 21, 22 and 23: Picture 20 shows a major wide extended crack with a void in the matrix. Pictures 21, 22 and 23 represent the crack pattern in the matrix of sample 60B.

Some clusters of cracks are visible in the matrix. When zooming in on these concentrated crack zones, a depression or bulge is identified in these zones. An example is given in the left corner of Picture 20. Voids of around 20-40 μm diameter are visible. From these voids, cracks are starting to spread out in the matrix.

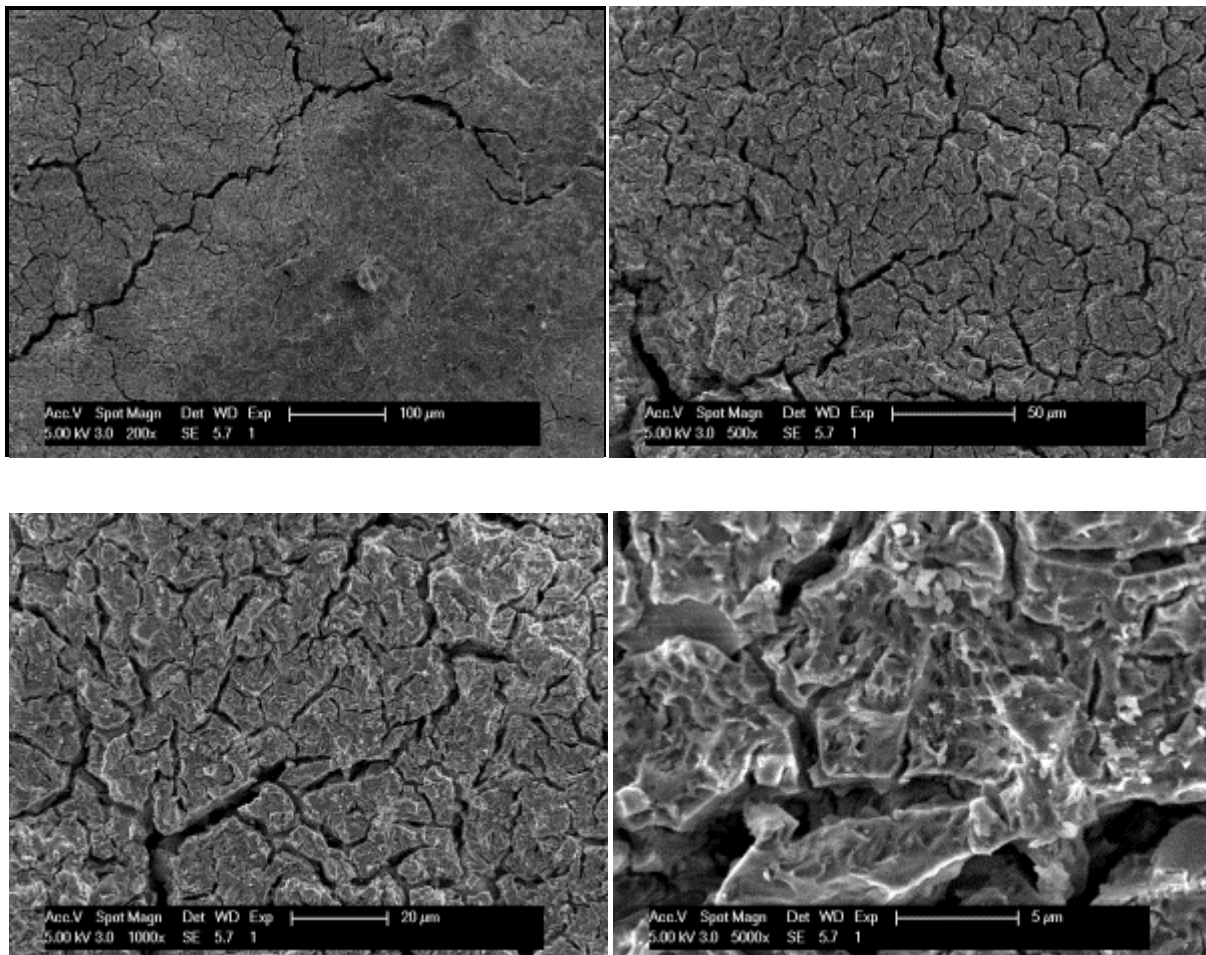
- Optical and fluorescence microscopy

A totally different crack network is visible in the interior of the sample. In the interior, most cracks are aligned. A clear crack network is visible, originating from the voids and connecting the other voids. A good example of this feature can be found on Picture 9. In the interior, some grains are visible in the inorganic polymer paste. The cracks continue in the pores and often cracks branch out from a void with an angle of 90° . The voids have an average diameter of 250 μm . On the optical microscope, desiccation cracks and round voids are visible. A large number of smaller cracks are visible in the major crack network.

6.1.3 The crack description of sample 65B

- SEM

Sample 65B shows at the SEM a well developed extend crack network. Heavily branched cracks are visible. Different orders of cracks can be noticed on Picture 25. The 1st order cracks in the matrix have a width up to 5 μm and a length of 20 μm up to several hundred micrometres, as can be seen on Pictures 24 and 25. 2nd order cracks branch out from the 1st order, illustrated on Picture 24 and 25. These 2nd order cracks have a length of maximum 20 μm and a width up to 3 μm . The 3th order cracks are branched from the 1st and 2nd order cracks and are less than 5 μm long and have a width of maximum 1 μm . On Picture 26 can be seen that the angle of branching is around 120°.



Pictures 24, 25, 26 and 27: These pictures illustrate the different orders of cracks in the matrix of sample 65B. The specific branching angle of 120° is visible on all four pictures.

A clear 1st, 2nd and 3th order crack network is visible. Also weak zones are visible with an extend number of cracks. Picture 24 gives an example of such two zones. One zone, the left zone, has a clear crack and desiccation pattern and the other zone, on the right side, has a badly developed crack network.

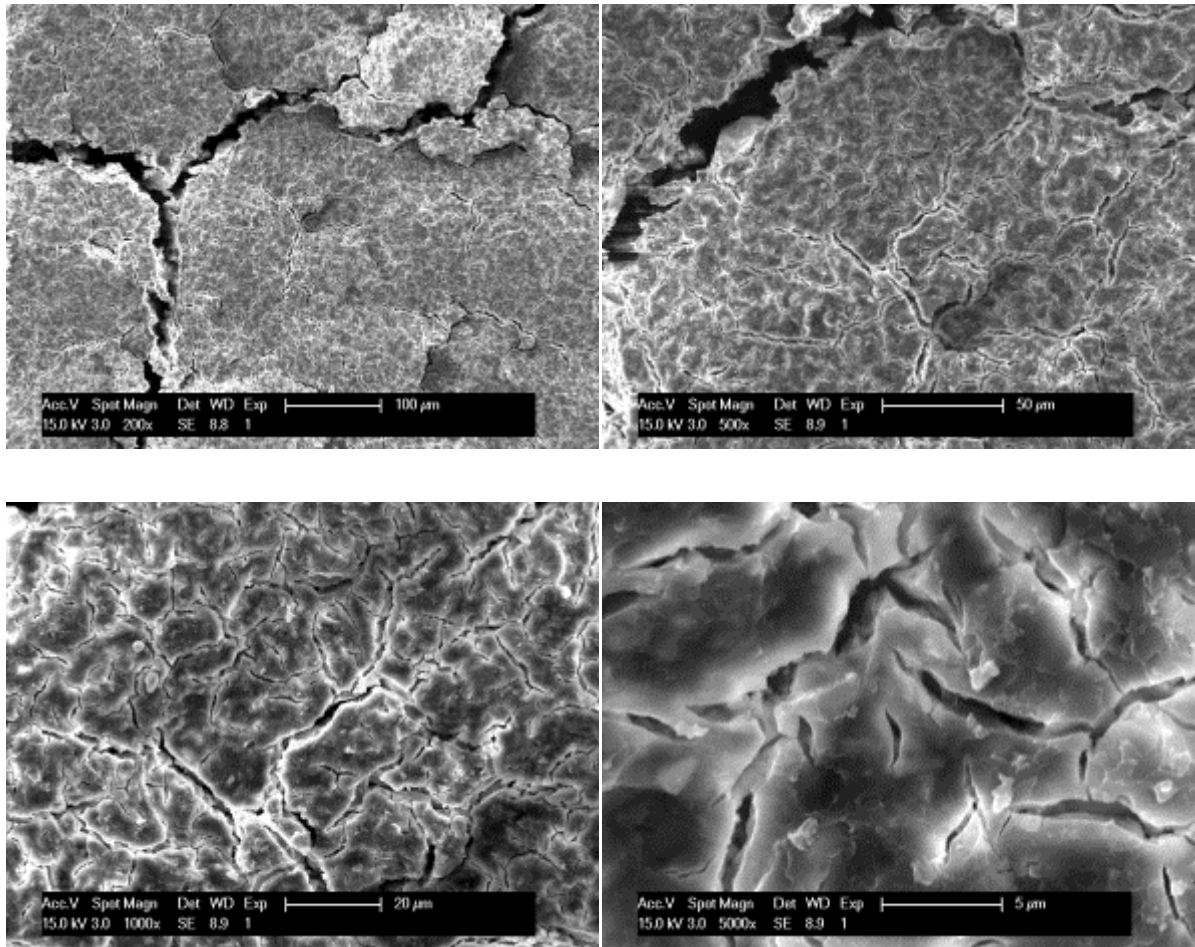
- Optical and fluorescence microscopy

The interior of sample 65B shows an aligned crack network that connects the pre-existing pores. The crack network is however not that extended as on the surface. The interior generally consists of solitaire pores and only a few very long cracks. The voids have an average diameter of 250 µm. Specific zones, which consist of desiccation cracks, are visible under optical microscope. In the matrix, some cracks follow the edge of the grains. A small number of micro-cracks is present. The cracks at the side surface branch out towards the top surface.

6.1.4 The crack description of sample 70B

- SEM

A major branched crack is visible in the matrix of sample 70B. This major crack has a length of some millimetres and has a width up to 10 µm, illustrated on Picture 28. The end of the 1st order crack is branched in 2nd order cracks. In the matrix, also 3th order cracks with round shaped crack patterns are visible on Picture 30. The 3th order cracks have a width of 1-2 µm and a length from 5 up to 40 µm. 4th order cracks are also visible on Picture 31 with a width of less than 1 µm and a length of max 5 µm. The majority of cracks are 3th and 4th order cracks and are only visible at a magnification of 1000x, like on Picture 30. The 3th and 4th order cracks have a branching angle of 120°, as illustrated on Picture 29.



Pictures 28, 29, 30 and 31: These pictures represent the different orders of cracks and its crack network in the matrix of sample 70B.

Several weak zones or clusters of cracks are visible. These depressions or bumps in the matrix consist out of cracks with a relatively very large width of 25 μm in comparison with its length of 40 μm . Cracks with a width of even 30 μm can be identified in voids. From these voids, 1st and 2nd order cracks originate.

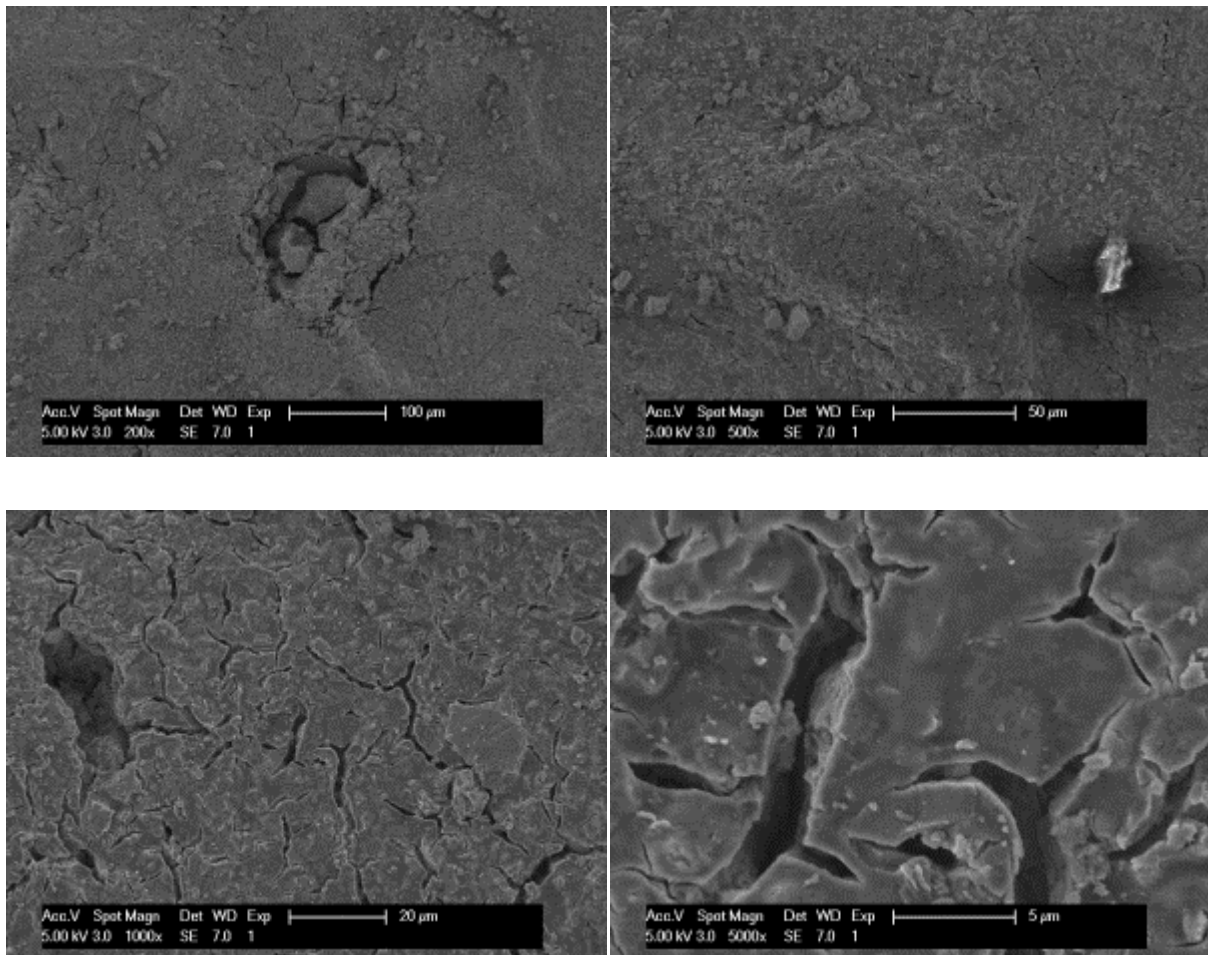
- Optical and fluorescence microscopy

The interior of the sample shows a crack network that connects the pores. The cracks are also connected with a perpendicular angle. Several voids are also visible with a diameter of maximum 100 μm . Grains are visible and cracks can end perpendicular to the grains. The cracks can be several hundred of micrometres long and a few micrometres wide.

6.1.5 The crack description of sample 75B

- SEM

The surface matrix on Picture 32 has a grainy appearance, a relief. The matrix consist out of some clusters with very wide cracks, with a width of 35 μm . These cracks are situated in depressions, bumps or voids, visible on Picture 32. 1st order cracks are identified on Picture 34 and have a width of 3 μm and a length of 10 up to 20 μm . 2nd order cracks occur solitaire or are branched from the 1st order cracks. These 2nd order cracks, visualised on Picture 34, have a length from 5 to 10 μm and a width of maximum 2 μm . Third order cracks can be seen on Picture 35, with a maximum length of 8 μm . The cracks have a typical branching angle of 120°. The majority of the cracks consist out of 2nd and 3th order cracks. Macro cracks of several hundreds of μm long do not occur in sample 75B.



Pictures 32, 33, 34 and 35: Pictures of different magnifications to show the cracks that occur on different scales in sample 75B. The smallest cracks of a few μm long have a large volume or width.

- Optical and fluorescence microscopy

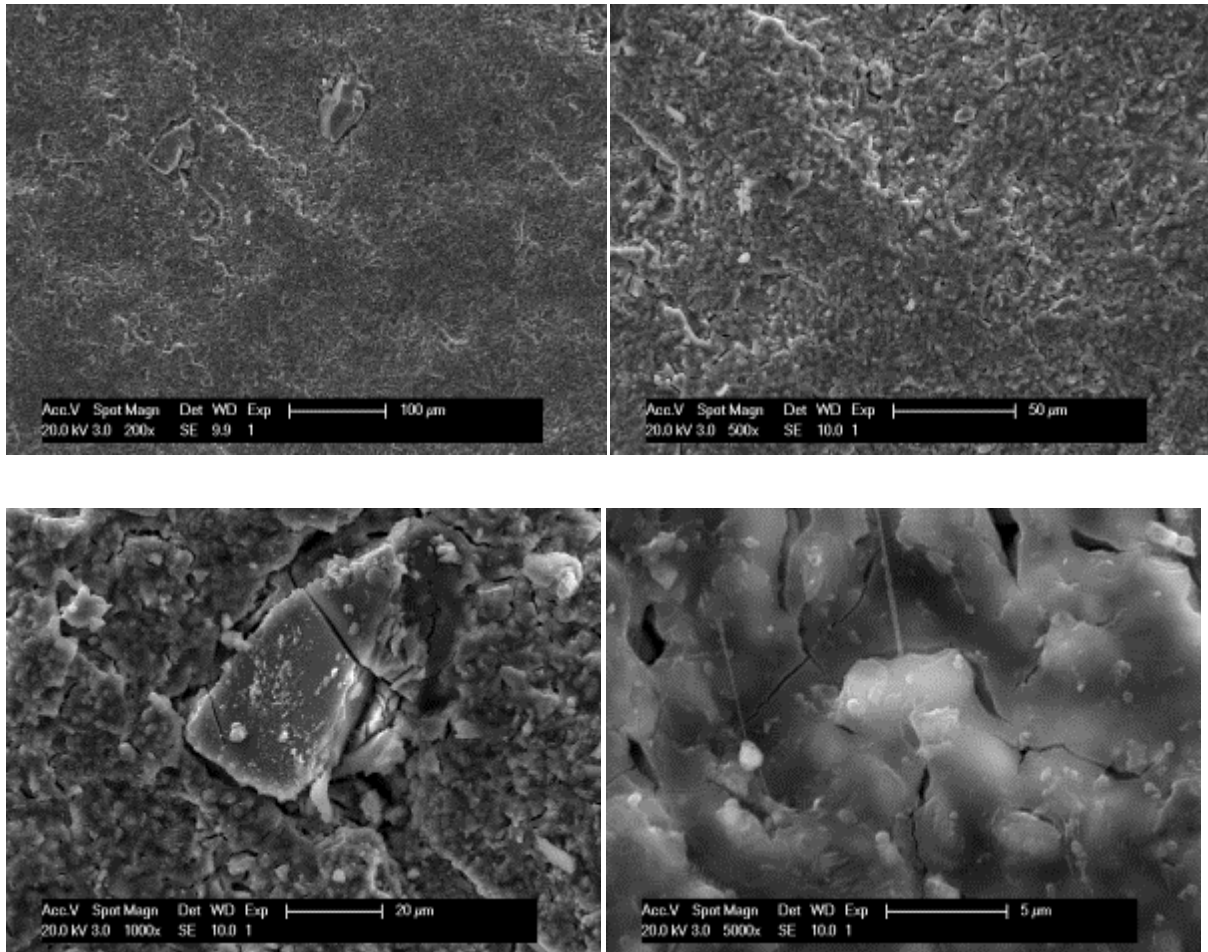
The voids on surface of the matrix of 75B have a diameter of 100 μm . The cracks do not connect the pores and no cracks originate from the pores. The matrix consists out of a large number of grains. Zones of concentrated packed grains can be observed at the surface.

6.1.6 The crack description of sample 80B

- SEM

The side surface of the sample 80B shows a grainy surface. An example of the relief is given on Picture 37. No macro-cracks are visible in the matrix of 80B on Picture 36. The 1st order cracks in the matrix of Picture 40 have a length of 10 μm maximum and a width of 2 μm at most. The 2nd order cracks on Picture 39 are perpendicular to each other and have a length up to 3 μm and a width smaller than 1 μm . These micro cracks occur alongside the grains. Several big grains are visible with a low amount of inorganic polymer formation around the grain as can be seen on Picture 38 and 39.

Three kinds of zones can be identified in the matrix on Picture 8. These zones are the following. A grainy zone to the right with a high relief which is the most common. The middle zone consists of typical desiccation cracks of a great width that only occurs at the surface and doesn't penetrate in the sample interior. The zone to the left consists of a flat surface and shows a crack network perpendicular to each other.



Picture 36, 37, 38 and 39: A clear grainy relief is visible on these pictures. Cracks can only be observed using higher magnifications. Picture 40 shows a grain bedded in the matrix with cracks alongside the grain surface.

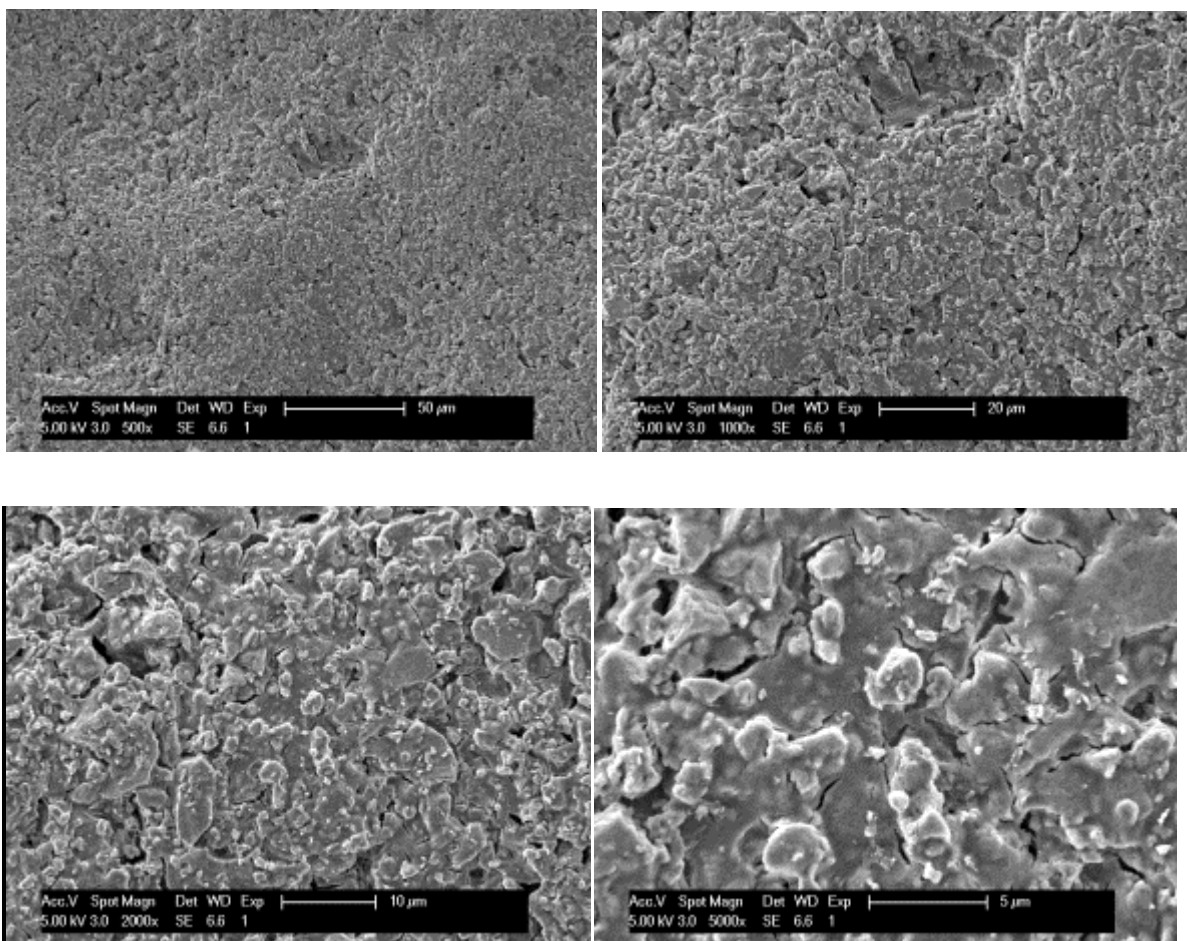
- Optical and fluorescence microscopy

Only one large crack of several hundred micrometres in length is identified. The matrix consists out of large grains and a high relief. Voids of maximum 50 μm in diameter are present in the interior. There are only a few voids in the matrix. Some zones of concentrated grains are determined.

6.1.7 The crack description of sample 85B

- SEM

Sample 85B consists out of a high grainy relief matrix, illustrated on Pictures 41 and 42. Cracks are regularly situated alongside the grains, visualised on Picture 43. No macro-cracks are visible on Picture 40. The 1st order cracks have a length of 5 μm and sometimes even 10 μm with a width up to 2 μm . The 2nd order cracks have a length of 5 μm or smaller and a width of less than 1 μm . The 2nd order cracks occur along the rim of grains on Picture 42. Some big voids are visible with cracks going deep in the interior of the sample.



Pictures 40, 41, 42 and 43: These pictures represent the surface matrix of 85B at different magnifications. A clear grainy surface can be determined.

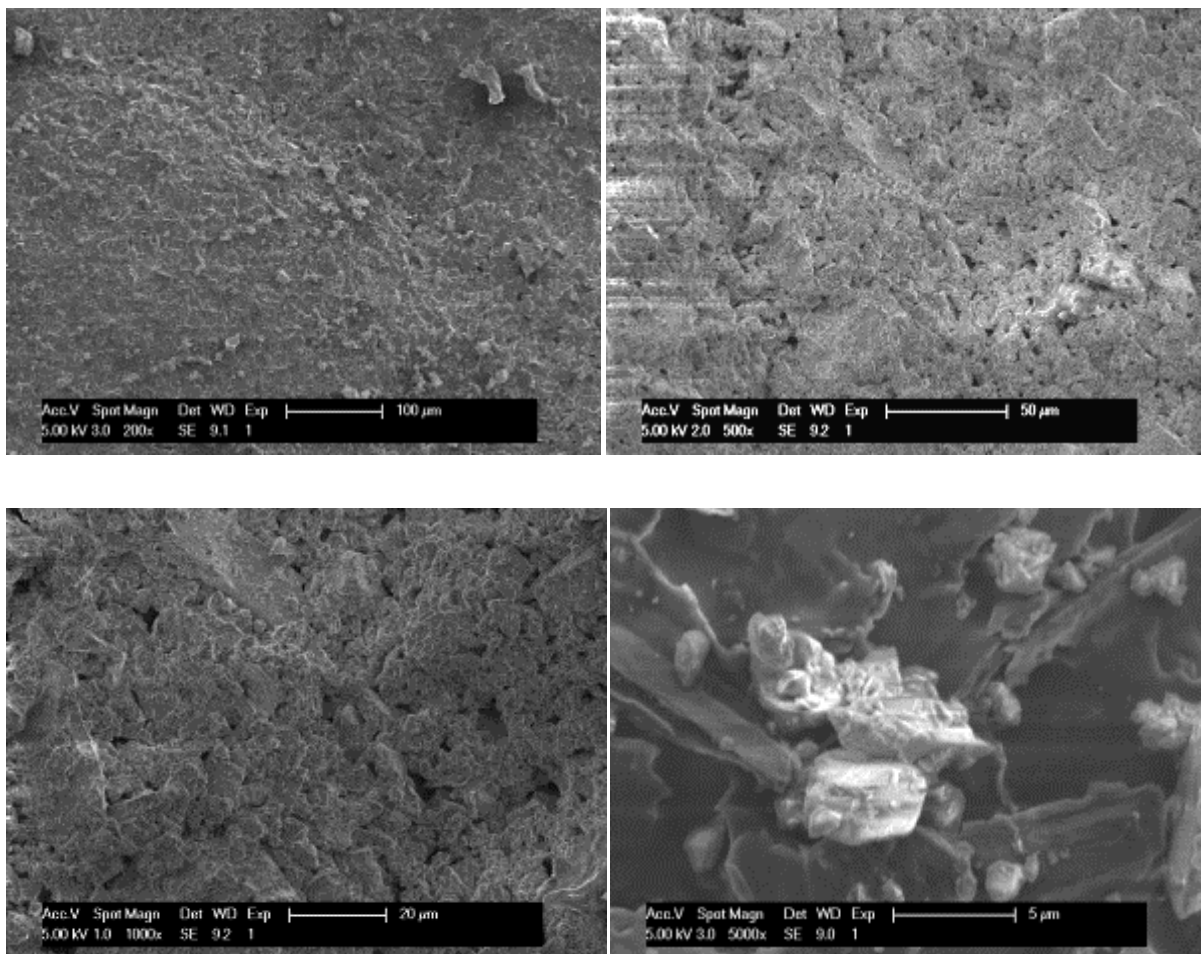
- Optical and fluorescence microscopy

Large grains are visible in the matrix. Cracks are connected perpendicular to each other. The cracks do not connect the voids. At the top surface, desiccation cracks are noticed.

6.1.8 The crack description of sample 90B

- SEM

The matrix has a high relief on Pictures 44, 45, 46 and 47. A high number of grains are laying on top of the surface. Clear cracks cannot be identified in the matrix. The relief consists out of grains of a few micrometres, which are sticking out of the surface. The matrix consists out of cracks, or the appearance of angular elongated voids on Pictures 46 and 47. These kind of cracks follow the edges of the grains. The surface seems to be porous because of the high relief. A few large voids are also situated in the matrix and have an angular shape.



Picture 44, 45, 46, 47: Picture 30 shows grains laying on the surface. Picture 45 and 46 show a high relief with a lot voids and grains. Picture 47 illustrates undissolved grains in the matrix.

- Optical and fluorescence microscopy

A few large cracks can be observed in the interior of a matrix with a high number of grains and a high relief. A white coloured cement is strongly present at the surfaces of the sample.

6.1.9 Sample 95B

The sample wouldn't stick on the sample holder of the SEM and crumbles heavily. This sample cannot be investigated by the SEM or by microscopy.

6.2 Compressive strength results

6.2.1 Compressive strength, 2 days after casting

The following compressive strength results are obtained after 2 days of casting.

Water ratio sample (wt%)	Maximum Load [kN]	Compressive extension at Maximum Load [mm]	Compressive strain (Extension) at Maximum Load [mm/mm]	Compressive strength (Mpa)	Average strength (MPa)	
60.1	42,24	0,84	0,02	26,40	27,39	60wt% Standard deviation: 0,70
60.2	44,38	0,95	0,02	27,73		
60.3	44,80	1,10	0,03	28,00		
60.4	43,85	0,91	0,02	27,40		
70.1	25,79	1,10	0,03	16,12	15,63	70wt% Standard deviation: 0,93
70.2	22,95	1,11	0,03	14,34		
70.3	24,96	0,99	0,02	15,60		
70.4	26,35	1,01	0,03	16,47		
80.1	11,02	1,32	0,03	6,89	6,66	80wt% Standard deviation: 0,35
80.2	11,03	1,30	0,03	6,89		
80.3	10,73	1,29	0,03	6,70		
80.4	9,83	1,23	0,03	6,14		
90.1	1,70	1,19	0,03	1,06	1,11	90wt% Standard deviation: 0,03
90.2	1,80	1,20	0,03	1,12		
90.3	1,80	1,25	0,03	1,13		
90.4	1,82	1,22	0,03	1,14		

6.2.2 Compressive strength, 7 days ago after casting

The following compressive strength results are obtained after 7 days of casting.

Water ratio sample (wt%)	Maximum Load [kN]	Compressive extension at Maximum Load [mm]	Compressive strain (Extension) at Maximum Load [mm/mm]	Compressive strength (Mpa)	Average strength (MPa)	
60.1	91,61	1,28	0,03	57,26	56,92	60wt% Standard deviation: 3,042557872
60.2	97,75	1,10	0,03	61,09		
60.3	87,33	1,20	0,03	54,58		
60.4	87,57	1,07	0,03	54,73		
70.1	42,04	1,41	0,04	26,28	26,32	70wt% Standard deviation: 0,227405646
70.2	41,67	1,18	0,03	26,04		
70.3	42,17	1,16	0,03	26,35		
70.4	42,55	1,02	0,03	26,60		
80.1	16,07	1,38	0,03	10,04	10,62	80wt% Standard deviation: 0,462604754
80.2	17,16	1,27	0,03	10,73		
80.3	17,86	1,26	0,03	11,16		
80.4	16,90	1,07	0,03	10,65		
90.1	2,42	1,16	0,03	1,51	1,58	90wt% Standard deviation: 0,100952806
90.2	2,73	1,20	0,03	1,71		
90.3	2,59	1,04	0,03	1,62		
90.4	2,38	1,03	0,03	1,49		

6.2.3 Compressive strength, 28 days after casting

The following compressive strength results are obtained after 28 days of casting.

Sample water ratio (wt%)	Maximum Load (kN)	Compressive extension at Maximum Load (mm)	Compressive strain (Extension) at Maximum Load (mm/mm)	Compressive strength (Mpa)	Average strength (Mpa)	
60.1	175,27	1,22	0,03	109,55	105,82	60wt% Standard deviation: 3,03
60.2	171,26	1,22	0,03	107,04		
60.3	165,05	1,20	0,03	103,16		
60.4	165,71	1,09	0,03	103,57		
70.1	128,38	0,98	0,02	80,24	76,10	70wt% Standard deviation: 4,53
70.2	125,79	0,97	0,02	78,62		
70.3	120,90	0,97	0,02	75,57		
70.4	111,94	0,89	0,02	69,96		
80.1	56,49	0,59	0,01	35,31	34,47	80wt% Standard deviation: 0,87
80.2	54,37	0,53	0,01	33,98		
80.3	56,14	0,62	0,02	35,09		
80.4	53,58	0,51	0,01	33,49		
90.1	6,33	0,54	0,01	3,96	4,92	90wt% Standard deviation: 0,73
90.2	8,75	0,55	0,01	5,47		
90.3	7,60	0,75	0,02	4,75		
90.4	8,83	0,56	0,01	5,52		

6.3 Flexural strength

6.3.1 Flexural strength after 2 days

The following flexural strength results are obtained after 2 days of casting.

Sample water ratio (wt%)	Maximum Load [kN]	Compressive extension at Maximum Load [mm]	Compressive strain (Extension) at Maximum Load [mm/mm]	Flexural strength (Mpa)	Average strength (MPa)	
60.1	1,79742	0,35001	0,00875	4,21	3,28	60wt%
60.2	1,00016	0,06666	0,00167	2,34	Standard deviation: 1,32	
70.1	0,91843	0,0866	0,00216	2,15	2,07	70wt%
70.2	0,84534	0,05347	0,00134	1,98	Standard deviation: 0,12	
80.1	0,35543	0,04336	0,00108	0,83	0,81	80wt%
80.2	0,33428	0,05667	0,00142	0,78	Standard deviation: 0,035	
90.1	-0,2175	2,11746	0,05294	0,00	0	90wt%

6.3.2 Flexural strength after 7 days

The following flexural strength results are obtained after 7 days of casting.

Sample water ratio (wt%)	Maximum Load [kN]	Compressive extension at Maximum Load [mm]	Compressive strain (Extension) at Maximum Load [mm/mm]	Flexural strength (Mpa)	Average strength (MPa)	
60.1	2,53813	0,3698	0,00925	5,948742	5,54	60wt%
60.2	2,19335	0,26644	0,00666	5,140664	Standard deviation: 0,57	
70.1	1,81577	0,22992	0,00575	4,255711	3,79	70wt%
70.2	1,41633	0,26351	0,00659	3,319523	Standard deviation: 0,66	
80.1	0,77055	0,08672	0,00217	1,805977	1,90	80wt%
80.2	0,85158	0,10636	0,00266	1,995891	Standard deviation: 0,13	
90.1	0,13798	0,1035	0,00259	0,323391	0,32	90wt%
90.2	0,1364	0,39005	0,00975	0,319688	Standard deviation: 0,0026	

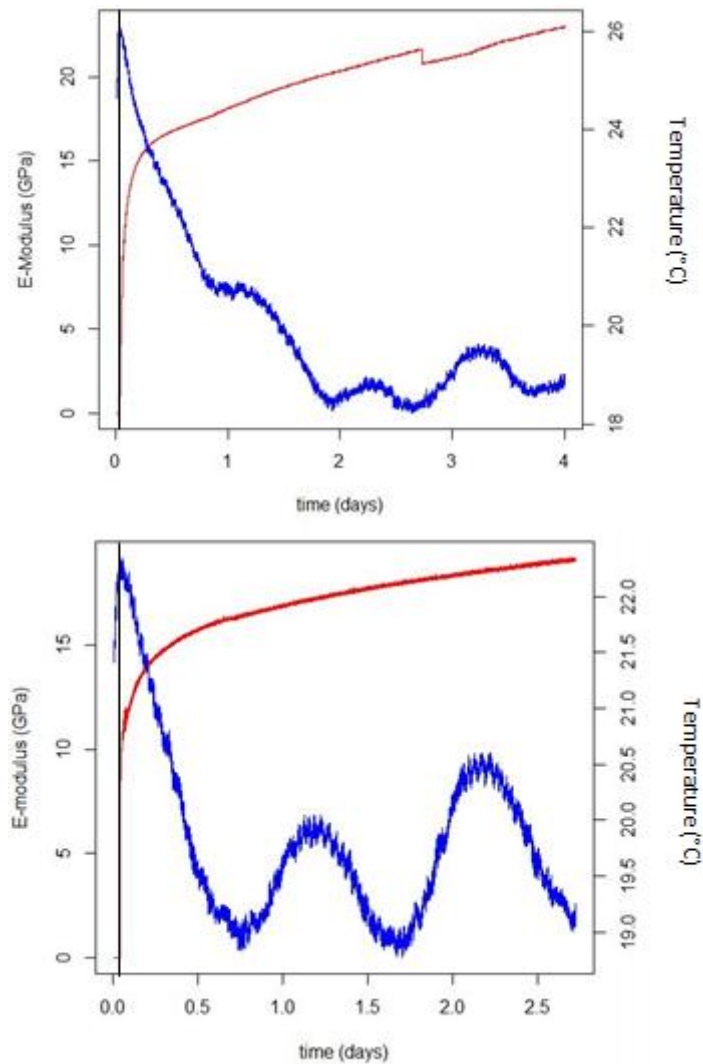
6.3.3 Flexural strength after 28 days

The following flexural strength results are obtained after 28 days of casting.

Sample water ratio (wt %)	Maximum Load (kN)	Compressive extension at Maximum Load (mm)	Compressive strain (Extension) at Maximum Load (mm/mm)	Flexural strength (Mpa)	Average strength (Mpa)	
60.1	0,08393	0,12691	0,00317	0,196711	Broken before	
60.2	4,12918	0,17672	0,00442	9,677766	9,68	60wt%
70.1	3,57086	0,57303	0,01433	8,369203	8,11	70wt%
70.2	3,35064	0,24988	0,00625	7,853063	Standard deviation: 0,36	
80.1	2,30651	0,11342	0,00284	5,405883	5,05	80wt%
80.2	2,00205	0,10976	0,00274	4,692305	Standard deviation: 0,50	
90.1	0,32188	0,05326	0,00133	0,754406	0,75	90wt%

6.4 E-modulus and temperature plot

The temperature and E modulus plot of sample 60M and 70M is given because they are the only samples that have a high temperature peak. The E-modulus start to increase when the sample cools down.



Figures 47 and 48: Figure 47 represents the temperature peak that agrees with the start of the E-modulus for sample 60M. The evolution in sample 70M is illustrated on Figure 48.

AFDELING GEOLOGIE
Celestijnenlaan 200 E nr bus 2408
3001 LEUVEN, BELGIË
tel. + 32 16 32 64 60
fax + 32 16 32 29 80
www.kuleuven.be

